A STUDY OF PHOTON PRODUCTION IN 70 GeV/c PROTON-NEON COLLISIONS

by

Edmund James Whittaker West

A thesis presented for the Degree of Doctor of Philosophy of the University of London

The Blackett Laboratory,
IMPERIAL COLLEGE OF SCIENCE & TECHNOLOGY,
London SW7 2AZ

October 1979

ABSTRACT

A Study of Photon Production in 70 GeV/c Proton-Neon Collisions.

E.J.W. West

This thesis describes the work carried out by the author in the study of direct photons produced in the Big European Bubble Chamber (BEBC). The study was prompted by anomalies in direct lepton data, a related process to direct photon production, and in order to test theoretical models describing these processes. Experimental data on direct photon production were also confused and no data existed at low P_T.

BEBC filled with a 74% molar Ne/H_2 mixture was exposed to a 70 GeV/c proton beam and approximately 6000 photographs were taken with one beam track per frame. Gammas from the proton-Ne interactions were measured using an online measuring system and reconstructed using HYDRA geometry/kinematics.

Bremsstrahlung gammas were removed by imposing suitable opening angle cuts and the remaining gammas paired off to form combinations compatible with π^0 or η. Frames with unassociated gammas of P_T > 0.5.GeV/c were re-examined in an attempt to find associated photons. After accounting for combinatorial problems and measurement/reconstruction efficiencies upper limits on γ/π^0 in the P_T regions around 0.5 GeV/c of a few per cent are set.

η production was also studied and limits on η/π^0 are established. Some data on inclusive π^0 distribution are presented.

CONTENTS

FIGURE CAPTIONS

Figure Captions Continued PAGE

Figures Captions Continued . . . . PAGE

Figures Captions Continued — PAGE

TABLE CAPTIONS

PREFACE

The author has been involved at all stage of this experiment from the bubble chamber exposure to the calculation of inclusive γ production. He was present at the setting up and beam tuning, during the main data taking run in March 1977, and conducted and supervised the scanning and measuring stage of the experiment. The online measuring programs used in the experiment were provided by Dr. Sunanda Banerjee. Certain bugs in the measuring programs were corrected by Dr. E.F. Clayton who also maintained and updated this system after Dr. Banerjee's departure.

The off-line Geometry/Kinematics programs used by this experiment were written and developed at CERN and installed on the IC PDP10 by Eddie Clayton : the author modified the input processor to this program to ensure efficient use of computer time and to minimise program size in event reconstruction. The author was responsible for all subsequent analysis. Ray Beuselinck provoked much useful thought on π^0 kinematic reconstruction and Peter Wright wrote some routines, mentioned in chapter 4, originally for another experiment, and also provided fig. 5.2

CHAPTER 1

Introduction

This chapter outlines the theoretical and experimental interest in the study of direct photons and the motivation for the experiment on which this thesis is based. As will be shown, most of the previous work, both theoretical and experimental, has been concerned with transverse momenta (P_T) which are large. Much experimental interest is in this region, but as some models attempt to make predictions at low P_T, then verification is required.

Whilst there is some overlap between experimental and theoretical aspects of this chapter, the author has attempted to treat them separately. This is both for historical reasons and for clarity. Where there is overlap, however, the author has tried to avoid unnecessary repetition. Much of this discussion is based on published reviews, particularly refs. 1.2, 1.12 and 1.13.

The arrangement of this chapter is as follows: firstly a discussion of large P_T scattering processes and why a study of γ/π is relevant to these, then a particular model (that of Farrar-Frautschi) is discussed followed by a short summary of recent work using QCD. From these one will see why direct lepton pairs and photons reflect essentially similar phenomena. On the experimental side, direct leptons data is discussed and it is argued that a study of direct photons could resolve some of the confusion in this data, followed by a summary of results on direct gamma production.

At the end of the chapter will be a summary of the proposal for the Imperial College direct photon search.

1.1 Theoretical Aspects

1.1.1 Large P_T Scattering Processes

It is clear that the interaction producing large P_T hadrons is not as simple as the process Berman, Bjorken and Kogut (1.1) suggested: namely elastic, large momentum transfer scattering of two freely propagating quarks from initial hadrons, followed by scale invariant fragmentation of the quarks into jets. This mechanism would predict a P_T^{-4} behaviour of the invariant cross-section at fixed x_T ($P_T/\sqrt{s}$) and θ_{cm} (1.2,1.3), giving only a lower limit of P_T^{-8} at moderate P_T ($\sim$6 GeV/c). Experimentally however, it is known to fall more like P_T^{-8}. Two types of modifications can be made to this simple mechanism:

i) Keep the scale invariant fragmentation following the high P_T scattering but leave out the scale invariant qq large P_T scattering (e.g. 1.4,1.5), see fig. 1.1a. This type might be referred to as "leisurely" production as the hadron is produced from the quark in time $\sim 10^{-23}$ P_T/m_o sec where m_o is a scaling factor of order < 1 GeV. The P_T^{-8} dependence was originally inserted ad hoc but QCD effects have recently been applied to justify this.

ii) Retain the dimensional predictions of field theory for the large P_T scattering but drop the scale invariant quark fragmentation. Thus if the large P_T process were a $\pi q \rightarrow \pi q$ or $q\bar{q} \rightarrow \pi\pi$ instead of $qq \rightarrow qq$, then a P_T^{-8} dependence falls out automatically on the basis of dimensional counting, see Appendix A. The constituent interchange (CIM) [1.6] and the quark fusion models [1.7] are examples. This type of process might be called "deep" production as times of order m_o/P_T sec are involved (see fig. 1.1b).

In principle, experiments could determine which, if either, of these processes is dominant. One could study the final states of high P_T processes for such indications. Naively one would expect "leisurely" production to produce a 2 jet final state whereas "deep" production would give up to 1 jet balanced by a mesonic system, (which may appear "jet" like), in the final state.

Present techniques are probably not able to distinguish sufficiently well between these two, experimentally similar, states.

1.1.2 Direct Photons as a Probe

However there is a means at large P_T of distinguishing between these processes, namely direct photon production. Both the order of magnitude of γ/π and its s dependence at fixed x_T and θ_{cm} are significant. As far as "deep" production is concerned we may substitute a photon for the $q\bar{q}$ in the final state (fig. 1.1c) and so n, the number of "elementary fields" to be accelerated is 1 fewer in the case of the γ than that of the $q\bar{q}$, an elementary field being any lepton, photon quark component. A dimensional counting rule [1.3] gives $d\sigma/dt \sim s^{2-n} f(t/s)$ as $s \to \infty$. On this basis then γ/π from deep production would be proportional to s

$$\gamma/\pi \sim s\ f(x_T,\theta_{cm})$$

In leisurely production however, only quark scattering is scale non-invariant so $\gamma/\pi \sim$ constant. Also $\gamma/\pi \sim O(\alpha)$ whereas in deep production it goes more like: $O(\alpha/\alpha_s^2\ s/m_o^2)\ f(x_T,\theta_s)$ (m_o of order 1 GeV). Thus at high s and high P_T γ/π might be very high indeed. Thus a high γ/π and/or one dependent on s would be a good indication of deep production. Hence γ/π gives a good handle on whether large P_T physics is related to short distance quark interaction or whether, for example, thermodynamical models provide better understanding. These latter might predict either (1.2)

i) $\gamma/\pi \sim O(\alpha)$,or

ii) decreasing γ/π at large P_T, in fact a dramatic decrease over the range $P_T \sim 500$ MeV/c to 2Gev/c resulting in a $\gamma/\pi \sim O(\alpha)$ at large P_T.

Apart from the general information one may obtain from a study of γ/π, other interesting physics may be examined apart from production dynamics. The study of γ/π using different projectiles, targets observed π's and jets may be informative in itself.

1.1.3 Farrar-Frautschi Model (1.8)

In this model large P_T quark bremsstrahlung, gives a $\gamma/\pi \sim 10\%$ at large P_T . At low c.m. momentum, γ/π is expected to be of order α but as momentum transfer increases, one would expect γ/π to increase, if short distance quark gluon dynamics become important, due to the weakening of α_s. The dimensional counting rules previously mentioned result in an s dependence also.

$$\frac{\gamma}{\pi} = \beta = s\ f(P_T/\sqrt{s})$$

Parameterising the direct muon data (1.9) gives

$$\beta \simeq 0.004 P_T^{3/2}\ s^{1/4} \quad \text{dependence above } P_T \simeq 2 \text{ GeV.}$$

resulting in $\beta \simeq 5\%$ at Fermilab energies and $P_T \sim 2$ GeV/c, and 15% at 4 GeV/c P_T. This mechanism of bremsstrahlung photons plus the vector meson contribution (1.10), can account for single electron and muon data.

This same mechanism should also be able to explain γ/π at low P_T as well. A constant value of $\beta \stackrel{\sim}{\sim} 3\%$ at $P_T < 1.2$ GeV/c gives the rising e/π at low P_T (1.11). The picture that emerges is of a large β at large P_T decreasing at $P_T^{3/2}$ and levelling off at a constant value of a few percent at $P_T < 1$ GeV/c. A useful test of this model would be to measure γ/π in this low P_T domain.

1.1.4 QCD Calculations

Quantum chromo-dynamics (QCD) is a non-abelian gauge theory of strong interactions, which is asymptotically free so that at large Q^2 (i.e. very short distances), the strong interaction coupling constant, α_s, becomes small enough for perturbative calculation to apply. The constituents of hadrons are assumed to be quarks and the mediators of the strong interaction between quarks are an SU(3) octet of colour gluons. The strong "charge" is called colour. Both quarks and gluons have "colour" but a feature of this theory is that all known hadrons have no net colour. A major difference between QCD and, say, QED is that the photon has no charge and so cannot interact with itself, whereas gluons do have colour and so can interact between themselves. Hence QCD is a non-abelian theory.

The further away quarks are from each other, within a hadron, the greater is the coupling between them, yet the closer together they are, the weaker the force and so they act more or less independently of each other. The consequence of this is that perturbation theory can be applied to calculate high P_T processes.

1.1.5 QCD Model of Halzen and Scott

Halzen and Scott [1.12] argue that the hadro-production of virtual and real photons are clean experimental tests of QCD. The effects of scaling violation in the structure function F(x) of the quarks caused by gluon bremsstrahlung by quarks can be computed to lowest order in α_s and are observable as scaling violation in $F(x,Q^2)$ where Q^2 is the momentum transfer of the virtual photon.

In the Drell-Yan process, (fig. 1.2a), the $q\bar{q}$ annihilation to a lepton pair, gluon bremsstrahlung effects are visible through the quarks transverse motion, which in turn give transverse momentum to the virtual photon. Alternatively transverse momentum may arise from $q\bar{q}$ annihilation to a gluon-photon pair (1.2b), or quark gluon Compton scattering (1.2c).

The same QCD mechanisms that produce transverse momentum of virtual photons yield real photons at large P_T (1.2d). Production of direct photons close to experimental limits are predicted. $\gamma/\pi^0 \simeq 10\%$ are obtained for $P_T \sim 4$-6 GeV, and $\gamma/\pi \sim 1$ at $P_T \simeq 10$ GeV. Figure 1.3 shows the predictions. At $P_T < 2$ GeV, γ/π is predicted to be well below the 1% level.

The large P_T spectrum of direct leptons and photons in all details - dependence on m, s, y and beam particles and the production of direct photons - should provide strong tests of QCD ideas.

It should be stressed, however, that QCD can make no predictions for low P_T processes as non-perturbative (i.e. non-calculable) effects dominate in this region.

1.2 Experimental Aspects

1.2.1 Direct Leptons

Direct leptons are defined as leptons produced in hadronic reactions ($h + h \to \ell^{\pm} + X$) coming from non-trivial sources such as π, K, hyperon decay or photon conversion. Possible sources are:

1) Decay of known mesons (ρ, ω, ϕ, J/ψ, ψ') and pseudo-scalar mesons (η).
2) Decay of unknown objects ($W^{\pm}$, Z, $L^{\pm}$ .....).
3) Decay of charmed mesons (D, $\bar{D}$ ....).
4) Direct photon continuum (parton annihilation, bremsstrahlung)

These last three involve new physics.

It should be pointed out here the need to distinguish single lepton and lepton pair production. Certainly, however, in hadronic reactions the data, particularly for single μ, is consistent with all single leptons being associated with $\ell^+\ell^-$ pairs. This tends to rule out a large charm production cross-section, as most lepton pairs can be attributed to decays of vector mesons or internal conversion of photons.

1.2.2 Status of Direct Lepton Data

As similar QCD diagrams can be used to represent direct lepton pairs and real photon production (by replacing the virtual photon with a real photon), then a knowledge of one can give a handle to the other and vice versa. For example if an anomalously large lepton cross-section is found we might expect therefore a high real photon cross-section.

Early measurements of ℓ/π of order 10^{-4} in hadronic reactions were found, more or less constant with P_T. However calculations from ρ production showed that ℓ/π ought to be much lower, in fact about 10^{-5}, and together with ω and ϕ were thought to represent the level of lepton pairs from the photon continuum. A problem was whether there was a correlation between pairs of low or high mass. Early experiments are forced to make a cut to remove low mass ($m_{e^+e^-} < m_\pi$) electron pairs due to the possibility that they come from Dalitz pairs. The Busser et al experiment(1.14), due to angular cuts in acceptance, would exclude possible new sources of small mass pairs associated with an anomalously large γ/π.

The e/π data is shown in fig. 1.4. The Busser et al experiment excludes small opening angle pairs and was taken at 90° to the beam axis, and the small P_T data of Baum et al was taken at 30° and had a 5° opening angle cut. Where they overlap, the differences may be due to these cuts. Estimates of the contribution of known vector mesons, based on large P_T limits, are also shown. The low P_T data of Baum et al(1.11) cannot be explained in this way unless the contribution from direct photons is more than 10 times greater than expected from vector dominance arguments.

Block et al have calculated the cross-sections for both charm production and direct photon production from the large e/π at low P_T. They find that the charm cross-section (i.e. total inclusive production cross-section for charmed states) in pp collisions would need to be of order 700 μb if the electron signal is exclusively due to charm. Alternatively if this signal is exclusively due to direct photon then the total cross-section for γ's is 30 mb or $\gamma/\pi \approx 15$ %. The high cross-section for charm, whilst not being ruled out, possibly contradicts evidence currently available. Moreover the equality of e^+/π and e^-/π for all P_T values, suggests that the process is electromagnetic. Yet if single photon emission is the source of the direct electrons it must have a strength $\sim$ 15 % of π^o production.

The SLAC - Duke - IC collaboration (1.16) using the SLAC 40" bubble chamber with 18 GeV/c π data find no excess in this low P_T region. This may of course be because the beam energy is below a threshold for the effect to be observed.

It should be noted that measurement of e/π at low P_T is extremely difficult. The contribution to the raw signal from π^o and by Dalitz decays requires, to extract a direct yield, a detailed knowledge of their production characteristics.

One way to remove the problems of π^o Dalitz decays and small mass pairs, is to look at prompt muons instead. The available data is shown in fig. 1.5. Where the muon data overlaps with the electron data, there is general agreement and a systematic rise with P_T is indicated. The single muon data is generally compatible with all single muons coming from $\mu^+\mu^-$ pairs (both single and pairs).

In summary, the ℓ/π ratio seems to be compatible with that due to lepton pairs produced by the decay of known vector mesons and the direct photon continuum, though at low P_T it is difficult to explain the level of this latter (1.13).

1.2.4 Experimental Status of γ/π

The confused state of the data on γ/π can be seen in fig. 1.6. Little data is available for $P_T < 2$ GeV/c and any experiment which measures γ/π in this region 0-2 GeV will be contributing new data. The data above 2 GeV/c, mainly from ISR experiments, particularly in the region 3-4 GeV is conflicting. Darriulat et al [1.17] find an anomalously large γ/π of 20% in this region at $\sqrt{s}$ of 52 and 63 GeV. A contemporary FNAL-JHU result [1.18] at $\sqrt{s}$ 27.4 GeV found γ/π consistent with zero at 3 GeV, rising to 10% at 4 GeV, indicating, if both sets of results are to be believed, that a strong s dependence is involved. More recent ISR results, Amaldi et al [1.19], Cobb et al [1.20], find γ/π consistent with zero in this P_T region. The former finds a hint of a rise above $P_T = 4$ GeV though consistent with zero.

The latter find γ/π rising at high P_T (above 3.5 GeV/c), reaching 20% at $P_T = 7$ GeV[1.21]. The CCOR experiment at the ISR [1.22] report upper limits of 20% in the region 7-10 GeV/c P_T.

Having said all this about high P_T data where much data is now becoming available suggesting a strong P_T dependence, little data is available at low P_T. A recent result [1.23] from the SLAC 82" chamber at $\sqrt{s}$ of 4.5 GeV (10.5 GeV/c π^+p) shows an excess of direct photons at very low x and P_T (between 0 and 20 MeV/c). In fact (46±9)% of all photons in the kinematic region $P_T < 20$ MeV/c and $P_L^* < 20$ MeV/c are attributed to direct photons. More data in this region would be useful to see if the direct photon continuum in the low P_T region is as high as the direct lepton data suggests. Also Farrar-Frautschi propose that γ/π levels off at several per cent in this low P_T region. Again such an experiment would be a test of this model. QCD predicts that γ/π becomes negligible below 2 GeV P_T. If a high γ/π is found at low P_T, clearly some other processes must be taking place.

In summary it can be said that an experiment designed to study direct photons at low P_T should have some physics interest, as a means of testing between theoretical models, resolving experimental ambiguities or if only to make a study of a region not previously explored.

1.3 Aim of Experiment

In August 1976, prior to the author joining the group, the Imperial College bubble chamber group submitted a proposal [1.24] to the CERN SPS to study direct photon production in BEBC filled with a Ne/H_2 mixture and using 100 GeV/c protons as the beam particle. It was believed that a γ/π at the level of 3% would be observable in a large Neon filled bubble chamber without the uncertainties of acceptance, confusion from neutron interactions, etc. The gamma detection efficiency could be made sufficiently high that most of the π^0 decays would have both gammas detected, leading to an easy separation of the direct gamma signal. The majority of bubble chamber events are, of course, at low P_T.

Previous bubble chamber experiments to study inclusive photon production have generally been done in hydrogen filled chambers, where the gamma conversion length is considerably longer than the dimensions of the bubble chambers. Materialisation of both gammas from a π^0 is rare and so comparison of double and single gamma events would not reveal the presence of a relatively high γ/π. One experiment, a 14 GeV/c K^-p (1.25) showed that the inclusive π^o cross-section (assuming all gammas come from π^o's) is to within a few per cent the same as for π^+ and π^-, indicating a γ/π^o less than a few per cent at this energy. However even optimistic models would not expect an effect to show at these energies.

BEBC filled with 74% Ne/H_2 was regarded as a compromise between high gamma detection efficiency, low probability for secondary interactions and good measurement precision. Gamma detection with a small fiducial volume was believed to be about 95% efficient.

As it was expected that the production of gammas was by quark bremsstrahlung, and consequently would be expected to depend on the quark charge, the proton was regarded as the best beam particle. Work by Halzen and Scott (1.12), tends to suggest that the anti-proton would have been a better choice. The proposal suggested that the momentum of the beam should be 100 GeV/c, at the upper range of the secondary hadron beams from the SPS. This would tend to give a higher π^o mean momentum and therefore more easily paired gammas, though at the expense of a higher π^o multiplicity and reduced measurement precision.

To avoid visual confusion due to secondary interactions one beam particle per frame flux was proposed. A total of 10,000 frames were asked for which would have resulted in 4,200 events within the fiducial volume. With 2.8 π^o per event then a total of 12,000 π^o's would be produced, and with a 3% γ/π, 360 direct gammas.

1.3.1 Backgrounds

There would be principally two sorts of background.

a) gammas from π^0 which are not paired with another gamma because of:

i) visual confusion,

ii) ambiguity in forming gamma pairs,

iii) escape of the gamma from the chamber

b) Bremsstrahlung.

By using one beam track per frame ai) would be reduced. aii) will be discussed in much greater detail later but the proposal expected that this would be determined by the case of pairing gammas at the scanning stage and the gamma energy resolution. Also opening angle criteria could be used. The expected measurement precision for the gamma momenta was expected to be of order 10% implying that the momentum error of the π^0 would be of order $3\frac{1}{2}$% with the π^0 mass constraint imposed.

The number of gammas escaping from the chamber had been estimated from Monte Carlo studies to be 3.5%. Bremsstrahlung would be removed by imposing scanning cuts and opening angle cuts between gammas.

It was hoped to perform a short, minimal experiment to see if a large γ/π^0 existed at low P_T. Aids to a swift analysis were the small sample, and the "parent-child" factor. This latter is discussed in Appendix B, but briefly it can be stated as follows: the mean P_T of the gammas from π^0 decay is lower than the mean P_T of the parent π^0's. Moreover, at a given high P_T the number of gammas from π^0 decay will be smaller than the number of π^0's at that P_T.

Thus in order to find a detectable signal, it was decided to look in a P_T region where the number of gammas was much reduced compared to the number of π^o's. Thus much effort could be put into pairing these gammas to form π^o's (or η's) and that any excess (i.e. direct photons) would show up more easily. This P_T region was chosen to be 0.5-1 GeV/c. Above 1 GeV/c statistics would run out, but at 0.5 should still be high enough to be sensitive to a 3% γ/π.

REFERENCES

1.1. S.M. Berman, J.D. Bjorken and J.B. Kogut Phys. Rev. D4 2381 (1971)

1.2. G.R. Farrar CALT 68-576 (1977)

1.3. S.J. Brodsky and G.R. Farrar Phys. Rev. Lett. 31 1153 (1973)

1.4. R.D. Field and R.P. Feynman CALT 68-565

1.5. S.D. Ellis and M.B. Kislinger Phys. Rev. D9 2027 (1974)

1.6. R. Blankenbekler, S.J. Brodsky and J.F. Gurion Phys. Lett. 42B 461 (1972) and Phys. Rev. D8 187 (1973)

1.7. P.V. Landshoff and J.C. Polkinhorne Phys. Rev. D8 4157 (1973)

1.8. G.R. Farrar and S.C. Frautschi Phys. Rev. Lett. 33 868 (1974)

1.9. J. Boymond et al Phys. Rev. Lett. 33 112 (1974)
J.A. Appel et al Phys. Rev. Lett. 33 722 (1974)

1.10. M. Bourquin and J.M. Gaillard Phys. Lett. 59B 191 (1975)

1.11. L. Baum et al Phys. Lett. 60B 485 (1976)

1.12. F. Halzen and D.M. Scott Wisconsin Preprints COO 881 - 16 and COO 881 - 21

1.13. N.S. Craigie Physics Reports Volume 47 No. 1 (1978)

1.14. F.W. Busser et al Phys. Lett. 53B 212 (1974)
and Nucl. Phys. B113 189 (1976)

1.15. M. Block et al

1.16. J. Ballam et al Phys. Rev. Lett. 40 741 (1978)
and Phys. Rev. Lett. 41 1207 (1978)

1.17. P. Darriulat et al Nucl. Phys. B110 365 (1976)

1.18. B. Cox et al Hamburg Conf. 1977

1.19. E. Amaldi et al Rome Preprint ROM 78 - 113

1.20. J.H. Cobb et al

1.21. CERN Courier June 1979 153
C. Kourkoumelis et al - talk given at Birmingham IOP conference March 1979

1.22. A. Segar , private communication (after talk given by author at Birmingham IOP conference 1979)

1.23. A. Goshaw et al APS Spring meeting 1979

1.24. T.C. Bacon et al CERN / SPSC / 76-50

1.25. A.C. Borg et al CEN Saclay D.Ph.P.E. 76-01

Figure Captions

1.1 Large P_T Scattering Processes

a) "Leisurely" Production

b) "Deep" Production

c) "Deep" Production with Gamma in Final State

1.2 QCD Diagrams for Direct Lepton/Gamma Production

a) Drell-Yan

b) $q\bar{q}$ Annihilation

c) Quark-Gluon Compton Process

d) Direct Photon and Lepton Related Processes

1.3 γ/π versus P_T for various Interactions according to Halzen and Scott

1.4 Direct Electron Data: e/π versus P_T

1.5 Direct Muon Data: μ/π versus P_T

1.6 Direct Photon Data: γ/π versus P_T

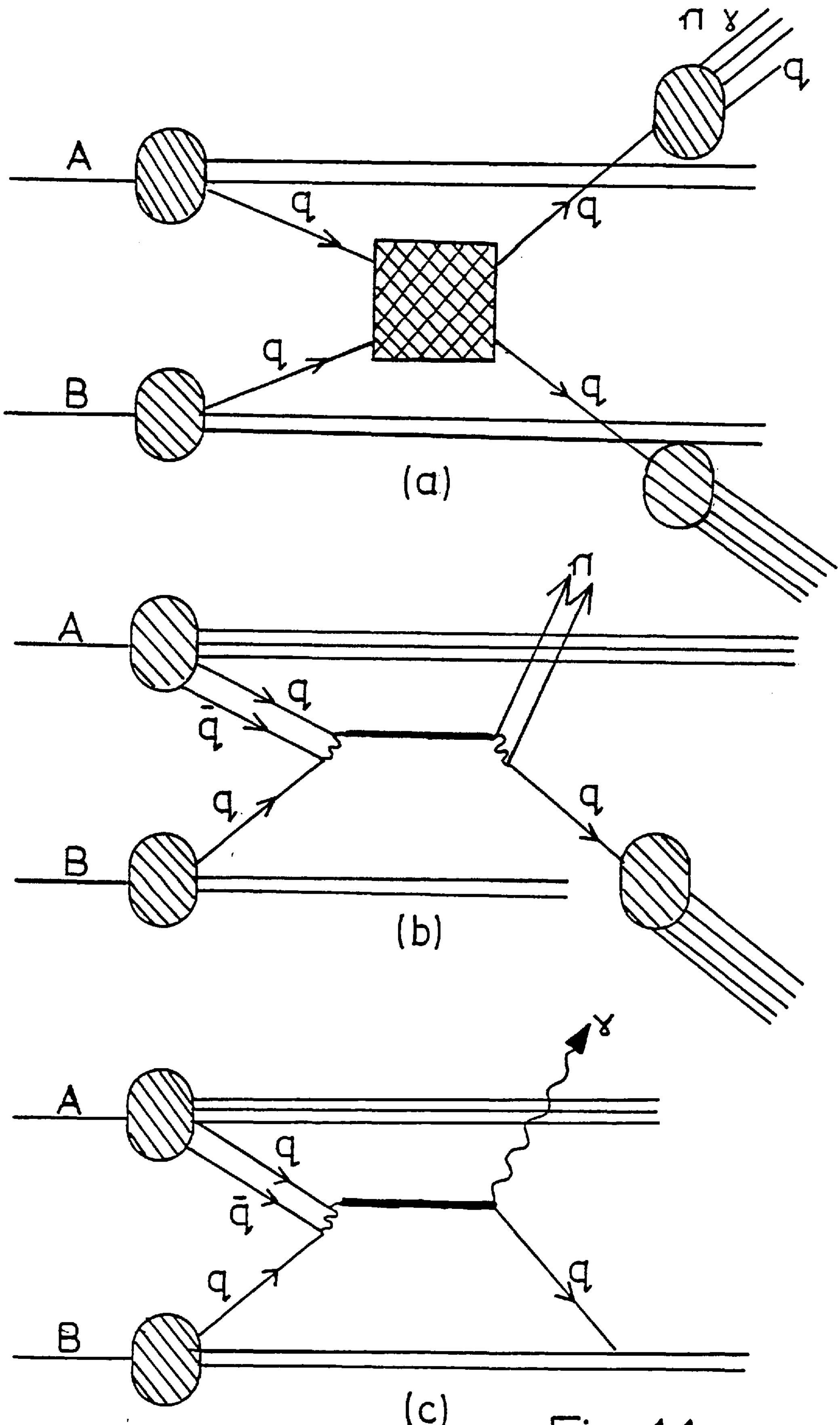

Fig 11

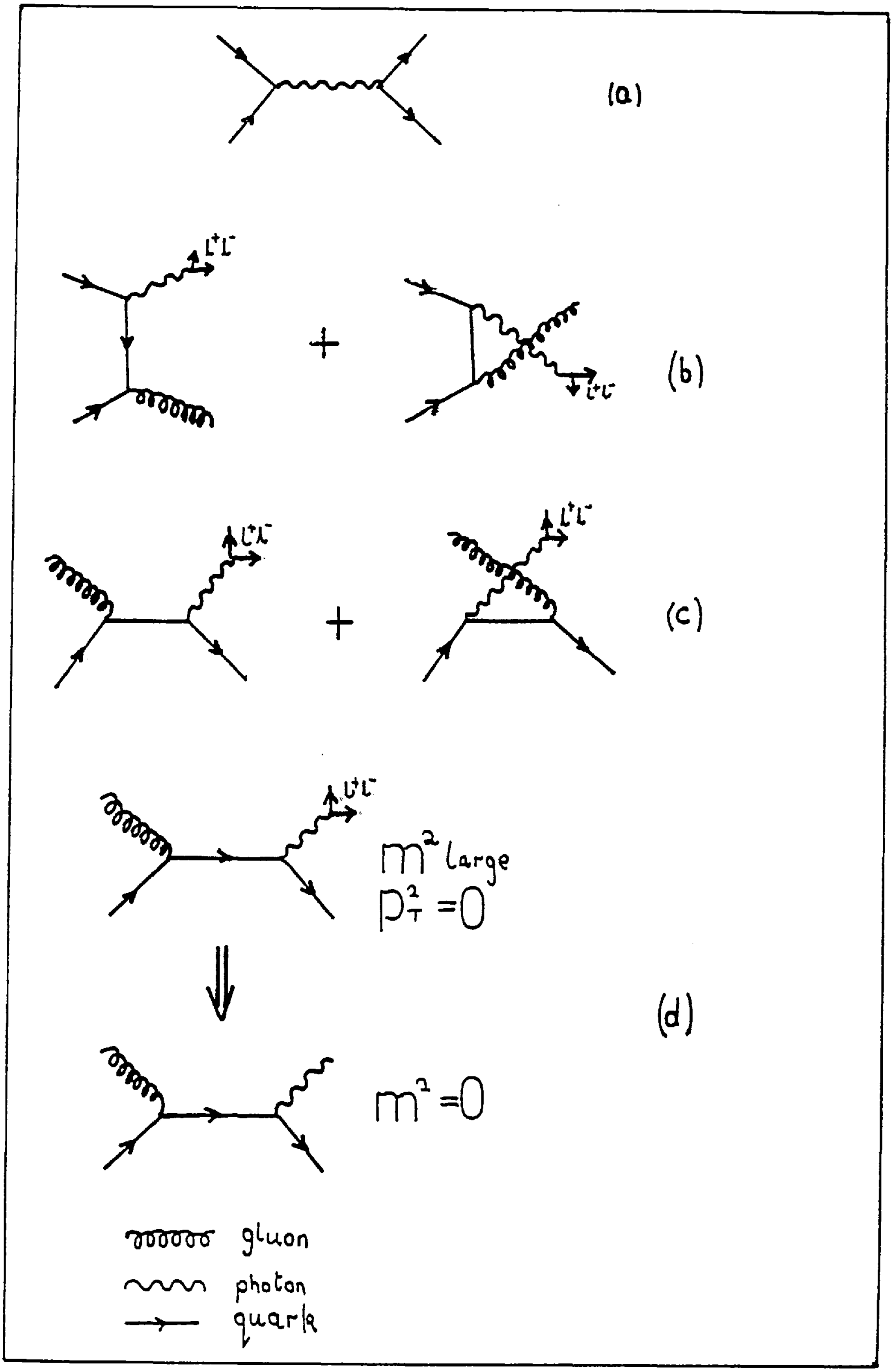

Fig 1.2

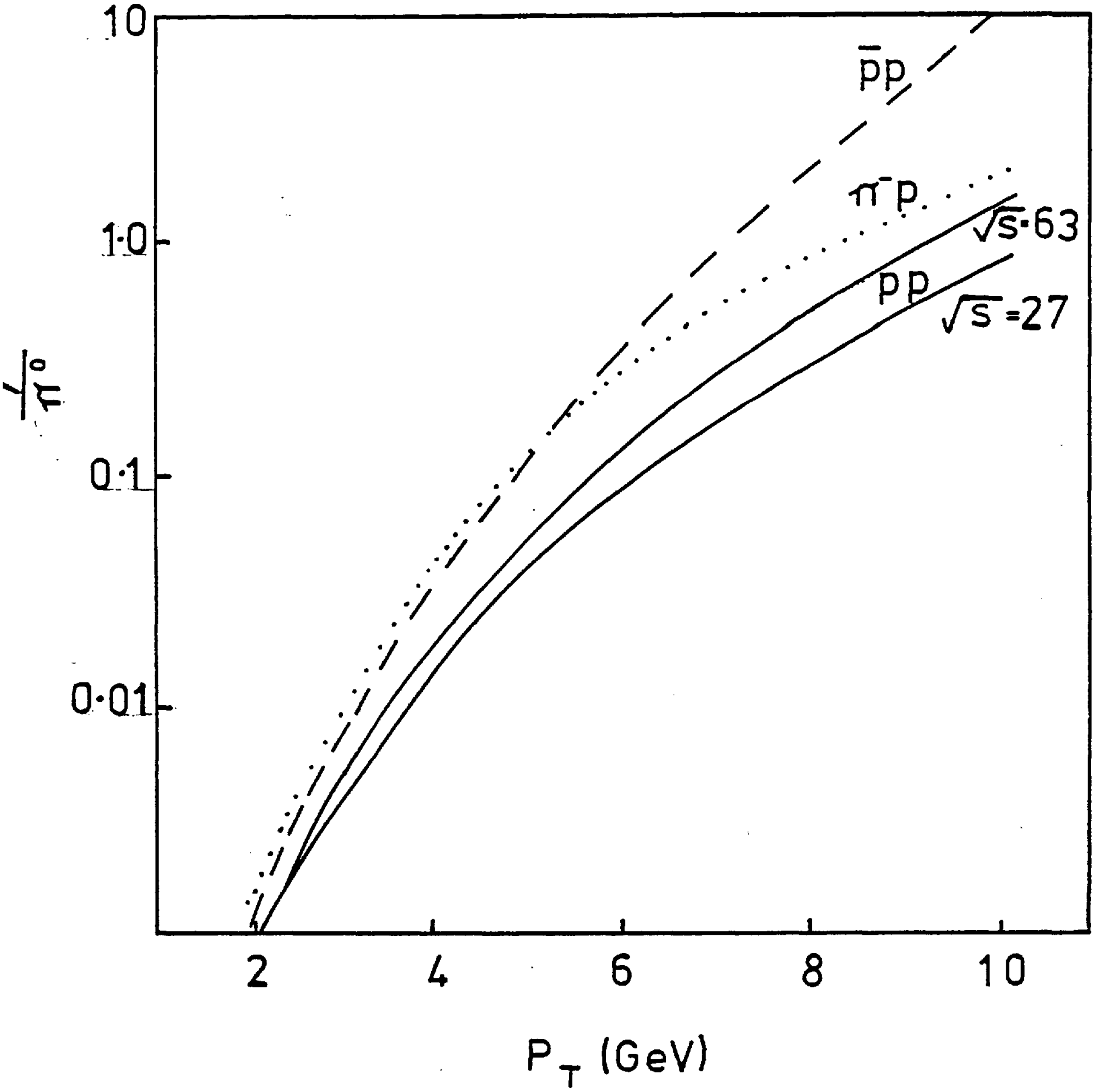
10
1.0
0.1
0.01
$\frac{\gamma}{\pi^0}$
$\bar{p}p$
$\pi^- p$
$\sqrt{s}$=63
pp
$\sqrt{s}$=27
2
4
6
8
10
P_T (GeV)

Fig 1.3

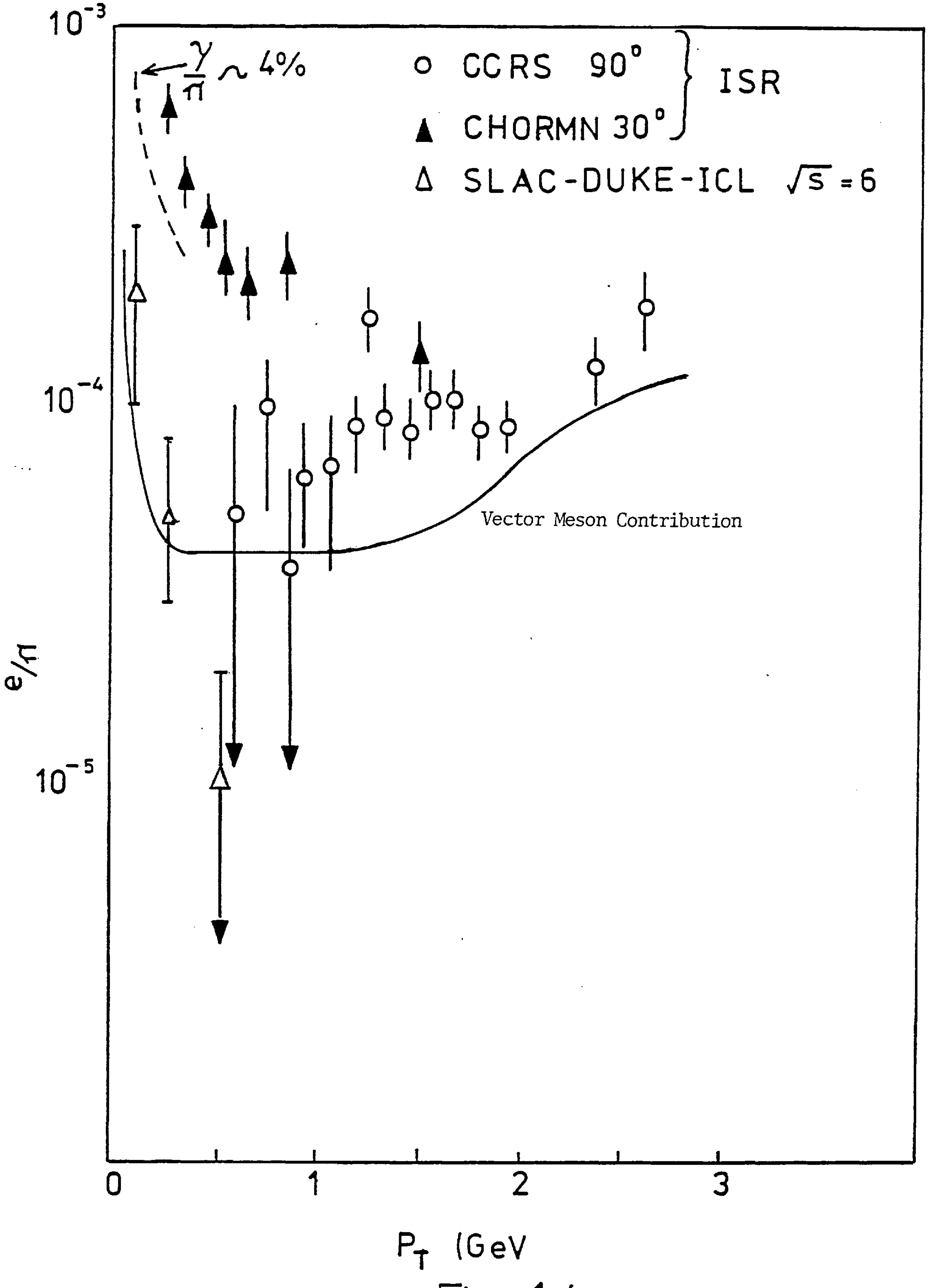

10^{-3}
$\frac{\gamma}{\pi} \sim 4\%$
○ CCRS 90°
▲ CHORMN 30°
ISR
Δ SLAC-DUKE-ICL $\sqrt{s} = 6$
10^{-4}
Vector Meson Contribution
e/π
10^{-5}
0
1
2
3
P_T (GeV

Fig 1.4

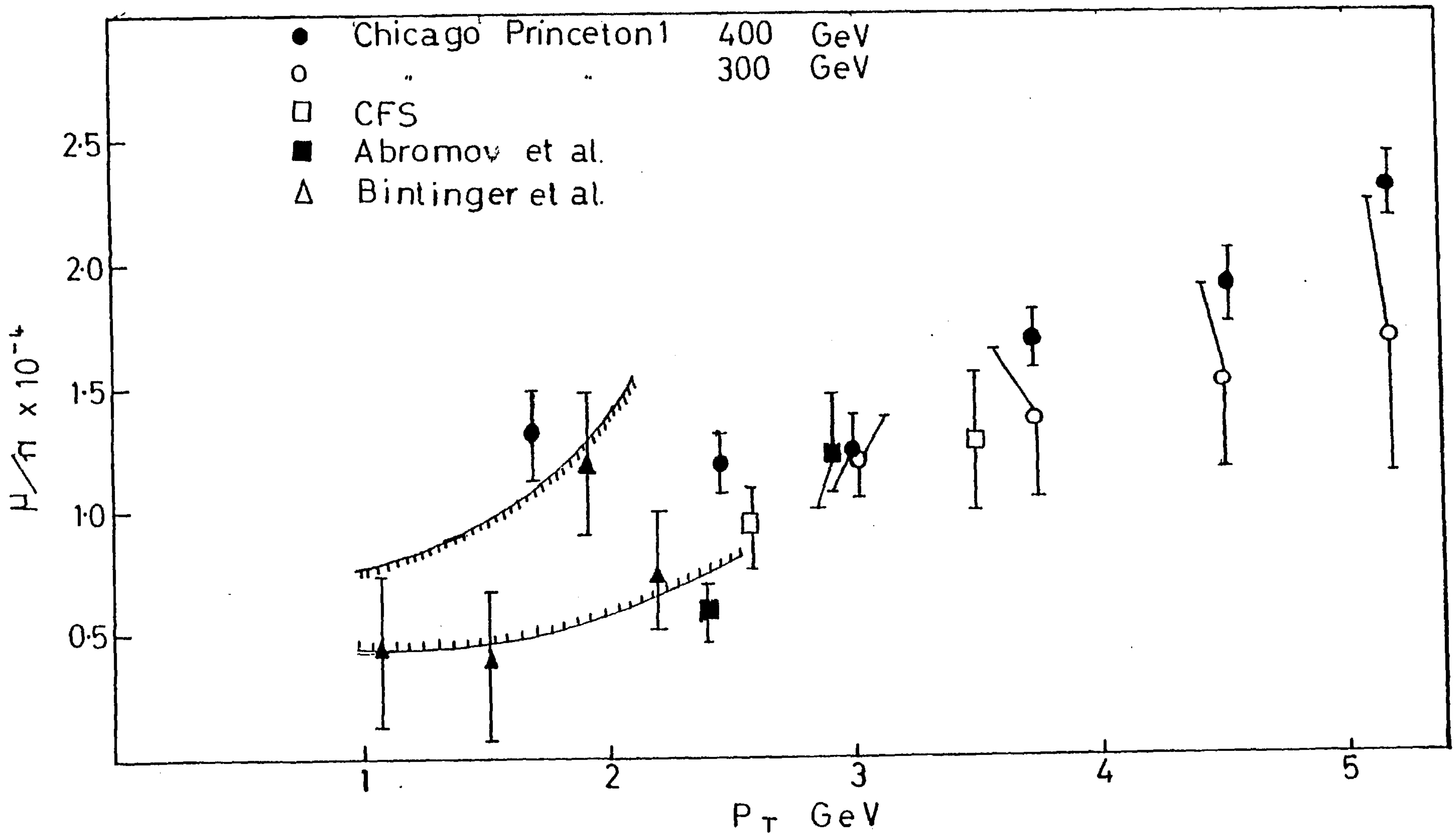

Chicago Princeton1 400 GeV
" " 300 GeV
CFS
Abromov et al.
Bintinger et al.
2·5
2·0
1·5
1·0
0·5
μ/π x 10⁻⁴
1
2
3
4
5
P T GeV

Fig1.5

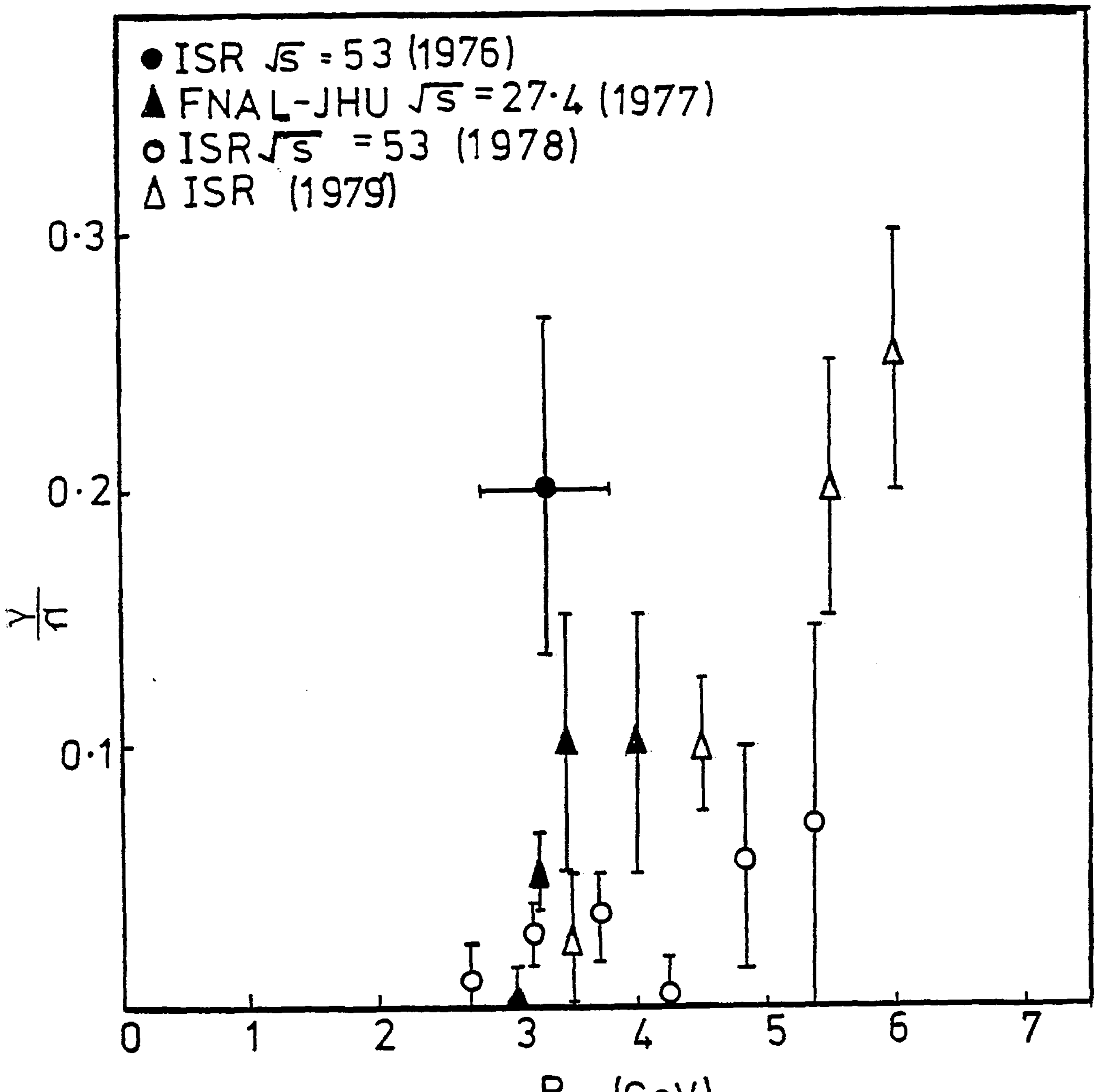
● ISR √s = 53 (1976)
▲ FNAL-JHU √s = 27·4 (1977)
o ISR √s = 53 (1978)
Δ ISR (1979)
0·3
0·2
0·1
γ/π
0
1
2
3
4
5
6
7
P_T (GeV)

Fig 1.6

CHAPTER 2

2.1 Introduction

This chapter describes the data collecting stages of the WA32 experiment at CERN. The proposal [1.24] had been submitted to the SPSC in August 1976 and was approved in October 1976, after the author had joined the Imperial College group. The run time for the experiment would be during one weekend concurrently with a neutrino run, BEBC being operated in the double pulsing mode. This would have been in February 1977 and though some film was taken at this time, it was not of sufficient quality, mainly due to multiple beam tracks, and so the run finally took place in late March 1977 once the S3 beam tagging system had become operational.

The first part of this chapter describes the S3 beam. This is a secondary beam from the SPS to produce hadrons for BEBC. As much has already been written on this beam [2.1,2.2,2.3], the description here is kept brief, covering only the important stages of the beam line itself. Next, the tagging system and its use in the identification of beam particles is described, and why it was used during the data collection.

Following this is a description of BEBC itself. Again detailed references already exist and it would be pointless to use too much detail here. This restricts itself to an overall view of the chamber and the mapping of the magnetic field. Then follows a discussion of the merits of the Ne/H_2 mixture used as chamber filling, and lastly the data taking itself is described.

2.2 The Beam

Whilst the proposal (1.24) asked for 100 GeV/c protons, the highest energy currently available at the time of the run was a 70 GeV/c fully separated proton beam.

The RF separated S3 beam to BEBC (2.1) was used. This beam line was designed to transport a maximum momentum of 150 GeV/c (unseparated) from target T7 to BEBC (see fig. 2.1). The beam has a total length of 900 m. Protons of momentum 200 GeV/c from the low momentum spill of the SPS impinge on target T7 and secondary particles then traverse the beam line as follows.

The layout is principally a classical three stage type: momentum definition of 0.2% provided in the first vertical bend; mass separation by three RF cavities, and cleaning and shaping of the beam before entering BEBC. The beam geometry is shown in fig. (2.3).

2.2.1 Momentum Analysis

A single vertical bend of 42.27mr. giving a dispersion of 2.2mm. for a $\Delta p/p$ of 0.1% provides the momentum analysis at the momentum slit.

Target dimensions:	vertical	2mm
	horizontal	1mm
Magnification at mom. slit		4.1
min. $\Delta p/p$ transmitted		±0.2%
Magnification at first horizontal slit		7.1

To increase the stability of this long beam against current fluctuation in the first quadrupoles, a horizontal focus has been added before RF1.

2.2.2 Mass Separation

Three RF cavities, used in pairs and operating in the 6000 MHz frequency range, achieve the mass separation in the horizontal plane. At the centre of each cavity is a focus of the target :

Magnification :	horizontal	7.7
	vertical	3.5

Between the cavities there are sets of quadrupoles yielding a magnification of (-1) in both planes. The complicated optics between RF2 and RF3 was principally due to civil engineering constraints.

2.2.3 Cleaning and Shaping

The third stage serves to clean and shape the beam before it enters BEBC.

Momentum redefinition is provided by means of a bending angle of 74.8mr. behind cavity RF3 and collimator C6 (which also acts as a beam stopper). Three superconducting bending magnets allow for a bend of about 55mr. at a distance of 59m. from BEBC.

In the last part of the S3 beam line a beam tagging system, consisting of two Cerenkov counters and two coded scintillation hodoscope counters, is incorporated.

2.3 S3 Beam Tagging System (2.4)

At momenta higher than 75 GeV/c, separation of kaons and protons is only partly efficient with the RF separator, and a tagging system including particle identification is necessary. Whilst in this experiment the separation of protons was complete, the tagging system was utilised for beam tuning, setting up of mass separation and for monitoring the purity of the beam during the run. As it was important to limit the number of beam tracks per frame to one, this was also used to veto the cameras in BEBC whenever there was more or less than one proton per pulse entering BEBC.

2.3.1 Basic Layout

The layout of the tagging system is shown in Fig. (2.4). Two threshold Cerenkov counters and two coded scintillation hodoscopes are located in a roughly 40m. long section after the last bending magnet. The Cerenkovs identify beam particles and the hodoscopes are for positional information. It is thus possible to identify incoming beam particles in a burst and to predict their entry point in BEBC. In an unseparated beam this is particularly important as only beam particles of a particular type (e.g. K^-, K^+, $\bar{p}$ etc.) need be looked for. All other beam tracks, not of interest, may be ignored. At these high energies, it is impossible for geometry/kinematics to identify the beam tracks from the film measurements and so the tagging system is important for this purpose.

In this particular case, the tagging system could identify the beam protons and veto the flashes should there either be more or less than one beam track or no incoming protons. At 70 GeV/c the proton beam was sufficiently well separated that no problems arose from K/p ambiguities, and one can be confident that all the beam particles on this experiment were protons.

In fact, from Hagedorn Ranft [(2.6)], the K^+/p ratio <u>at production</u> from the target is about 0.1 before any RF separation and $\pi^+/p \sim 1$. The separation between π^+ and p is complete (π's being removed by a beam stopper), and the K^+'s are effectively removed.

2.4 Big European Bubble Chamber (BEBC) [(2.3)]

The general layout of BEBC is shown in fig. (2.5). The bubble chamber is a large upright container 4m. high, 3.7m. in diameter with a hemisphere at the top containing the window for the five cameras and an expansion piston at the bottom. On earlier experiments a ring of parasitic bubbles covered the piston ring and teflon dust, also causing bubbling, covered the piston head, thus causing poor picture quality. For recent experiments (including this), these problems have been removed by covering the bottom of the chamber above the piston with a floating disc.

The chamber vessel is surrounded by a cylindrical vacuum tank 3.2m. in diameter and 9.2m. high. The magnetic field is generated by two superconducting magnets, cooled by liquid helium. Iron shielding of 2000 tonnes and 40cm. thick surrounds the entire structure.

2.4.1 Magnetic Field

Two superconducting coils, capable of producing magnetic fields of up to 3.5 Tesla surround the chamber. The mapping of the field inside the $22m^3$ fiducial volume by direct measurement had, at the time of the experiment, not been done. However an array of 181 Hall probes have been placed on the boundary surface. As there are no magnetic materials within the chamber volume, field measurements on the closed boundary will allow the field to be calculated at any point within the chamber. A least squares fit of the resulting field values to a Legendre polynomial series, yields a set of coefficients which allow the field to be evaluated at any point within the fiducial volume to an accuracy $\Delta B/B \sim 10^{-3}$.

This system allows any variation of the field during an experimental run to be observed and corrected for.

2.4.2 Optics

Mounted on the top of the chamber, arranged in a regular pentagon are five optical units: four of these have wide angle lenses with annular flash tubes rigidly connected to the film transport system and a data box. In the fifth is a periscope. Each camera sees the useful volume of about $22m^3$ and the stereo angle, achieved with an optical axis inclined by 13^o to the chamber axis, has been chosen such that, irrespective of their direction, tracks in space can be reconstructed with a precision better than 0.3mm. despite the vibration of the chamber vessel and temperature gradient in the structure.

2.4.3 Illumination

The optical system for BEBC is such that bubbles of less than 1mm. diameter will show up against the background when photographed. As the refractive index of the cryogenic liquids ($n \sim 1.1$) differs only slightly from the vapour bubble ($n \sim 1.0$), this is not easy and so for various reasons "bright-field" illumination is used. The principle of this is as follows: light after passing through the liquid enters the entrance pupil of the lens and darkens the film. If any obstacle is in the path of the light, e.g. a bubble, then nearly all the light is scattered away from the lens. Thus bubble tracks appear as bright lines on a dark background.

Scotchlite is used to wallpaper the inside of the chamber vessel. This is a retro-directive reflecting material, and makes possible the homogeneous illumination of the chamber with small light sources, which are rings around the lenses.

2.4.4 Data Box

In order to identify each frame and view on the film, a data box is incorporated into each camera providing information concerning the film, photo, camera number and operating conditions. This information is provided by means of binary and alphanumeric coded light signals projected onto the film when a photo is taken. The information contained is :

View number
Frame number
Roll number

Also two binary bits are set if the frame is a hadron picture. This assists film scanning when BEBC has been used in a double pulsing mode.

2.4.5 Use of BEBC Filled with Ne/H_2

In order to perform this experiment, a high gamma detection efficiency was the major requirement. A bubble chamber with a hydrogen filling does not have the necessary gamma conversion length to perform a short experiment: instead of 6000 frames, at least ten times this number would be required in order to achieve the same sensitivity. A heavy liquid on the other hand has a much shorter radiation length than hydrogen, and consequently a much higher gamma detection efficiency. Because of the demands of the narrow band neutrino collaboration, it was necessary to perform the experiment with a 74% molar Ne/H_2 mixture. The advantages, and drawbacks, of this mixture are outlined below:

advantages -

1) high gamma detection efficiency. The radiation length for an electron in this mixture is 42cm.[2.7], consequently the gamma conversion length is 56cm. This comes from the formula[2.5]

$$\frac{\sigma_{brem}}{\sigma_T} = \frac{4 \ln G + 2/9}{28/9 \ln G - 2/27}$$

where σ_{brem} = bremsstrahlung cross-section (α 1/radiation length)

σ_T = gamma conversion cross-section (α 1/conversion length)

$G = 183/Z^{1/3}$

for Z of 10 this is approximately 9/7.

With the fiducial volume chosen the theoretical gamma detection efficiency was about 96% (see Chapter 3).

2) With a 40mb proton-proton cross-section the interaction length for a beam particle would be 140cm.[2.7]. Thus approximately 40% of frames should have had a primary vertex in the fiducial volume. This would mean less wastage of film.

3) Good gamma identification. This is dealt with in greater detail in Chapter 3 but the e^+e^- pair from a converting gamma are easy to identify thus aiding scanning and reconstruction.

Problems of using Ne/H_2 -

1) Short interaction length leads to large numbers of secondary scatters of the hadrons. This leads to obscuration of the film, making scanning for gammas difficult, particularly near the primary vertex.

2) The short radiation length leads to electrons from converted gammas producing bremsstrahlung gammas which also convert in the chamber. This adds more obscuration, produces background gammas, and, where an electron radiates close to the gamma vertex, makes measuring electron tracks harder.

3) Multiple scattering is much more important than in hydrogen, causing reconstruction problems.

2.5 Data Taking

In late February 1977 some five thousand frames were taken in BEBC. The author was not present on this run and the beam tagging system was not used. The film from this run was virtually unmeasurable. Most frames had more than one interacting beam track and the resulting visual confusion was such that it was decided not to use this film.

In mid March 1977 the author was at CERN for the main data taking. This was during an anti-neutrino run for the WA19 collaboration so that BEBC was double pulsing. BEBC was filled with a 74% molar Ne/H_2 mixture with a corresponding radiation length of 42cm. (gamma conversion length 56cm.). The S3 beam tagging system was in operation such that the BEBC camera flashes operated when only one beam track entered the chamber.

The beam was tuned in the way described in ref. (2.3) section BEAM/102, the beam profile as shown in fig. (2.7). The central peak, from π's and K's is removed by means of a beam stopper, the wings, from protons being left. The protons then passed through a series of vertical and horizontal collimators. The separation of these was adjusted such that an average of 1 proton per pulse entered BEBC. From Poisson statistics

$$P(n) = \frac{m^n e^{-m}}{n!}$$

for a mean of 1, 37% of pulses will have 1 beam track. This maximises the number of photos taken in a given time.

Approximately 6000 frames were taken before the termination of the cycle.

REFERENCES

2.1 H. Atherton et al. CERN / D.Ph. II / BEAM 73 - 5

2.2 P. Bernard et al. CERN / D.Ph. II / BEAM 72 - 3

2.3 BEBC Users Handbook

2.4 I. Lehraus. CERN / EF / BEAM 76 - 3

2.5 Heitler Quantum Theory of Radiation 3rd ed.
(Oxford Univ. Press 1954)

2.6 Grote - Hagedorn - Ranft, Particle Spectra. CERN 1970

2.7 H. Leutz et al. CERN 74 - 20

FIGURE CAPTIONS

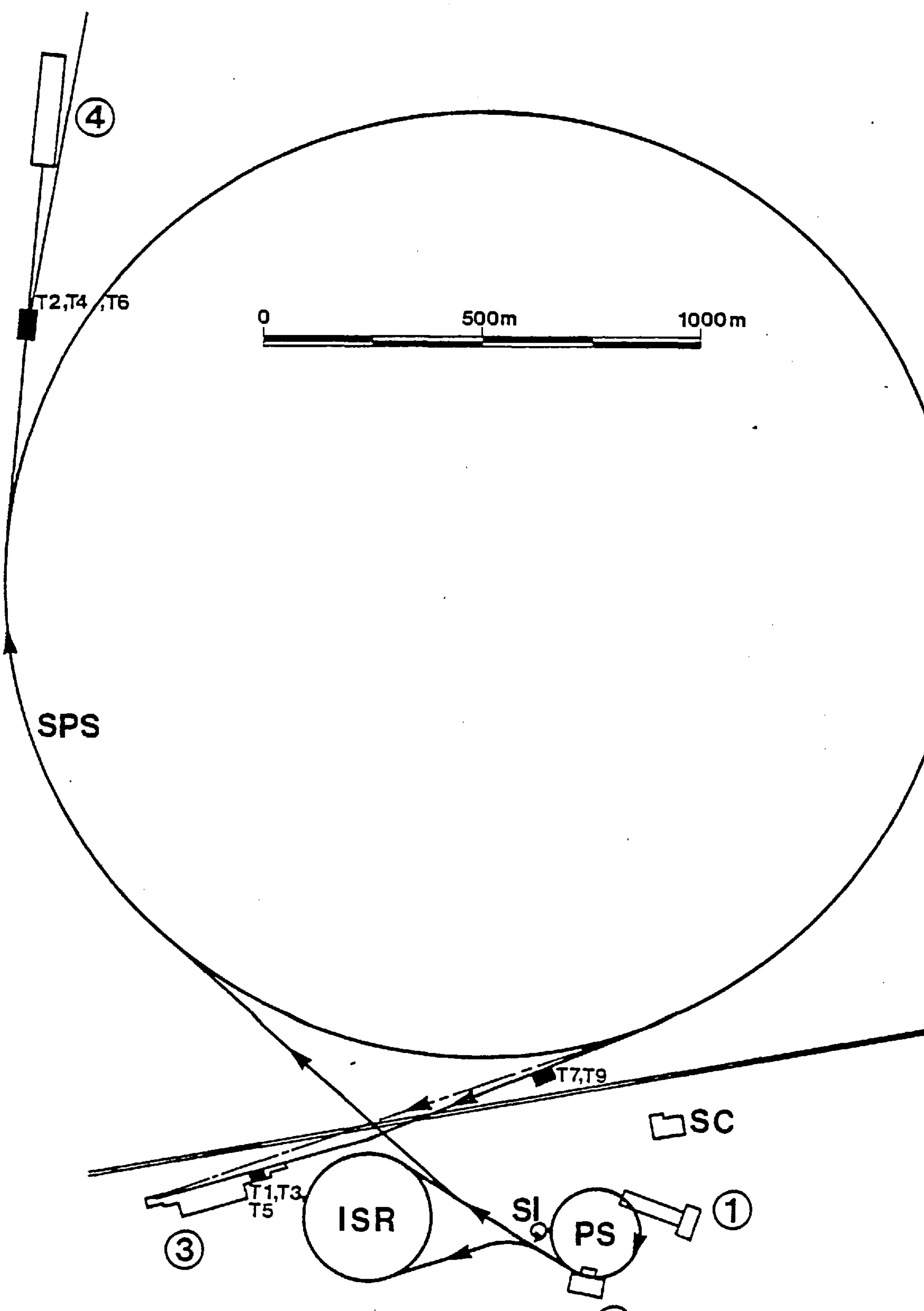

Fig 2.1

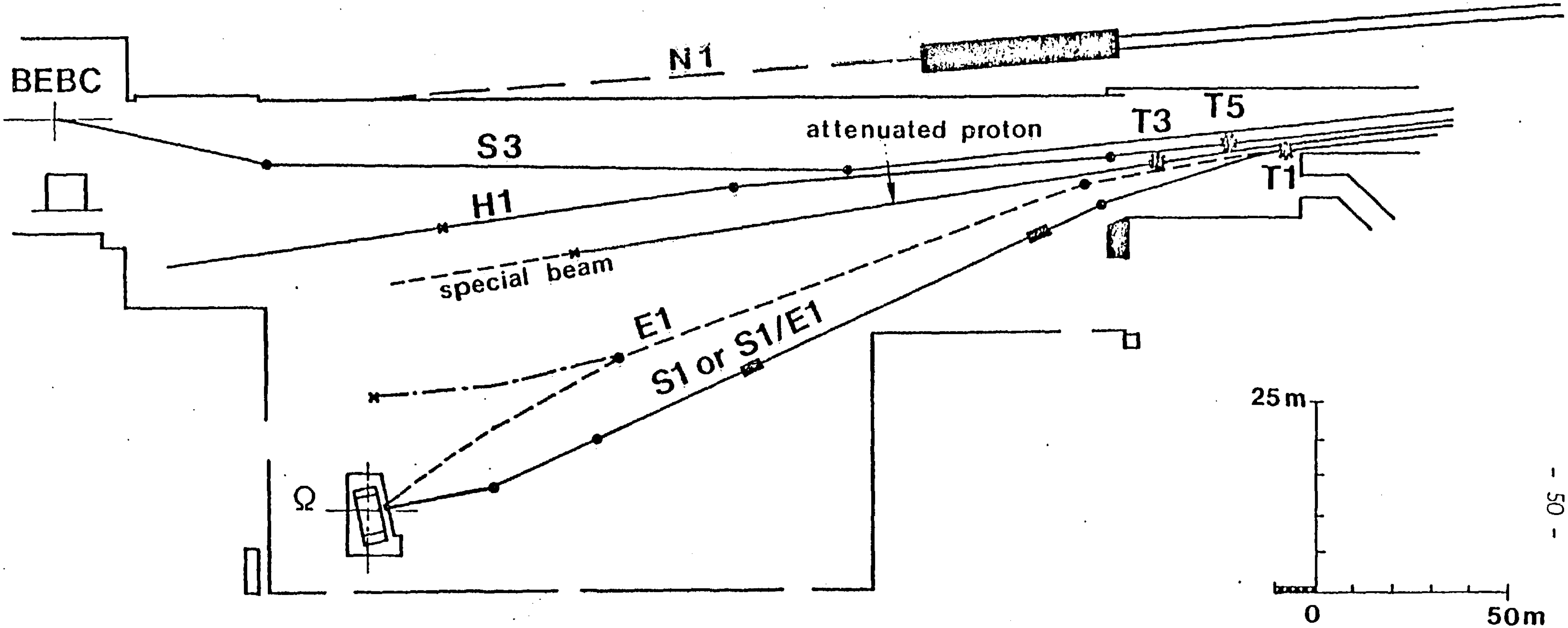

SPS WEST EXPERIMENTAL AREA

GENERAL LAYOUT

Fig 2.2

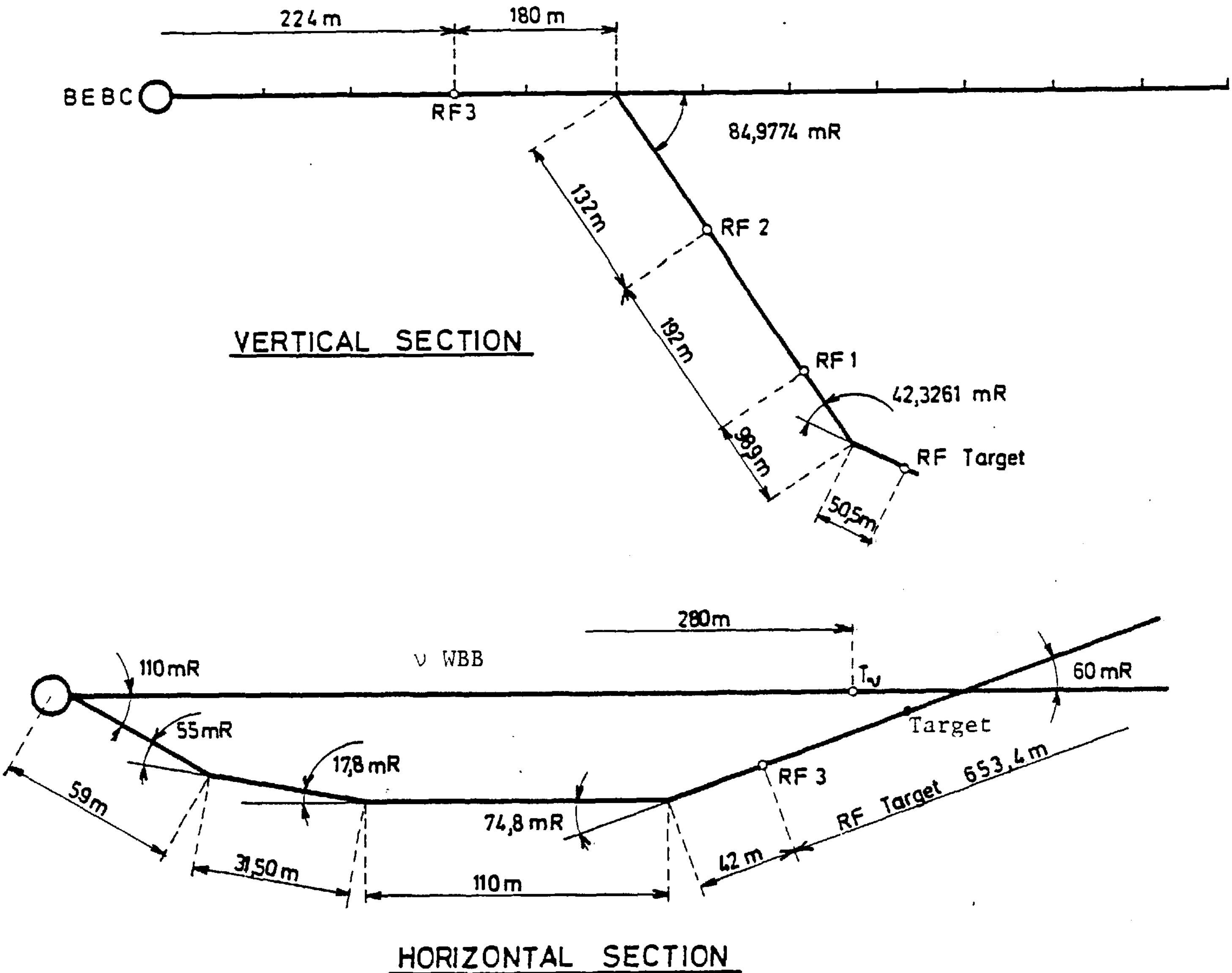
224 m
180 m
BEBC
RF3
84,9774 mR
132m
RF 2
VERTICAL SECTION
192m
RF 1
42,3261 mR
98,9m
RF Target
50,5m
280m
ν WBB
110 mR
T_ν
60 mR
55 mR
Target
17,8 mR
RF 3
653,4 m
59m
74,8 mR
RF Target
42 m
31,50 m
110 m
HORIZONTAL SECTION

Fig 2.3

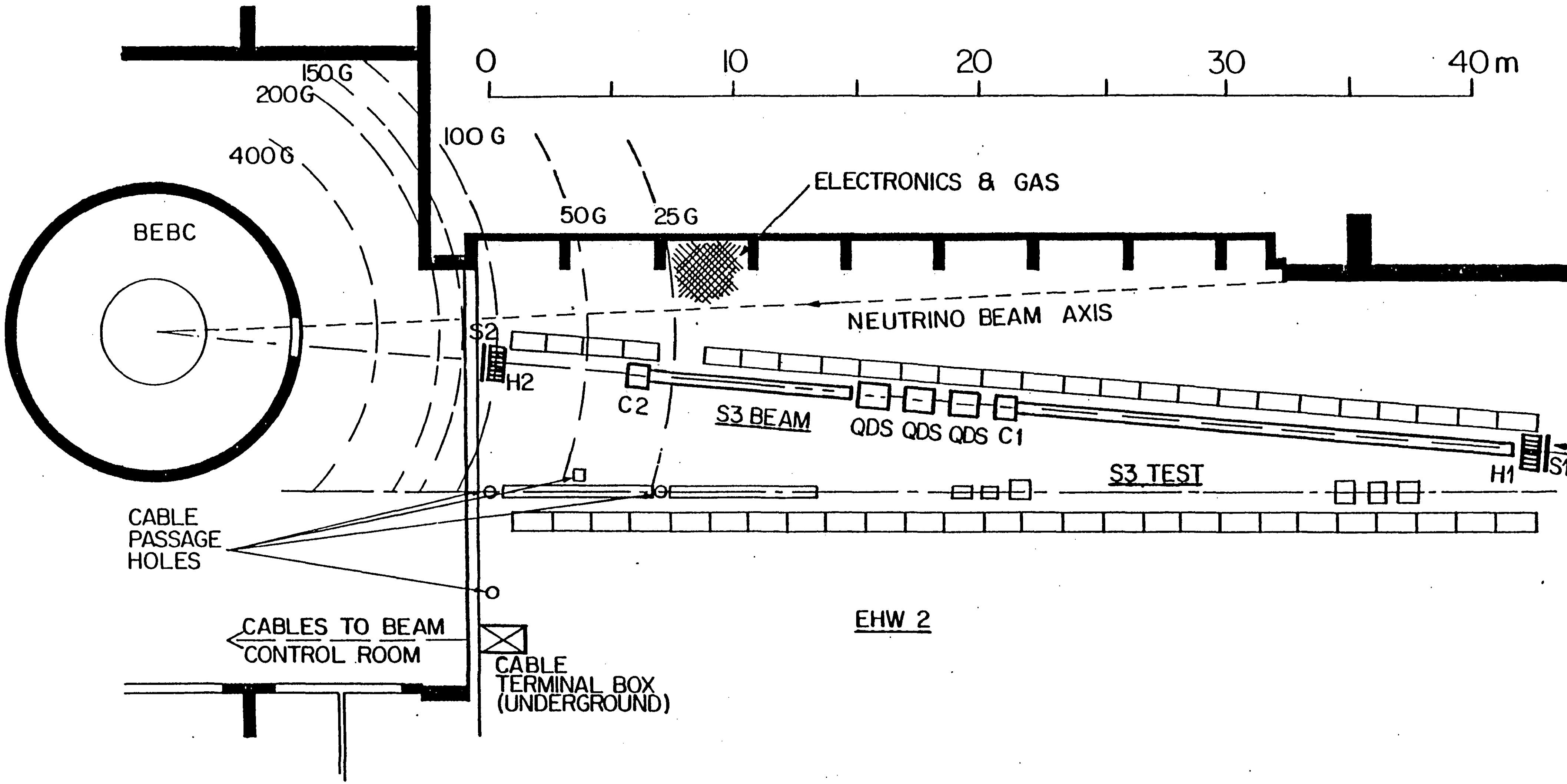
0
10
20
30
40 m
150 G
200 G
400 G
100 G
50 G
25 G
ELECTRONICS & GAS
BEBC
NEUTRINO BEAM AXIS
S2
H2
C2
S3 BEAM
QDS QDS QDS C1
H1
S1
S3 TEST
CABLE
PASSAGE
HOLES
EHW 2
CABLES TO BEAM
CONTROL ROOM
CABLE
TERMINAL BOX
(UNDERGROUND)

Fig 2.4

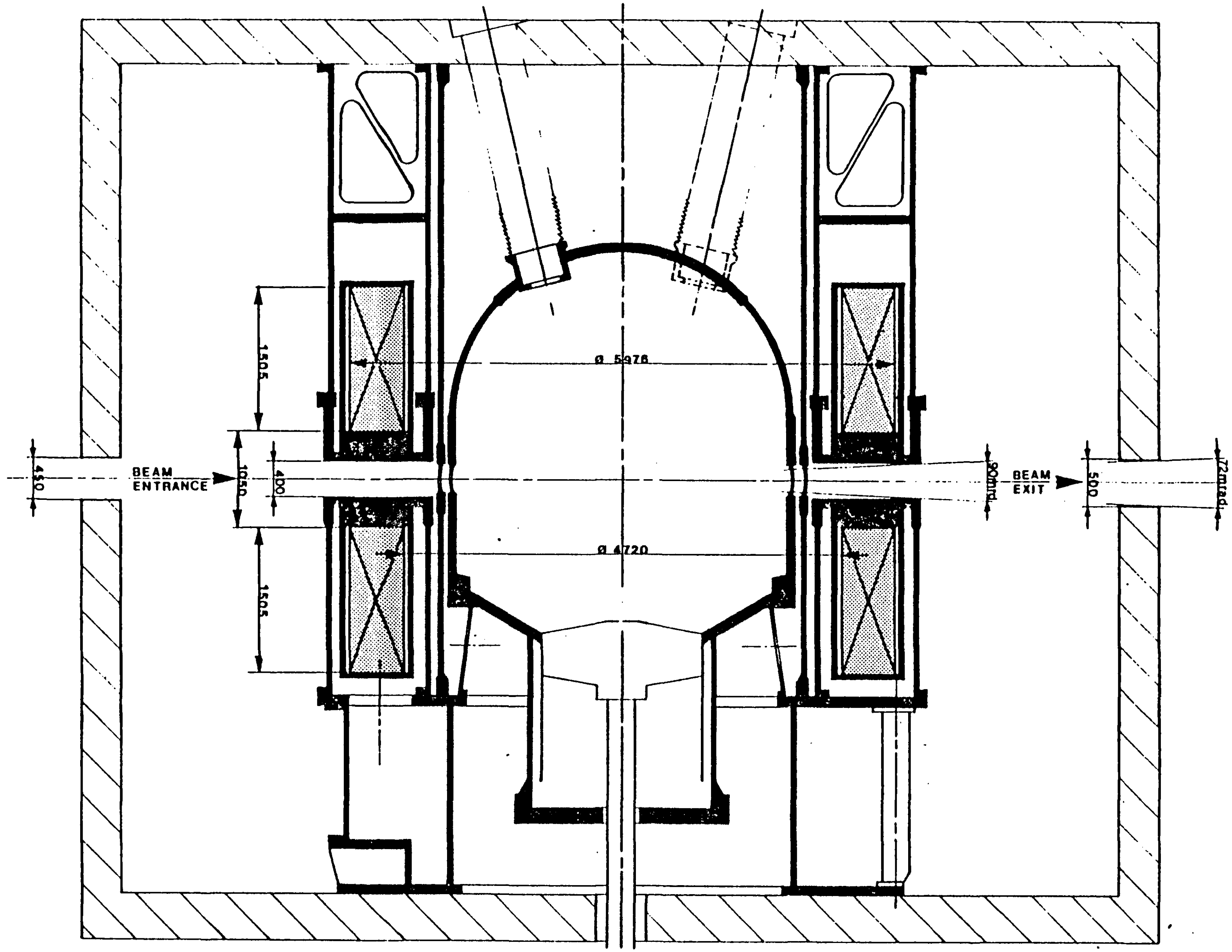
BEAM
ENTRANCE
BEAM
EXIT
Ø 5976
Ø 4720
1505
1505
1050
400
450
500
90mrad
72mrad

Fig 2.5

Fig. 2.6 (overleaf)

Picture of the BEBC interior on view 2 at the time of this experiment. The DATA BOX is visible above the Brenner mark: the lower left hand two digits are the hadron bits, used during this experiment to distinguish proton frames from anti-neutrino frames.

The event on this frame is typical in both hadron and gamma multiplicities.

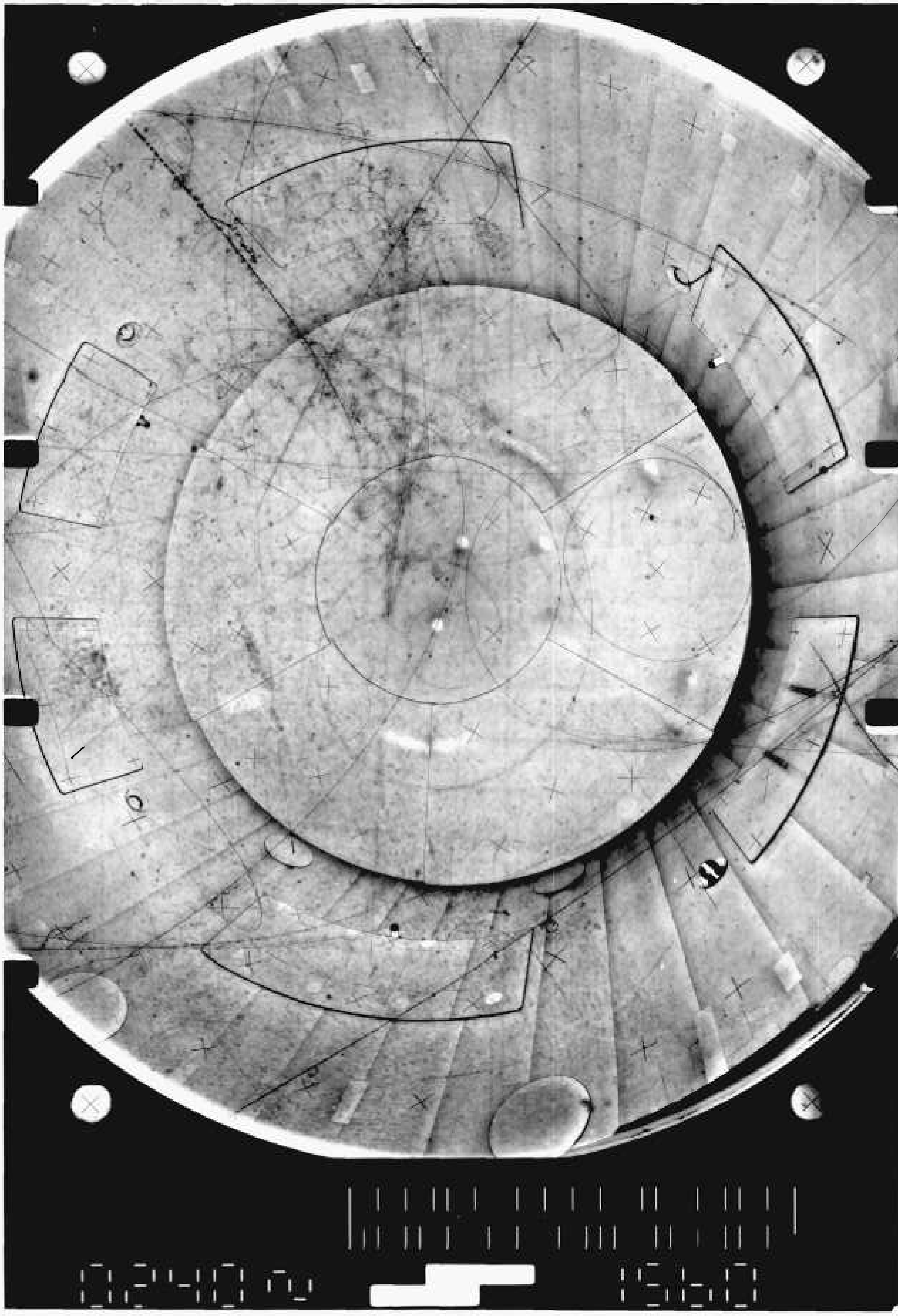

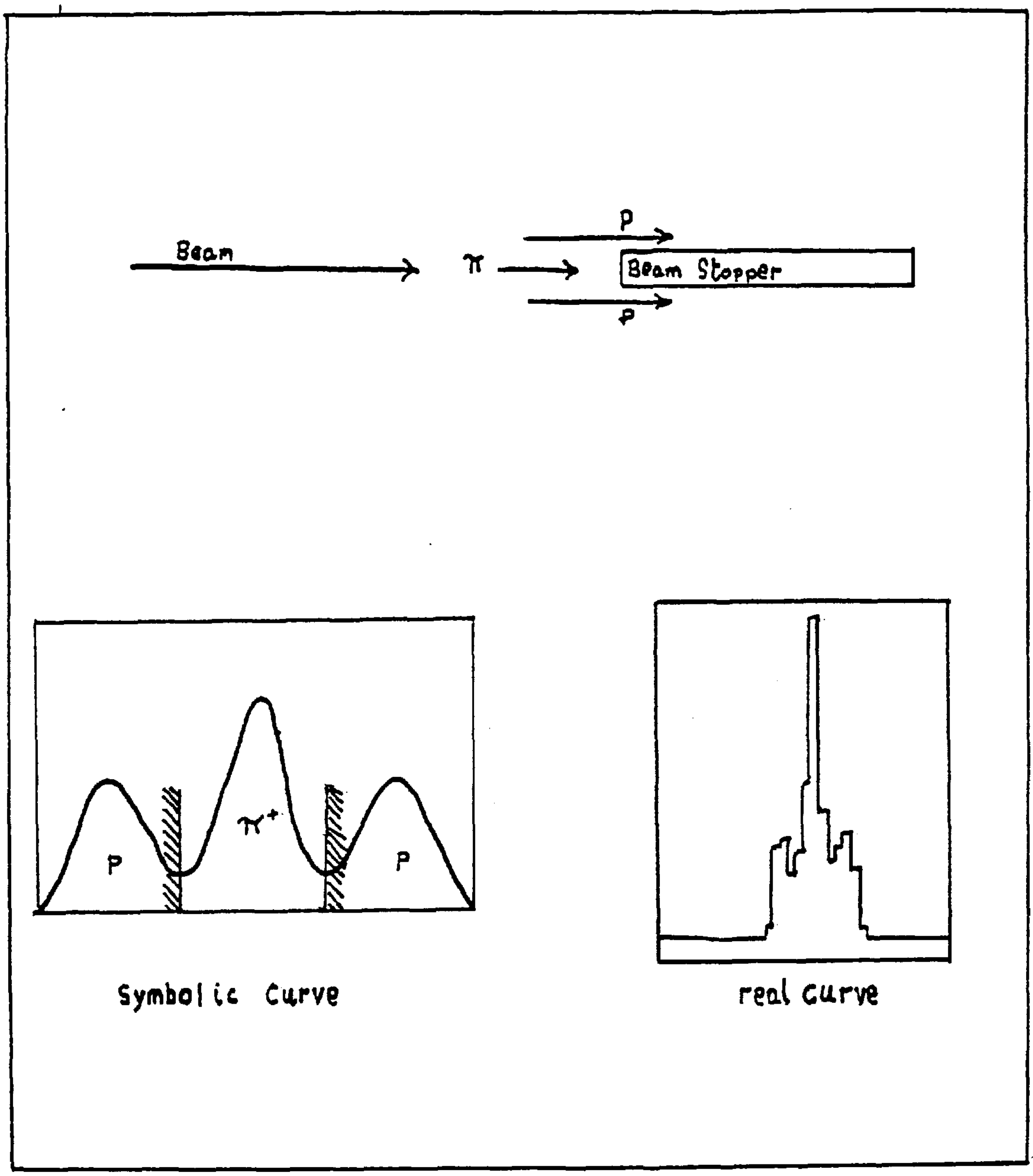

Fig 2.7

CHAPTER 3

3.1 Introduction

This chapter describes the scanning and measuring of the film. The criteria for event selection are presented and the choice of fiducial volume discussed. Gamma identification in BEBC is then described in detail as this is crucial to the success of this experiment. The online measuring system developed at Imperial College for measuring high energy/high multiplicity events is described.

3.1.1 Event Selection

As the proton film had been taken at the same time as an anti-neutrino run, with BEBC in double pulsing mode, it was necessary to have a means of distinguishing the two, apart from the presence of an incoming beam track. This was provided for by the two lower left hand side bits in the BEBC data box being set for proton frames. Thus any BEBC frame with these bits not set was ignored. Events were chosen such that a high energy incoming particle with angles consistent with that of the beam, interacts with the chamber liquid in BEBC regions A5 or A6 on view 2, (fig. 3.1), and with one or more photons converting in the chamber. As the track vectors of charged hadrons from the interaction were irrelevant for present purposes, they were not measured, though charged multiplicities were noted. The advantage of this was to speed up the measuring process: if hadron tracks were measured as well as gammas, the time taken to measure an event would be much longer. The disadvantage, as pointed out later, is that geometrical constraints on the event as a whole, to better determine position of the primary vertex cannot be imposed.

If charged hadrons from the primary vertex had been measured, information on π^+ and π^- inclusive distributions would be available and ready to compare with, and normalise inclusive π^0 distributions. This information, however, is not available and consequently should be remembered when π^0 inclusive distributions are discussed. The charged multiplicity is known and this can give some independent indication of the true π^0 multiplicity. However, when considering such quantities as γ/π^0 and η/π^0, corrections can be made or can cancel out.

3.1.2 Fiducial Volume

The fiducial volume was chosen such that gammas had a minimum potential decay length of 150cm. This volume ran from -120 to +30 cm. with respect to the chamber centre along the beam direction. Any proton interaction with the liquid in this region would be selected.

It was found that scanning for events in BEBC regions A5 and A6 on view 2 was sufficient to impose this fiducial cut. The vertex distribution is shown in fig. 3.2.

Monte Carlo studies using this fiducial volume were carried out: protons of 70 GeV/c were allowed to interact within the fiducial volume and π^0 with a range of x and P_T produced. These decayed into 2 gammas which were then followed to see if they would convert inside the chamber. The only assumptions necessary were the p-Ne collision length and the γ conversion length in Ne/H_2 of this density. These are taken from ref. (2.7).

3.1.3 Potential Detection Efficiency

This study showed that the average potential detection efficiency in the absence of all other factors was 96.5% for one gamma. (i.e. 3.5% of all gammas leave the chamber.) Thus the potential detection efficiency for both gammas from a single π^0 was 93% and for all gammas from $3\pi^0$, the expected average number of π^0's per event, would be 80%. This study neglects effects such as scanning near the vertex, obscuration due to multiple scattering, electromagnetic showers as a result of bremsstrahlung, secondary hadron interactions etc. These are difficult to calculate from a Monte Carlo study and can only be estimated. Other effects reducing the number of gammas in the final analysis are measurement/reconstruction efficiencies. These problems will be discussed in Chapters 4 and 5.

3.2 Scanning

The film was doubly scanned to find events within the fiducial volume under consideration. This was defined for the scanner to be any interaction within the regions A5 and A6 of view 2 (see fig. 3.1). The scanning efficiency for events in these regions was effectively 100%.

Drawings were made of the events in order to direct the measuring. At first it was decided to use a template in order to measure only events with a likely high P_T gamma (i.e. $P_T > 0.5$ GeV/c).

However as only by measuring was it possible to find the P_T of the gamma and also in order to study π^o and η production at various P_T ranges, it was decided to measure all gammas on all events within the fiducial volume.

3.2.1 Gamma Identification (3.1)

A heavy liquid bubble chamber with a high magnetic field affords excellent identification of gammas. The electron tracks from a converting gamma have several distinct signals, see fig. 3.3:

1) Spiralisation - this results from the electron radiating its energy and spiralling inward in the magnetic field.

2) Bremsstrahlung is also a good electron identifier: a minumum ionising track which suddenly kinks, sometimes producing a downstream gamma is almost certainly an electron.

3) Trident formation.

4) Large δ rays.

5) Vanishing positive tracks.

The advantage is that there is virtually no γ/V^o ambiguity, the V^o's having very different signals such as denser track multiple scatters, and secondary interactions. This makes kinematic reconstruction very much simpler as only electron and gamma hypotheses need be attempted on the measurements.

3.3 Online Measuring (3.2,3.3)

Events were measured on a conventional BESSY measuring machine, using online control and geometrical reconstruction programs. The control program directs the measuring using information supplied to it by the measurer. Points on each track are transmitted to the control program which then passes them on to the online geometry program (OLGA) which reconstructs the track in space. The parameters of the reconstructed tracks are returned to the control program which performs tests to see whether the track has been measured well enough for offline reconstruction or whether more and/or better measurements are required. In the former case, the program then asks for the next track to be measured; in the latter case the program demands more points. The process of measurement and reconstruction continues until the program is satisfied that either the measurements are good enough for offline geometry/kinematics to reconstruct the track, or that subsequent remeasurement will not improve track reconstruction.

A typical frame would be measured as follows: the control program asks for the BEBC ROLL/FRAME number, how many primary vertices, gammas etc. are on the frame and draws up an "item" list which will be processed in order. Then it demands that the fiducials on each of three views be measured. In order to have accurate measurements over the whole chamber, 18 fiducials were measured on each view (see fig. 3.4). If any fiducial is badly measured, (i.e. not within a given tolerance of where the program expects it to be), it is remeasured.

Next the primary vertex of the proton-Ne interaction is measured as well as the incoming beam track on each view and geometrically reconstructed. After these have been successfully measured then the gammas on the frame are measured one by one. Should the measurer see gammas on any frame not found at the scanning stage, they are added to the item list.

After each item has been measured the control program "wakes" OLGA up to reconstruct them. A flow diagram for the measuring process is shown in fig. 3.5.

3.3. 1 Hardware

This whole process is performed using the PDP10 computer of the Imperial College High Energy Nuclear Physics Group. Both the control program and OLGA are running on this machine, though for most of the time OLGA is in a state of hibernation, running only when there are tracks to be reconstructed. The PDP10 is interfaced with the measuring machine by a PDP8F computer. This accepts measurements from the BESSY machine and transmits them to the control program. The control program communicates with the measurer on a normal teletype. Both PDP8 and teletype are physically interfaced with the PDP10 by way of a teletype line distributor (DC10). This system is flexible enough to allow several machines to measure online simultaneously. A schematic diagram of the system is shown in fig. 3.6.

3.3. 2 Item Comments

After each item has been measured, the measurer may comment it: e.g. for a gamma, the measurer types in G when the control program asks for this vertex to be commented. This is to aid both online and offline reconstruction. Should an item be commented as a gamma then only electron hypotheses need be attempted in the track reconstruction and a gamma (as opposed to a V^0) hypothesis attempted on the vertex itself. This allows much greater speed and flexibility in the measuring process.

Rapport between control program and measurer is also allowed up to a certain level. Should an item become very difficult for OLGA to reconstruct, making many attempts at improvement, the measurer is allowed either to skip the item and go to the next, or to erase completely the existing measurement and start that item again.

When each item has been measured the control program writes it to disk, wakes up OLGA, which reads these measurements, reconstructs them and writes the parameters of the reconstructed track back to disk. These are then read by the control program. Once an item has been satisfactorily measured it is written to another disk file containing all measurements for that event, and when a whole frame has been measured the whole event is appended to a disk file containing all measurements for that roll.

The next stage is the offline reconstruction which will be described in the next chapter.

REFERENCES

3.1 K.W.J. Barnham IC / HENP / PN / 52

3.2 S. Banerjee ' Online Geometry for Conventional Measuring Machines ' IC / Programming Note / 9 1977

3.3 S. Banerjee ' Present Status of Online Geometry ' IC / Programming Note / 11 1977

FIGURE CAPTIONS

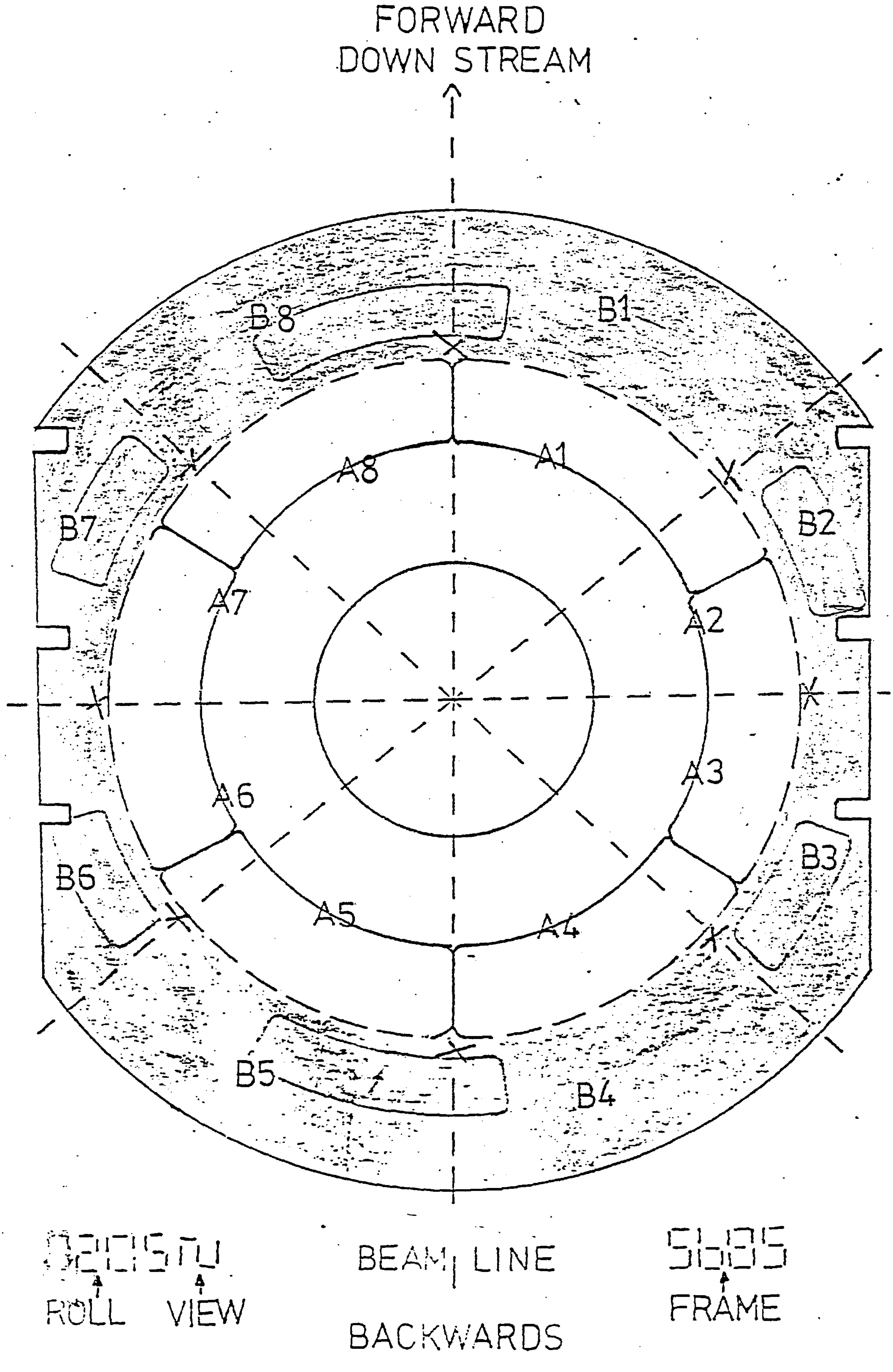
FORWARD
DOWN STREAM
B8
B1
A8
A1
B7
B2
A7
A2
A6
A3
B3
B6
A5
A4
B5
B4
020ISTU
ROLL
VIEW
BEAM LINE
5635
FRAME
BACKWARDS

Fig. 3.1

PRIMARY VERTEX DISTRIBUTION IN BEBC

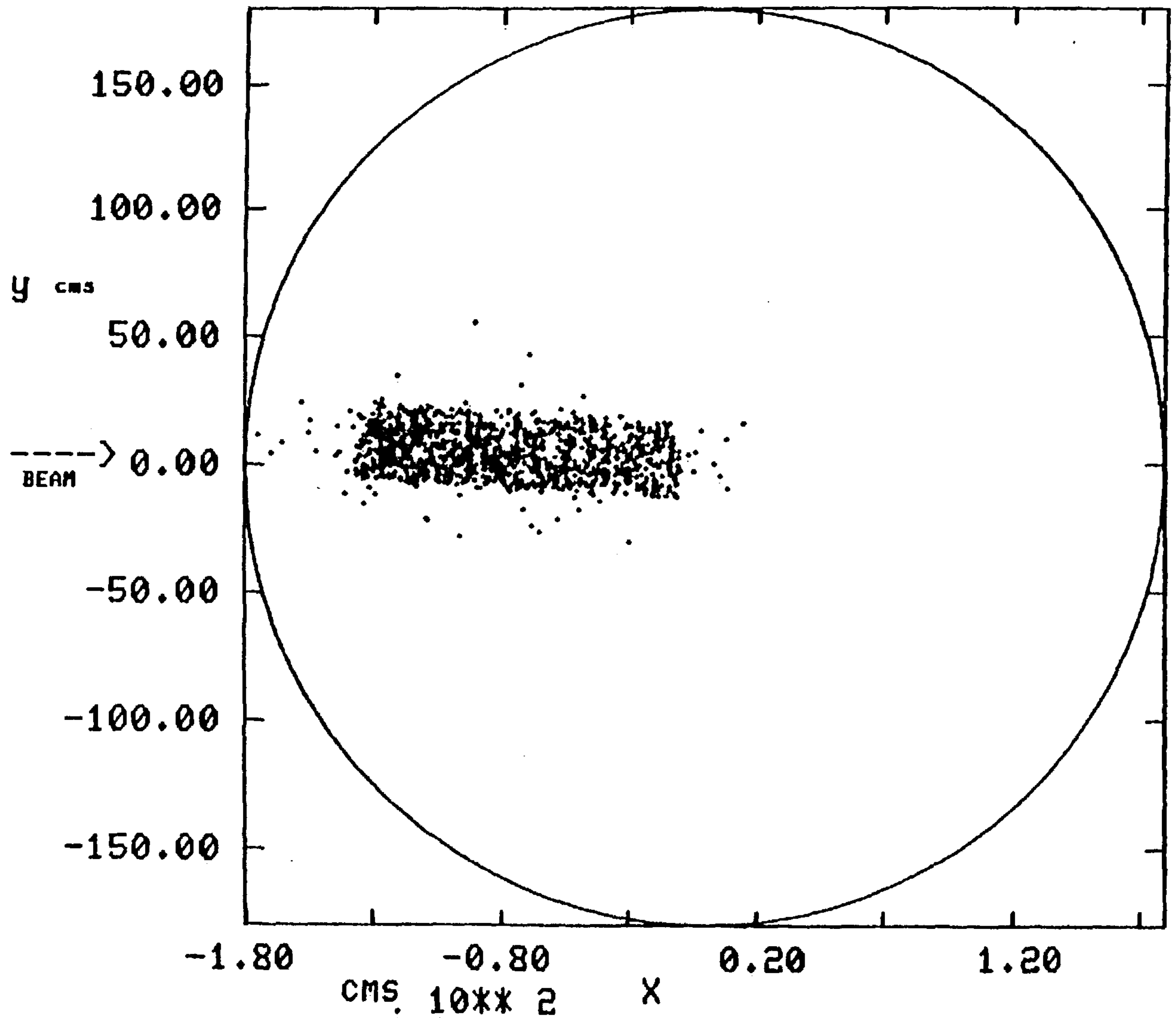

Fig 3.2

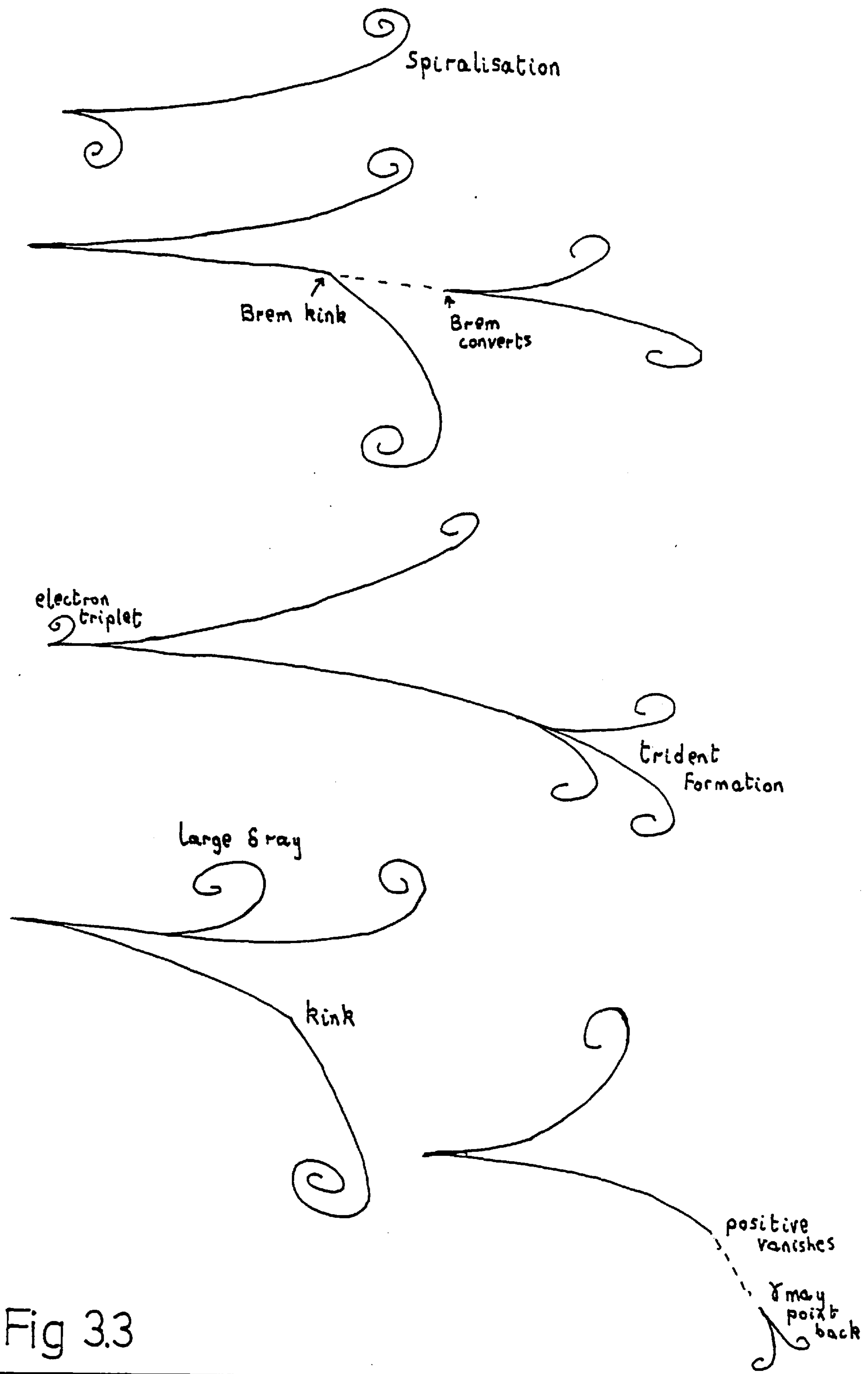
Spiralisation
Brem kink
Brem converts
electron triplet
trident formation
large δ ray
kink
positive vanishes
γ may point back

Fig 3.3

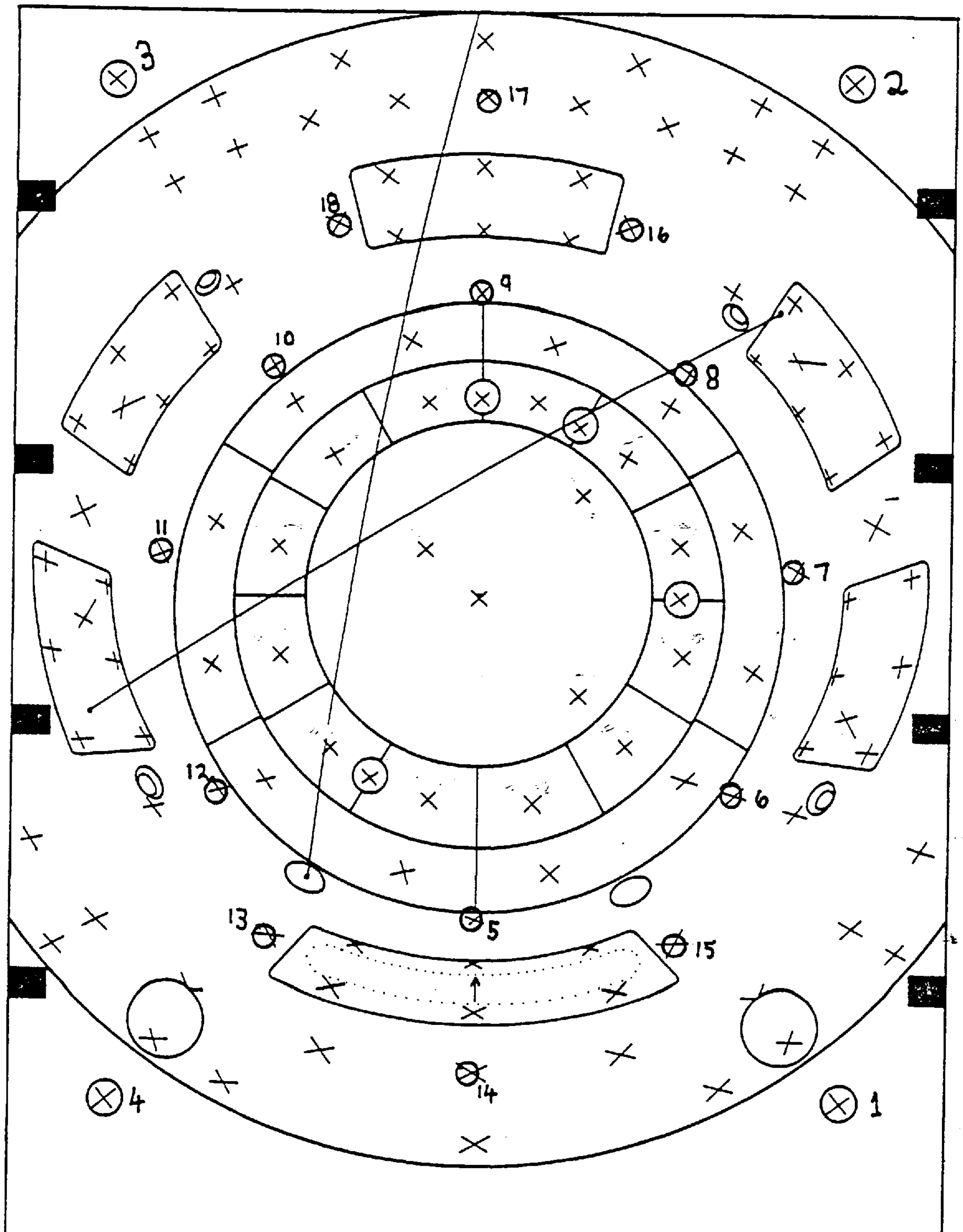

Fig 3.4

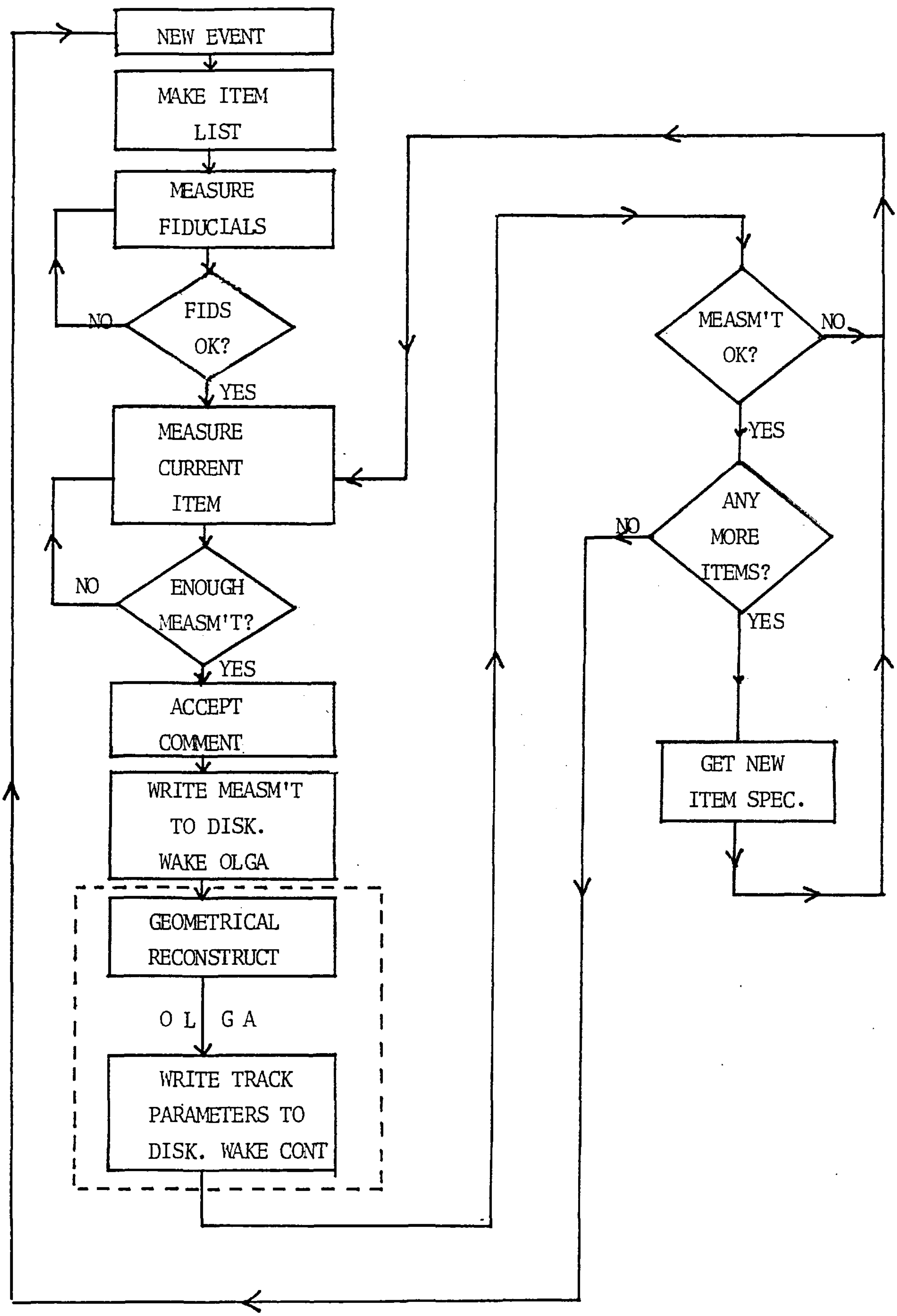
NEW EVENT
MAKE ITEM LIST
MEASURE FIDUCIALS
FIDS OK?
NO
YES
MEASURE CURRENT ITEM
ENOUGH MEASM'T?
NO
YES
ACCEPT COMMENT
WRITE MEASM'T TO DISK. WAKE OLGA
GEOMETRICAL RECONSTRUCT
O L G A
WRITE TRACK PARAMETERS TO DISK. WAKE CONT
MEASM'T OK?
NO
YES
ANY MORE ITEMS?
NO
YES
GET NEW ITEM SPEC.

Fig 3.5

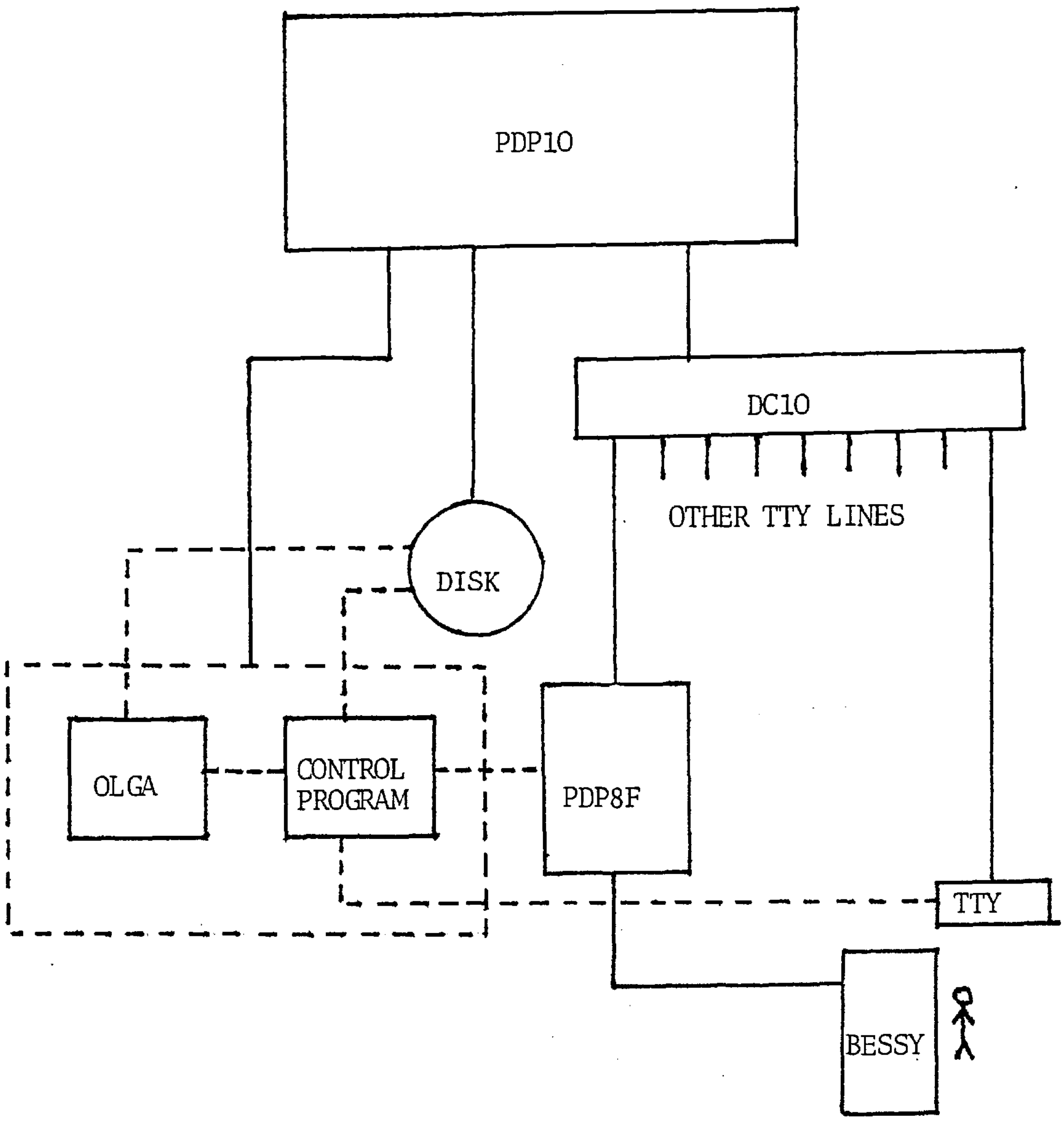
PDP10
DC10
OTHER TTY LINES
DISK
OLGA
CONTROL PROGRAM
PDP8F
TTY
BESSY

Fig 3.6

CHAPTER 4

Introduction

This chapter describes the stages after the events have been measured. Part 1 covers the offline geometry, and its principles; next follows a discussion on the reconstruction of electron tracks and the problems involved, then a brief account of the kinematic fitting of gammas from the measured electron tracks. Part 4.3 describes the precision of the fitted variables, showing plots of momentum resolution and track residuals. The post geometry processing is next described; gamma selection criteria and bremsstrahlung cuts imposed. Gamma-gamma effective mass plots are produced and attempts to clean up the π^0 signal described. The background to the gamma-gamma mass plots are then calculated being followed, lastly, by an outline of the massive combinatorial problems behind the kinematic fitting of gamma pairs to form π^0's and why a different approach is necessary.

4.1 Event Reconstruction

The stage following the event measuring was offline reconstruction. This was done using HYDRA geometry [(4.1)] developed at CERN. The task of this is to use the film measurements to reconstruct the vertices and tracks in three dimensions so as to determine their position in space and so calculate the particle momenta.

4.1.1 Geometrical Reconstruction of Tracks and Vertices

What follows is a brief discussion of the principles behind HYDRA geometry. The main tasks for geometry may be split into "point fitting" and "track fitting". The former is to reconstruct a definite point in space, (e.g. a primary vertex) where the same point has been measured on all views.

Track fitting is more difficult as several points are placed at roughly equal intervals along each track on each view, but in general the same points on the track are not measured on each view. Only the primary vertex (i.e. the start point) and, sometimes, the end point of each track are corresponding points on every view. Once a track has been reconstructed in space (a helix fit), mass hypotheses are attempted.

4.1.2 Point Fit

In attempting a "point fit" HYDRA tries to identify vertices on different views which are images of the same point in space. The resulting match must be such that no image yields several points. Given measurements of the images of a space point on two or more views, the position of the point $(X_1X_2X_3)$ and associated error matrix $\langle X_iX_j \rangle$ may be estimated. This is done in two stages:

i) Determination of approximate values of $X_1X_2X_3$

ii) A least squares fit to obtain best estimates of $X_1X_2X_3$ and error matrix

When measurements are labelled (as in the case of this experiment) these may be computed by choosing that point in space such that the sum of the squares of distances from the point to the light rays through the chamber (for each view, a light ray through the chamber between the camera and the measured point on that view is constructed) is a minimum.

Assuming isotropic measurement errors, this least squares fit is done by minimising with respect to $X_1X_2X_3$ the sum of squares of deviations, in the film reference plane, between measurements and projected points.

4.1.3 Track Fitting

Given a set of points measured along the same track on different views, track fitting combines these images into the same track through space. The basic steps are as follows

i) For each view a crude circle fit is done to the points on each track.

ii) Space to film transformations derive candidate "multiples" (light ray intersections on 2 or more views) near the vertex as well as a first estimate of track parameters.

iii) This approximation is used to construct "near corresponding points" along the track. These are points, measured on different views which are sufficiently close together in space to better define the track itself. These points are used to improve track parameters and, if necessary, more near corresponding points may be constructed further along the track. This process can be repeated for successive arc lengths up to the end of the track.

iv) Ambiguities are diagnosed and resolved from near corresponding point computation.

4.1.4 Final Track Fit

Lastly, mass hypotheses are used to improve the fits. This takes into account differing energy losses for different particles, multiple scattering etc. The fitting of electrons is described elsewhere in this chapter. However in principle mass dependent fits are made by following the track through the magnetic field and looking for deviations from uniform momentum. For each track, several particle mass hypotheses (e, μ, π, K or p) can be attempted, using a range-momentum relation, to see which particle trajectory best fits that track. Multiple scattering is taken into account by splitting the track into a number of segments and fitting each segment separately as well as finding two scattering parameters. Errors can be accumulated over all segments and a better fit achieved.

The number of segments is such that the maximum residual is of the order of magnitude of the measurement error.

For each track then several mass dependent fits maybe obtained, which at over 2 GeV/c momentum are virtually indistinguishable. It becomes necessary to limit the hypotheses: this may be done before or after geometrical reconstruction. To attempt all mass hypotheses would lead to an unecessarily large increase in both computing time and size of the program, especially when one already knows the masses of the particle tracks one is trying to fit.

This was the case with this experiment where the beam particles were known to be protons and the tracks from gamma vertices known to be electrons. The author thus modified the input processer of HYDRA geometry so as to limit the mass dependent hypotheses attempted i.e. only proton fits for beam tracks, only electron fitting for gammas.

This nearly halved the computing time for each event and reduced the size of the program by 20%. Also the post-geometry processing was aided as the need to process unnecessary (and useless) information was avoided.

4.1.5 Convex Fitting

In this experiment the only tracks to be fitted are the incoming beam track and the electron-positron pair from each gamma vertex, the point fitting being used to reconstruct all vertices. HYDRA however employs a "convex fit" to improve the vertex fitting. The track fits from each vertex are used to better define the vertex fit by using their point of intersection. For gammas two tracks are sufficient to do this. For the primary vertices where only the beam track has been measured, this is not possible (except in ensuring that the beam track does pass through the primary vertex). If the hadrons from the vertex had been measured however, then the primary vertex position would be determined more accurately.

As the primary vertex needed to be known, however accurately, it was necessary to prevent convex fits for the primary vertices with high χ^2 and to impose a χ^2 cut on vertices later ($\chi^2 > 20$ were rejected). This meant that gammas could be fitted back to the primary vertex, whereas if HYDRA had expected a convex fit on the primary, then these gammas would not have been able to be fitted.

4.2 Reconstruction of Electron Tracks

The reconstruction of gammas and ultimately π^o's depends on the measurement of the energy and direction of the electron-positron pair from the converted gammas. In principle this can be done in a heavy liquid bubble chamber in the same way as for any other particle namely a trajectory in the chamber is projected on at least two stereo views and varied to minimise the deviations of measurements from these projections. Important in determining the trajectory, apart from the curvature due to the momentum in the magnetic field, are the energy loss and small angle scattering from electromagnetic collision with the nuclei and electrons in the liquid. The most notable attempt to take into account these processes, is the break point method [4.2].

Elastic coulomb scattering is a small angle effect, decreasing inversely with particle momentum but Bremsstrahlung has the possibility of causing a large loss in energy at a single collision. An electron loses energy, on average, according to:

$$\frac{dE}{dX} = -\frac{E}{X_o} \tag{4.1}$$

where X_o is the radiation length of the liquid (42cm) in this case.

The probability of retaining an amount of energy $e^{-y}E$ after a short distance dl is:

$$P(y)dy = \frac{e^{-y}\, y^{bdl-1}}{\Gamma(bdl)}\, dy \tag{4.2}$$

$$b = (X_o \log 2)^{-1} \qquad \text{(see ref. 4.3)}$$

This produces gross straggling effects but small angular deflection.

Several methods are available to fit electron tracks. Behr and Mittner [4.4] fit a helix and then correct for the most likely energy loss from equation (4.2). An alternative is to fit a logarithmic spiral helix following the predicted average energy loss of equation (4.1).

The radius of curvature is:

$$\rho \; \alpha \; P \; = \; P_0 \; e^{-s/X_0}$$

It is advisable to limit the length of the track in these cases.

In practice, (i.e. in HYDRA), the real trajectory is approximated by splitting the track into a series of short segments. Within each segment, the trajectory is assumed to follow the equation with only small radiations included. Large radiation losses and coulomb scattering are accumulated at the end of each segment. In this way an approximation to the true trajectory of the electron is found parameterised by the initial parameters and scattering parameters. It is the initial parameters which are required for kinematic fitting.

4.2.1 Kinematic Fitting of Gammas

For gamma vertices the information available after geometrical reconstruction is as follows:

i) position of the gamma vertex

ii) parameters ($1/p$, λ, ϕ + errors) of the electron tracks.

At the vertex, only one track is missing and unmeasured viz. the gamma itself. HYDRA kinematics attempts to use the available information to reconstruct this missing track such that the parameters of the gamma are known. This is done by applying constraints to the vertex. These include momentum and energy conservation:

$$\vec{p}_{e_1} + \vec{p}_{e_2} + \vec{p}_\gamma = 0 \; ; \; E_{e_1} + E_{e_2} - E_\gamma = 0 \qquad (4.3)$$

where e_1 and e_2 refer to the two electrons produced by γ.

Further constraints can be applied to a gamma vertex e.g. insist that there is a zero degree opening angle between the electrons and that the gamma comes from the primary vertex. The zero degree opening angle is only approximate at low photon momentum[4.5]:

$$\theta \approx m_e c^2/E_\gamma$$

For gamma energies greater than 50 MeV θ is approximately zero.

From measured quantities then, in general, equation (4.3) would not be satisfied, instead:

$$\sum_i P_{ik}(x) = F_k(x)$$

HYDRA kinematics fits the measured and unmeasured quantities such that the χ^2 for the fit is a minimum. The constraints will also improve the electron parameters. A 4C fit is obtained for the gamma when the additional constraint of coming from the primary vertex has been imposed. If this is not satisfied, a reconstructed gamma has only a two constraint (2C) fit.

4.3 Fitting Precision

4.3.1 Momentum Resolution

Having processed events through geometry it is possible to see how well tracks have been measured, in particular to compare the beam track and electron reconstructions. There are several ways of looking at this information. First of all a plot of $\Delta p/p$ for tracks will show how good the momentum resolution is. Plots of $\Delta p/p$ for beam, electrons and reconstructed gammas are shown in Fig. 4.1a, b and c respectively.

For the beam tracks there is a large spread, trailing off to high $\Delta p/p$ but peaked fairly low (at about $\Delta p/p$ of 0.07). The mean value is 18 ± 11%. It should be remembered, however, that the beam momentum is 70 GeV and consequently the tracks are quite straight and so need to be measured over quite a length to obtain good momentum resolution.

The electron tracks have, on average, a poorer momentum resolution $\langle \Delta p/p \rangle = 20.3 \pm 7.3\%$. However the distribution, peaking at about 17% falls much more rapidly that that of the beam. The lower momentum ($\langle p \rangle \simeq 700$ MeV) means that the measured sagitta is larger than that of the beam for any given track length. Moreover for electrons multiple scattering, straggling effects are much more important and also bremsstrahlung limits the length over which the tracks can be measured.

For the gammas the momentum resolution is marginally better than the electrons, as kinematic constraints better define gamma momenta:

$$\langle \Delta p/p \rangle = 18 \pm 7\%$$

The general shape of the distribution is much the same as that of the electrons.

A more useful plot of momentum resolution is one of $\Delta(1/p)$ against track length. As the momentum is directly proportional to the radius of curvature of the track which is (for large R) inversely proportional to the sagitta s, a measured quantity. So $p \propto 1/s$. Consequently $\Delta(1/p)$ is a more useful quantity than Δp as it directly relates to the sagitta error. The longer the measured track, the larger the sagitta for a given momentum and a better determined value of the sagitta. Consequently the longer track length leads to a smaller $\Delta(1/p)$. Plots of $\Delta(1/p)$ versus track length are shown in Figs. 4.2a and b for beam tracks and electrons respectively. The shapes are roughly hyperbolic as expected.

4.3.2 Track Residuals

A useful check on the accuracy and calibration of the measuring machine are the residual distributions; the mean mesidual being defined as the mean spread of measured points along any track about the fitted track on the film. Beam tracks should have a lower mean residual than electron tracks as the former are not so affected by multiple scattering, straggling or bremsstrahlung. As can be seen from Figs. 4.3a and b the spread in the beam residuals is much smaller than the electrons.

$$\langle r_{beam} \rangle = 8.2 \pm 2.4\ \mu$$

$$\langle r_{electrons} \rangle = 8.7 \pm 4.4\ \mu$$

A machine like BESSY 2 would be expected to produce residuals of order 10μ on average.

Whenever the track residuals at the online measuring stage were found to be consistently high over a period of time (a few days), the BESSY machine was recalibrated. This needed doing approximately every six months, so little data was lost because of an out of date calibration.

4.3.3 Energy Distribution of Electrons

The cross-section for the creation of an electron from a gamma in the range E_- to $E_- + dE_-$ is given by [4.5,4.6]:

$$\sigma_{E_-}\, dE_- = \bar{\sigma}.\, \frac{p_+ p_-}{E_\gamma^{\,3}}\, dE_-\, f(E_- E_+) \tag{4.4}$$

The exact form of this equation is given by Heitler [2.5].

For very high gamma energies and neglecting screening, (4.4) reduces to

$$\sigma_{E_-}\, dE_- = 4\sigma \left[\frac{E_-^{\,2} + E_+^{\,2} + \frac{2}{3}E_+E_-}{E_\gamma^{\,3}}\right]\left[\log \frac{2E_+E_-}{mc^2 E_\gamma} - \frac{1}{2}\right]$$

$$\rightarrow \frac{4\sigma}{E_\gamma}\, f(v) \tag{4.5}$$

where $v = E_-/E_\gamma$

and $$f(v) = \left[v^2 + (1-v)^2 + \tfrac{2}{3}v(1-v)\right] \times \left[\log \frac{2E_\gamma}{mc^2}\, v(1-v) - \frac{1}{2}\right] \tag{4.6}$$

A plot of $\xi(v)$ versus v using equation (4.6) is shown in Fig. 4.4a superimposed on the experimental data. The solid line is a fit using E_γ as a free parameter; the broken line with E_γ fixed at the mean gamma momentum. The shape is in generally good qualitative agreement with theory but the discrepancy between the two curves can be explained by a loss of very asymmetric gammas as these are both more difficult to measure and to fit than symmetric gammas. Also the 20% errors on each of P_e and P_γ would tend to smear the experimental points out so that the sharp edges are poorly defined. Moreover the fit is particularly sensitive to the region of asymmetry ($v < 0.2$ or $v > 0.8$) and a good fit to the data would require these regions to be much better defined than they are.

Using only those points between v of 0.3 and 0.7 (4.4b) gives a much closer fit to that expected.

4.3.4 Vertex Distributions

The distribution of the primary vertex x, y and z coordinates in the BEBC reference frame are shown, respectively, in Figs. 4.5a, b and c. The x coordinate distribution shows a decrease over the x range -130cm to about 0cm. The scanning cut has let through some events with an x position less than -130cm but loses some events in the region 0 to +30cm. This loss is not serious and does not adversely affect the fiducial cut. The y coordinate distribution is slightly off centre, as a result of the angular separation between the beam axis and the BEBC reference axis. The effect of the BEBC magnetic field results in a broad y distribution as compared with the spread of the vertices over the z direction. From 4.5c one can see that the divergence of the beam along the z axis is small, in fact less than 1 mrad.

The mean values of x, y and z are shown in Table 4.1.

4.3.5 Beam Track Length

The track length for beam tracks is shown in Fig. 4.6 together with a least squares exponential fit over the region 50 to 150cm. The mean interaction length is 126 ± 24cm, compatible with the interaction length predicted for a 40mb proton-nucleon cross-section by ref. 2.7.

4.4 Post Geometry Processing

The event processing after HYDRA geometry took the following course:

4.4.1 Gamma Selection

The geometry output was read and only relevant information selected, namely the incoming beam parameters, and the parameters for all the reconstructed gammas. Much of the information contained in the HYDRA geometry output was irrelevant for the subsequent analysis. This consisted of the measured electron parameters, vertex coordinates etc. The information that is useful is that pertaining to the beam (so as to define an axis in the chamber) and that for the reconstructed gammas. Once a gamma has been reconstructed, the electron data is no longer essential and so may be rejected.

Program HYDRD (and successors) reads the geometry output tapes, selects the beam information and the gammas with 4C fits to the vertex. This information consists of the momentum, dip and phi of these tracks with their associated errors plus additional information to identify the gammas and their distance from the primary vertex.

It was found that many reconstructed gammas with only two constraints (2C fits) did in fact appear to associate with the vertex on a visual inspection. It was decided to make cuts to accept these gammas. The impact parameter to the vertex was calculated, together with the error (for 4C fits the impact parameter, by definition, is zero), and if either the impact parameter was smaller than twice its error or the angle between the reconstructed line of flight of the gamma and the line between gamma and the primary vertex (θ in Fig. 4.7) was less than a specific value (3°), then that gamma was accepted for the subsequent analysis.

The proportion of gammas accepted in this way was 30.6%.

The proportion of gammas failing geometrical reconstruction was calculated at this stage: 14 ± 1.2%. This is a measure of true gamma vertex reconstruction.

Also at this stage one can look at such useful information as $\Delta p/p$ for gammas, beam and electron tracks.

Gammas whose $\Delta p/p$ was too large (> 0.5) were rejected at this stage as well as events whose primary vertex was badly measured ($\chi^2 > 20$). Events where the beam momentum was badly measured were also thrown out, though the cut on this was not too severe ($\Delta p/p < 1$). As the beam track is primarily used to define the direction with which the gamma P_T is measured, so long as the dip and phi are well measured, and this is generally the case, then that is enough. However if the momentum is badly determined then this introduces large errors in the calculation of such parameters as Feynman x. This is not though of primary importance.

The information thus selected was written to a card image disk file. It was thus possible to inspect by hand the data at this stage, before it was processed further and to edit out any ambiguities or problems (such as cases where one gamma has been measured twice). Table 4.2 summarises this stage.

4.4.2 Production of the DST

The next stage in the processing chain consist of combining the gammas in pairs and calculating their effective masses, ordering the gammas in descending order of P_T and calculating such variables as Feynman x for the gammas. Also imposed were the bremsstrahlung cut (see Section 4.5) and the π^o/η χ^2 cut (see Section 5.1). Those gammas which are bremsstrahlung were merely tagged as such at this stage before being removed in the next. Neither was any decision taken on π^o's or η's. Those effective mass combinations satisfying the π^o or η cuts were tagged as such in order to be sorted out later. HYDRA banks are lifted to contain all this information and output in FQX format. This data represents the final DST on which the physics analysis proceeds. Table 4.3 shows the HYDRA structure of the DST.

Figure 4.8 shows the raw gamma-gamma effective mass plot for all combinations of gammas from every event. No cuts have been imposed. As can be seen no evidence of the π^o is to be found on this plot except for a shoulder at around the π^o mass. The reason for this is due to bremsstrahlung; the very small opening angle between a bremsstrahlung gamma and its parent together with its much lower momentum results in a very small effective mass, generally less than 100 MeV. In order to clean up the plot to reveal a π^o peak and, hopefully, an η it was necessary to introduce a cut designed to remove bremsstrahlung gammas.

4.5 Bremsstrahlung

Due to the short radiation length in Ne/H_2 bremsstrahlung is a major problem. On average an electron from a converted gamma will radiate half of its energy as photons in a length 42cm in the chamber. This is seen as a sudden kink or change of curvature of the electron track. This effect tends to make measuring more difficult. Moreover the bremsstrahlung photons are likely to convert in the chamber. Frequently these bremsstrahlung photons are obviously seen as such: they point to a specific electron track and not to the primary vertex. More often, however, they are ambiguous: they may come from the primary vertex. It was decided to include in the measuring all gammas that could possibly be associated with the primary vertex and to sort out the bremsstrahlung gammas later.

4.5.1 Cut to Remove Bremsstrahlung

In order to separate out bremsstrahlung, use was made of the minimum opening angle condition for the γ's. As the photon is massless there is a minimum opening angle between the gammas from π^o decay in any frame. This angle is when both decay γ's shoot out perpendicular to the line of flight of the π^o (or η) parent (see Fig. 4.9). In this case the transverse momentum component (wrt the π^o direction) is $M_{\pi^o}/2$ and the longitudinal component is $p_{\pi^o}/2$, hence the opening angle between the two gammas is:

$$\theta_{\gamma\gamma} = \theta_1 + \theta_2 = 2\tan^{-1}\frac{M_\pi}{p_\pi}$$

where p_π is the momentum of the parent π^o in the frame at which $\theta_{\gamma\gamma}$ is measured.

If $\Delta M_{\gamma\gamma}$ is the error on the effective mass $M_{\gamma\gamma}$ between any two gammas then the following conditions must be applied:

if:

$$\theta_{\gamma\gamma} \quad < \quad 2x\tan^{-1} \frac{M_p - 2x\Delta M_{\gamma\gamma}}{p_p}$$

and the momentum of the downstream gamma (within 1 SD) is less than that of the upstream gamma then the downstream gamma is taken to be a brem.

$$M_p = M_{\pi^o} \quad \text{if } M_{\gamma\gamma} < 0.2 \text{ GeV/c}$$

$$= M_{\gamma\gamma} \quad \text{if } M_{\gamma\gamma} > 0.2 \text{ GeV/c}$$

$$p_p = |\vec{p}_{\gamma_1} + \vec{p}_{\gamma_2}|$$

Any gamma satisfying these conditions was rejected together with all effective mass combinations formed with other gammas. The results of this cut are shown in Table 4.4.

This bremsstrahlung cut was imposed and the cleaned up gamma-gamma effective mass plot is shown in Fig. 4.10. Here a π^o peak is clearly visible, despite the considerable combinatorial background. Also there is a sharp drop at $M_{\gamma\gamma}$ below 100 MeV. This suggests that the bremsstrahlung cut is too severe and is rejecting perfectly good gammas. It now becomes necessary to see what the shape of the combinatorial background is, and how many "real" gammas are rejected because of the bremsstrahlung cut.

4.6 Calculation of the Background

In order to calculate the shape of the background in the gamma-gamma effective mass plot, that is the background due to combining uncorrelated gammas, those not from the same parent, the author decided to attempt combining gammas from different events. This was achieved as follows. All measured gamma parameters were written to a random access file on the IC PDP10. Gammas were then selected at random in pairs from this file, making sure that no two gammas from the same event were selected. Their effective mass was calculated and the bremsstrahlung cut imposed. This was done for a large number of gamma pairs such that the statistics were very high, and a fairly smooth curve resulted. The chances against using the same pair twice was about 4 million to 1. As the number of combinations in all was about two million (resulting, for a fifty bin histogram, in an error per bin of less than 1%) then it is unlikely that any pair was selected twice for this curve.

Above 250 MeV an exponential was fitted in order to smooth out the background curve.

This was repeated without imposing the bremsstrahlung cut in order to find out how many gammas and mass fits are rejected because of this cut. The respective shapes of these two are shown in Fig. 4.11. As can be seen the bremsstrahlung cut throws out much "real" background (i.e. that not arising from bremsstrahlung but due to combinatorial background) below 100 MeV consequently losing some π^0's and gammas. Knowing this, corrections can be made.

4.7 Kinematic Fitting of π^o

Ideally it should be possible to combine the gammas measured on each frame by using HYDRA kinematics to form π^o and η. One takes the N gammas and forms combinations such that the χ^2 for forming a set of n π^o's ($n \leq N/2$) is a minimum. The π^o's are then the combinations such that the χ^2 for those combinations are less than some predetermined value (say $\chi^2 \leq 5$). One could also include the η into the kinematic fit and select η's in this way too.

Suppose though, that one has, for example, 6 gammas successfully measured and reconstructed on one event. These might form three reasonable π^o's with no gammas left, or two good π^o's with 2 γ's unfitted, or perhaps one excellent π^o but with 4 gammas unpaired. Which combination is correct? The probability is that each set of combinations is equally as good - or as bad - as any other. In a situation such as this, common in this experiment, a fitting program would have extreme difficulty selecting the best set of π^o's.

If a set of γ combinations is defined as any group of 2 γ combinations such that no gamma is combined with more than one other gamma within each set, with N gammas on any one frame the number of sets is found as follows. The first gamma forms (N-1) combinations with the others. This leaves N-2 gammas in any one set to combine. The next γ can thus form N-3 combinations with the rest and so on. Thus the number of sets is (4.7):

$$n = (N-1)(N-3)(N-5)\ldots.$$

$$= \frac{N!}{(N/2)!\ 2^{N/2}}$$

For $N < 5$ or 6 this number is manageable, yet for $N > 10$ the number of sets to be tested is extremely large. The computation involved would be vast.

Since the aim of the experiment was to find direct γ's, the author chose, in the first instance, to pair off the highest P_T gammas on each frame to form a π^o or η.

REFERENCES

4.1 HYDRA APPLICATIONS LIBRARY
HYDRA Systems Manual.

4.2 P. Laurikainen, W.G. Moorhead, W. Matt
Nucl. Inst. & Methods 98 349 (1972)

4.3 D.J. Crennel RHEL / Physics Note / 113

4.4 L. Behr, P. Mittner; Nucl. Inst. & Methods
20 446 (1963)

4.5 K.H. Spring "Photons and Electrons"
Methuen Monographs 1960

4.6 D.H. Perkins "Introduction to High Energy Physics"
Addison Wesley 1972

4.7 R. Beuselinck Private Communication.

TABLE CAPTIONS

	mean value cm	mean width cm
x	-79.8	36.3
y	+4.1	8.3
z	-1.33	3.54

TABLE 4.1 Primary vertex coordinate in BEBC reference frame

No. of events through geometry	1328	
No. left after cuts on χ^2 and beam momentum	1109	219 rejected
No. gammas measured	11616	10.4 / ev
No. gammas with 4C fit	4419	
No. gammas with 2C fit	5585	
No. gammas failing	1612	13.9 ± 1.2%
2C fits used	1946	30.6 ± 0.8%
Total no. γ's used	6365	5.8 / event

TABLE 4.2 Summary of the offline Geometry and Gamma selection

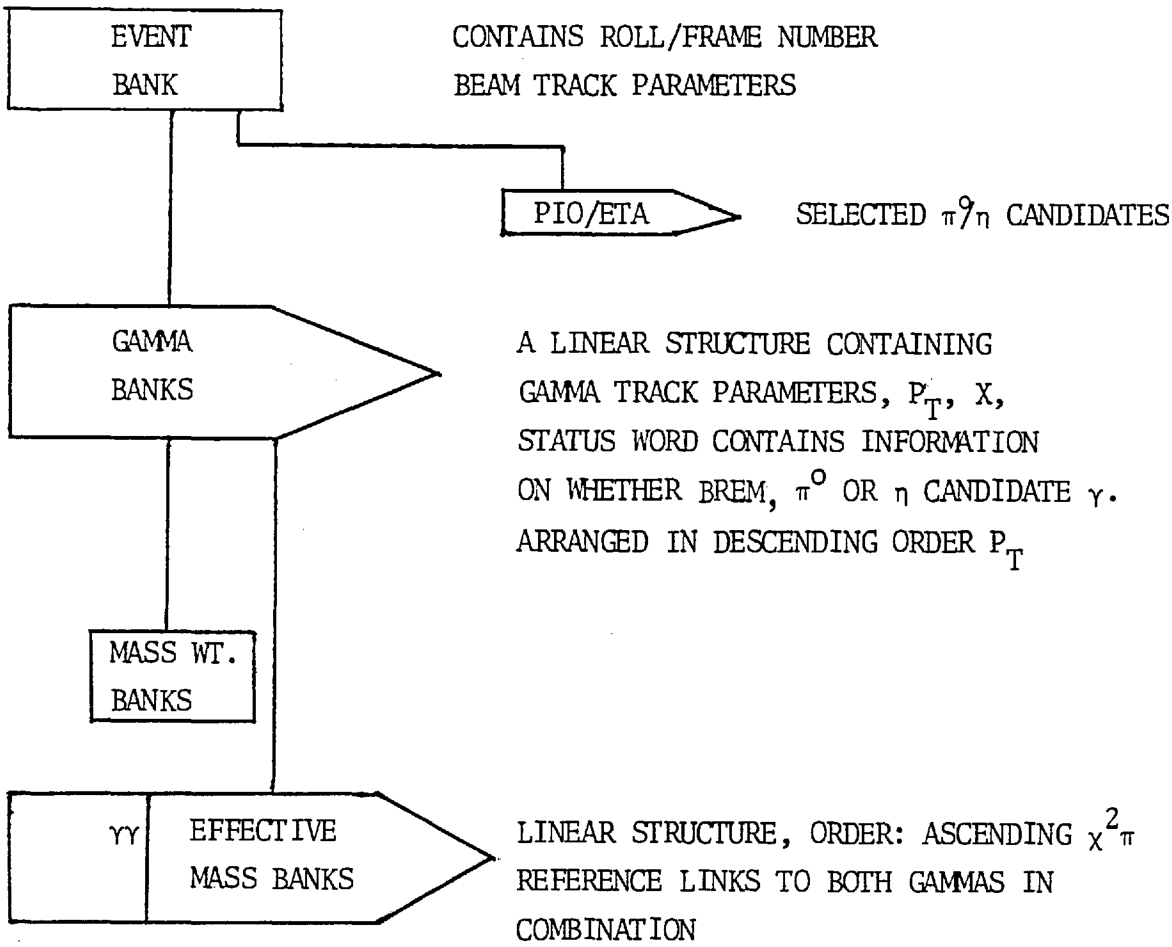

TABLE 4.3 HYDRA Bank Structure of DST

No. of gammas used	6292
Bremsstrahlung gammas removed	1460
Brems which formed π^0 with another γ	246
forming η	17
No. of gammas left	4832
No. of real gammas rejected by brem cut (estimated)	150

TABLE 4.4 Result of Bremsstrahlung Cut

FIGURE CAPTIONS

4.1 a) $\Delta p/p$ Beam Track

b) $\Delta p/p$ Electron Tracks

c) $\Delta p/p$ Gamma

4.2 a) $\Delta(1/p)$ v Track Length - Beam Track

b) $\Delta(1/p)$ v Track Length - Electron Tracks

4.3 a) Residuals - Beam Track

b) Residuals - Electron Tracks

4.4 a) f(v) versus V with least squares fit (solid line) superimposed. Dashed line is equation 4.6 with $E_\gamma = 2.3\text{GeV}$

b) f(v) versus V. Solid line is a least squares fit over range $0.3 < v < 0.7$

4.5 Vertex Distribution :

a) x

b) y

c) z

4.6 Beam Track Length with Exponential Fit.

cont...

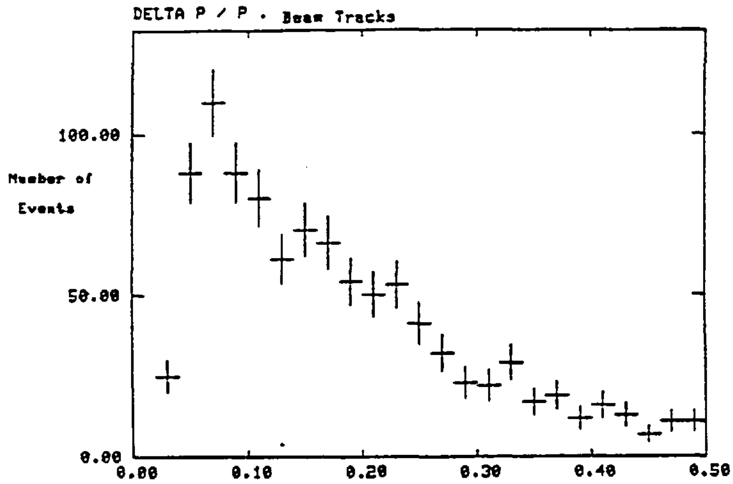

Fig. 4.1a

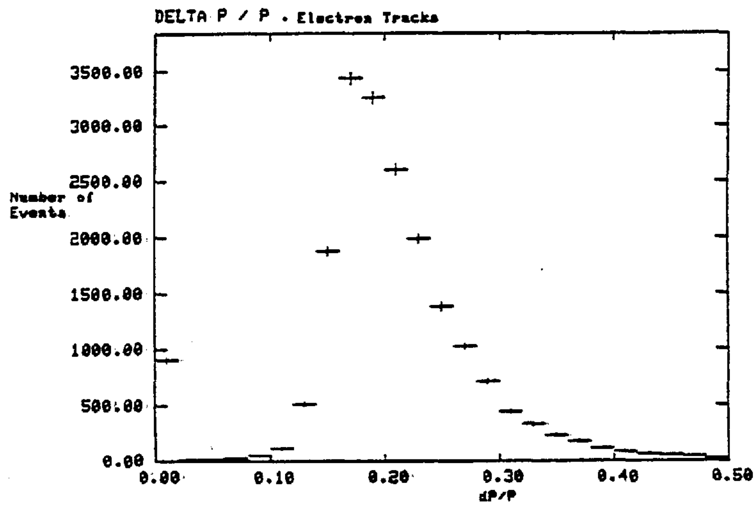

Fig 4.1b

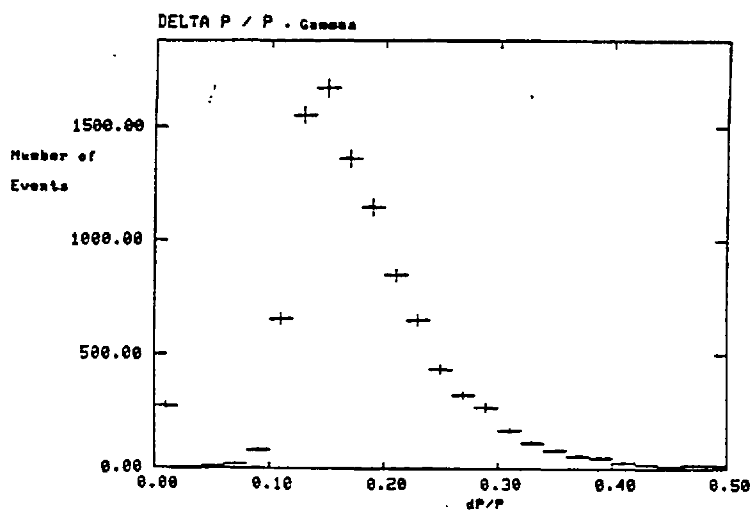

Fig 4.1c

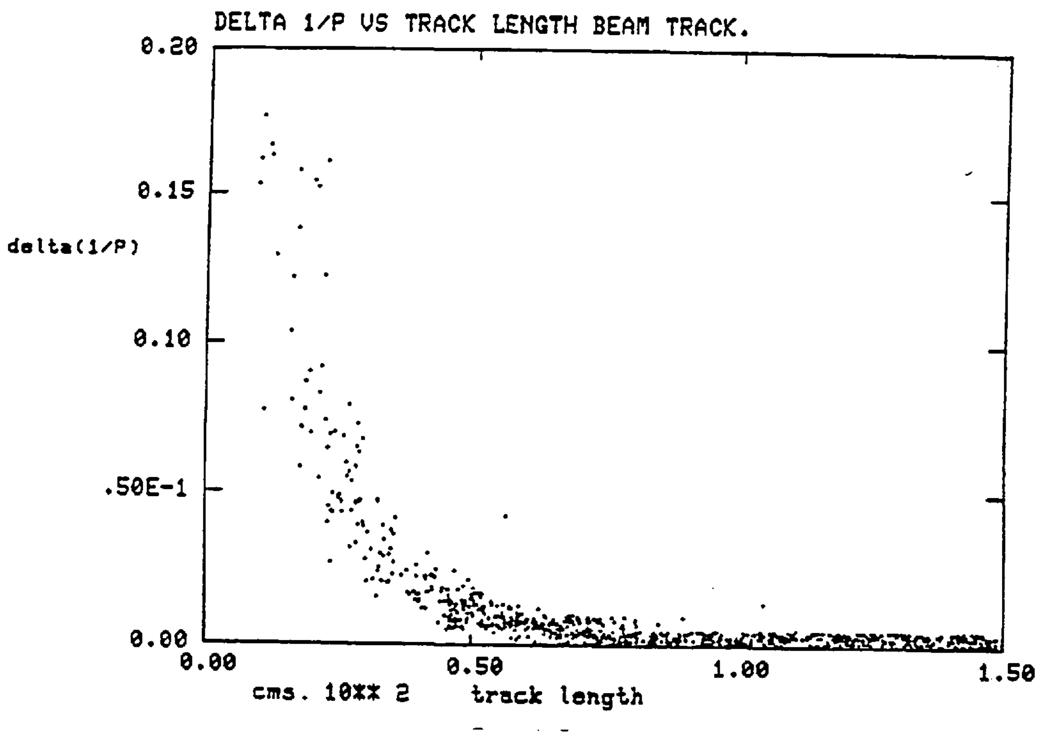

Fig 4.2a

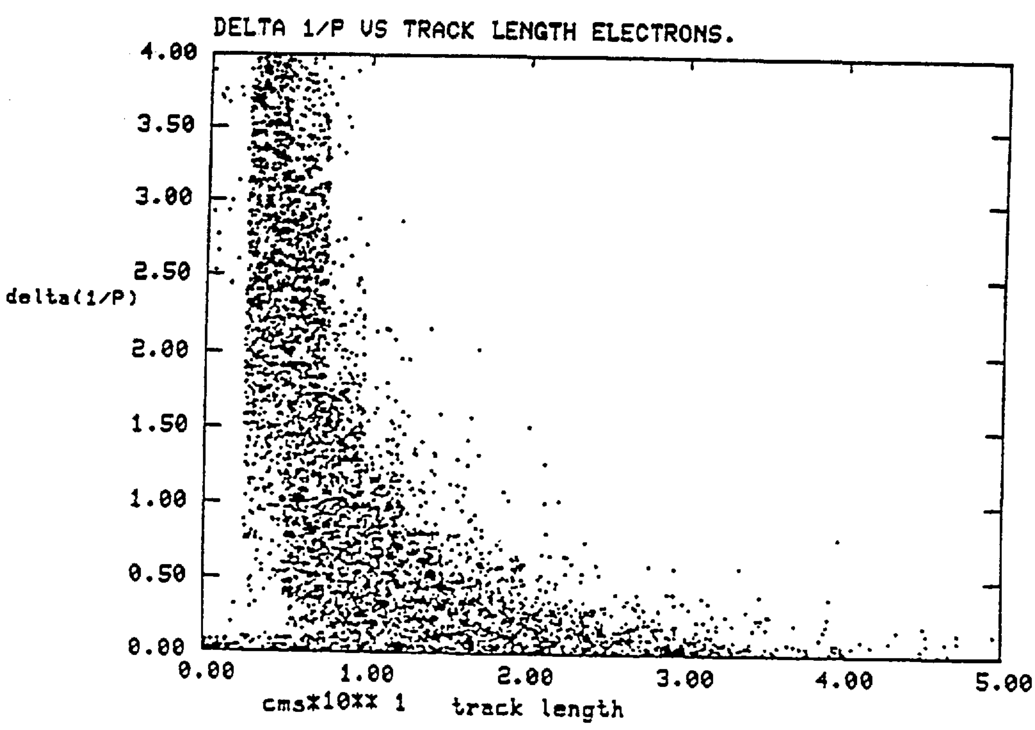

Fig 4.2b

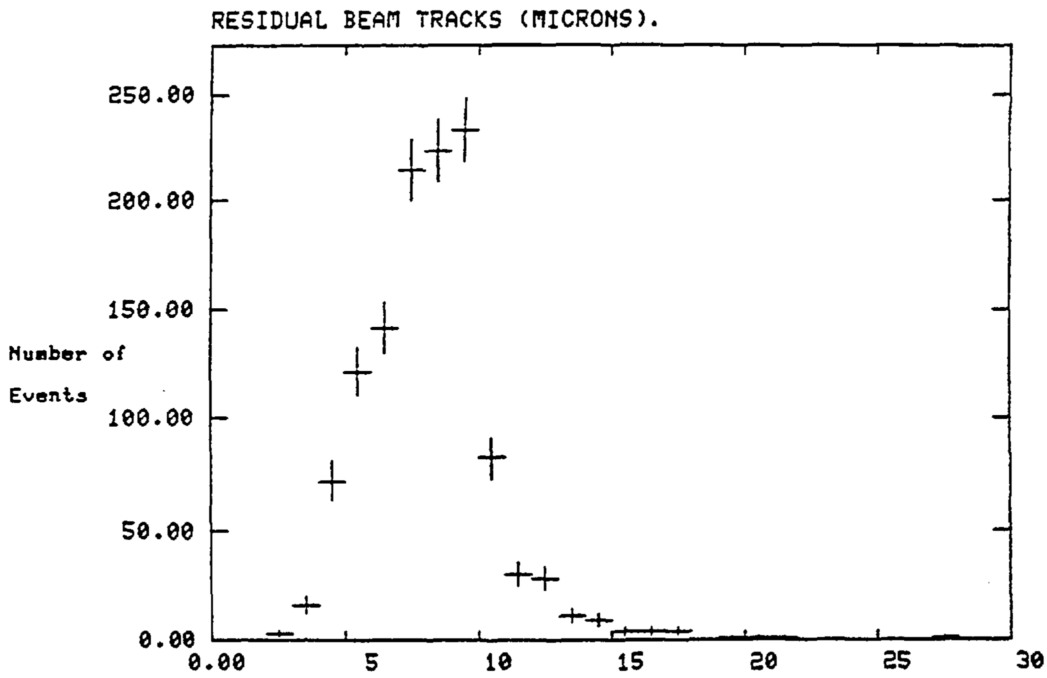

Fig 4.3a

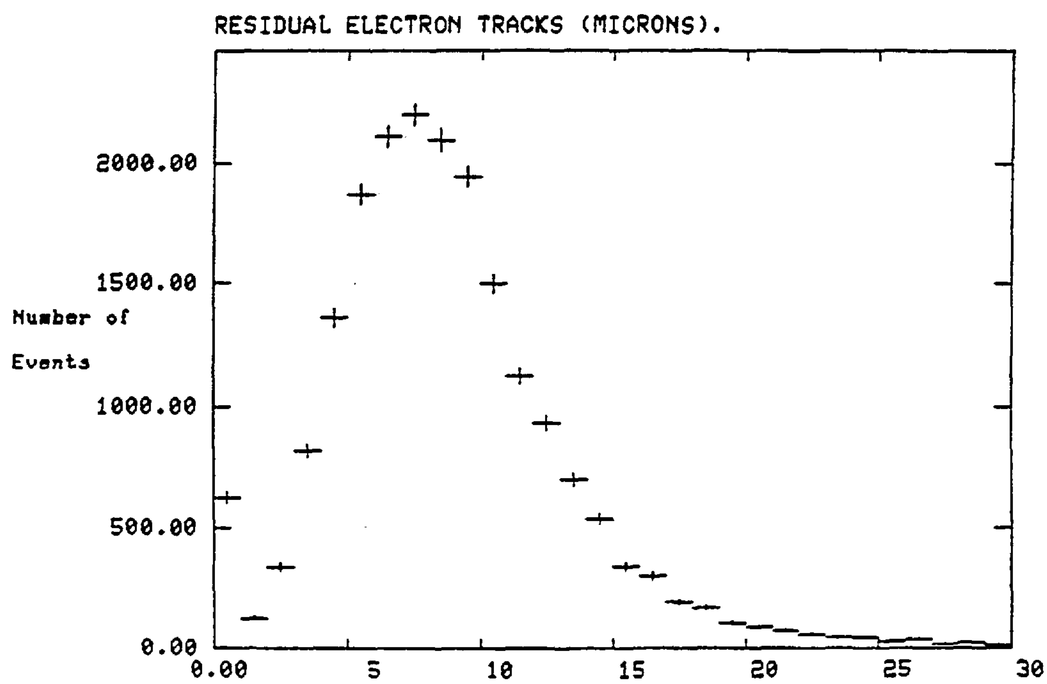

Fig 4.3b

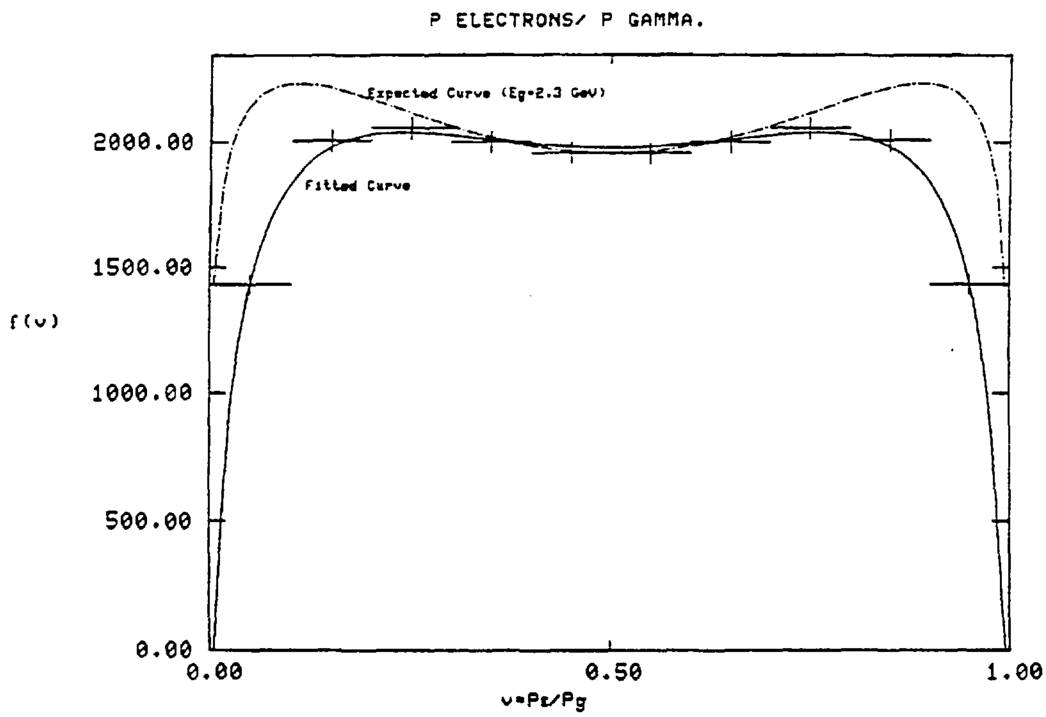

Fig 4.4a

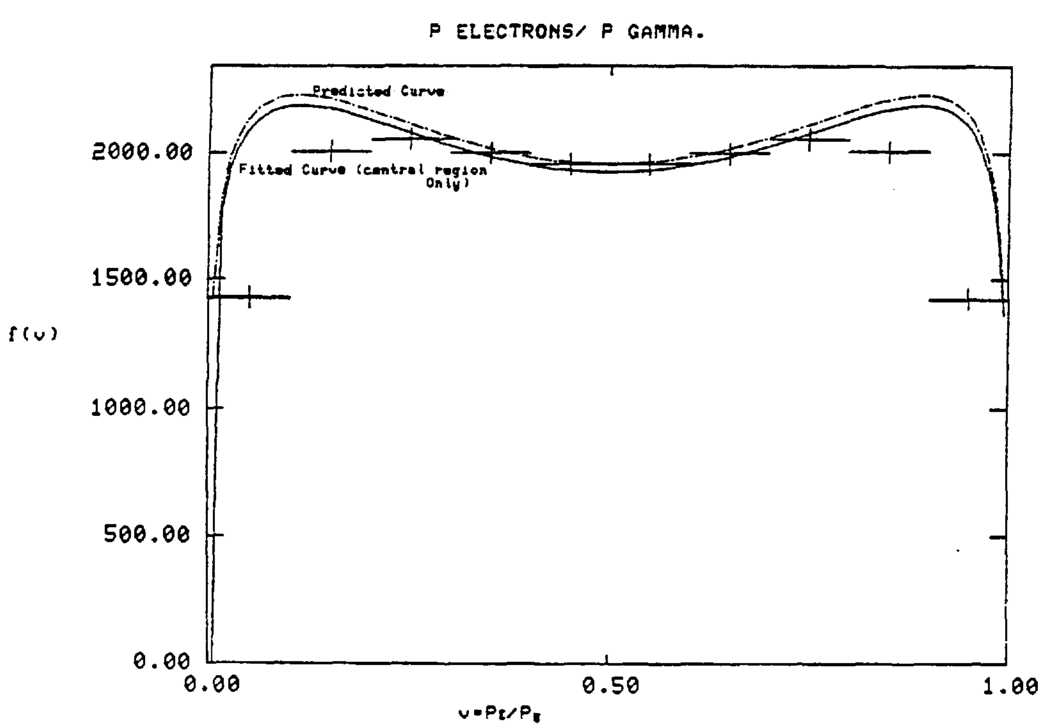

Fig 4.4b

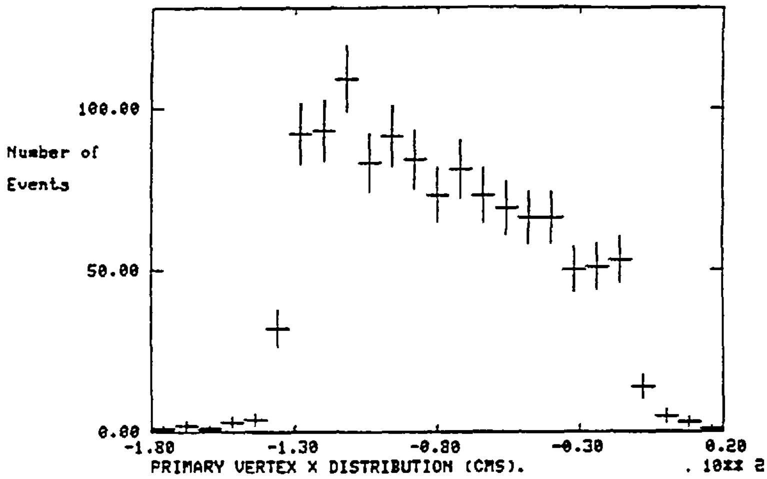

Fig 4.5a

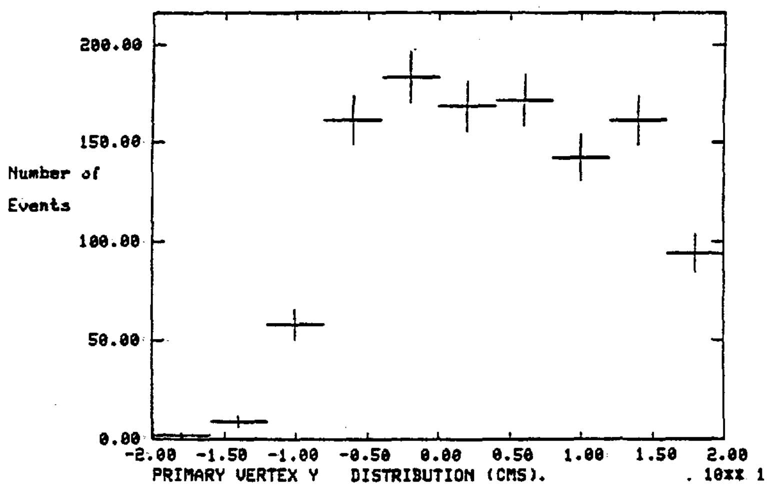

Fig 4.5b

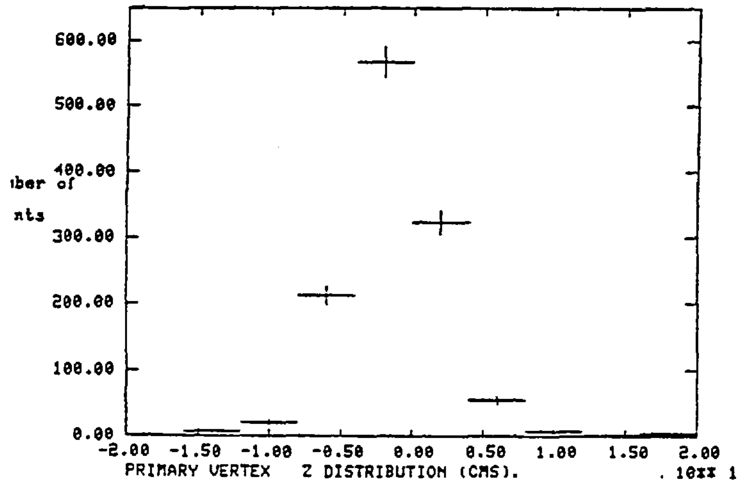

Fig 4.5c

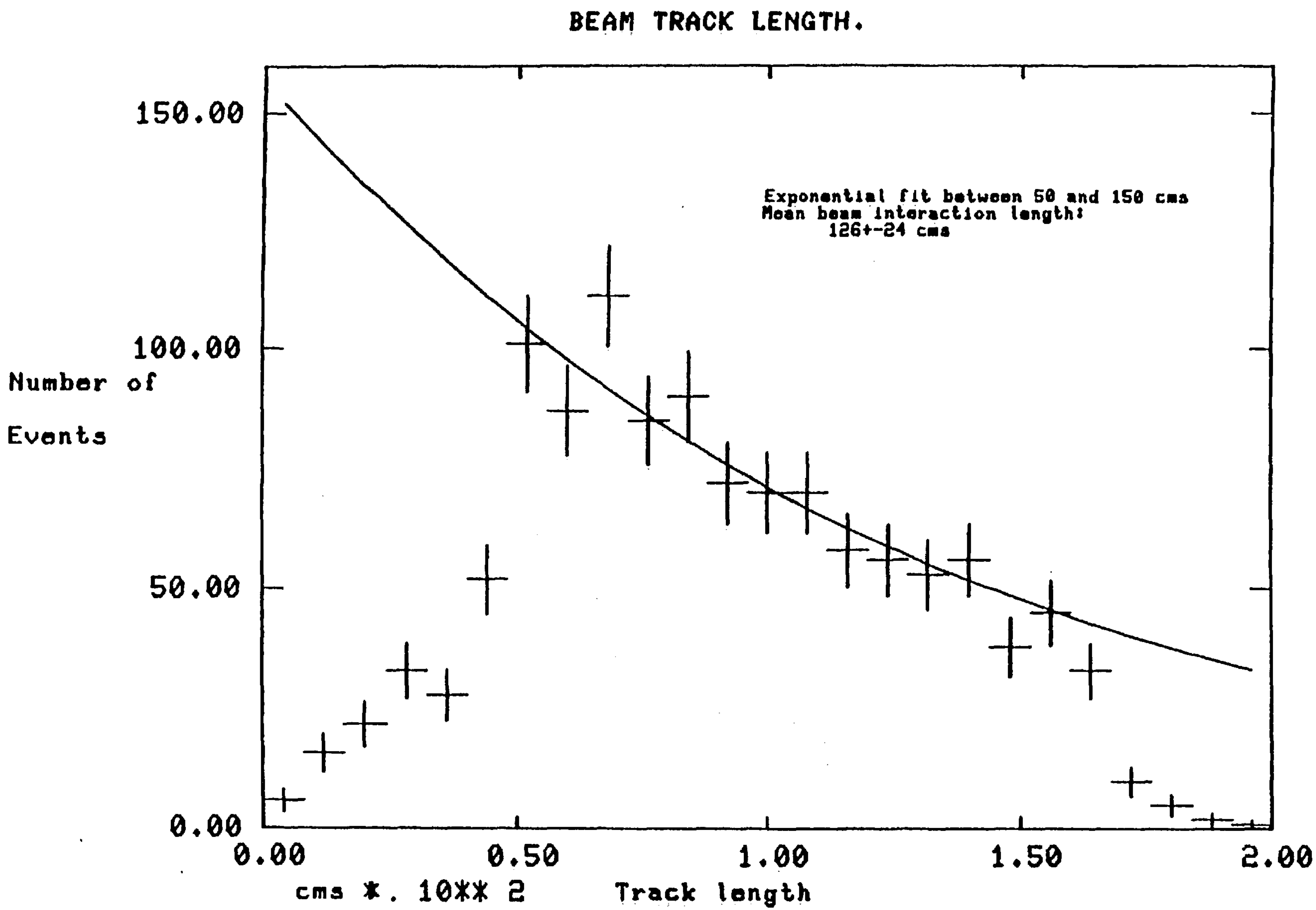

BEAM TRACK LENGTH.
Exponential fit between 50 and 150 cms
Mean beam interaction length:
126+-24 cms
150.00
100.00
50.00
0.00
Number of
Events
0.00
0.50
1.00
1.50
2.00
cms *. 10** 2
Track length

Fig 4.6

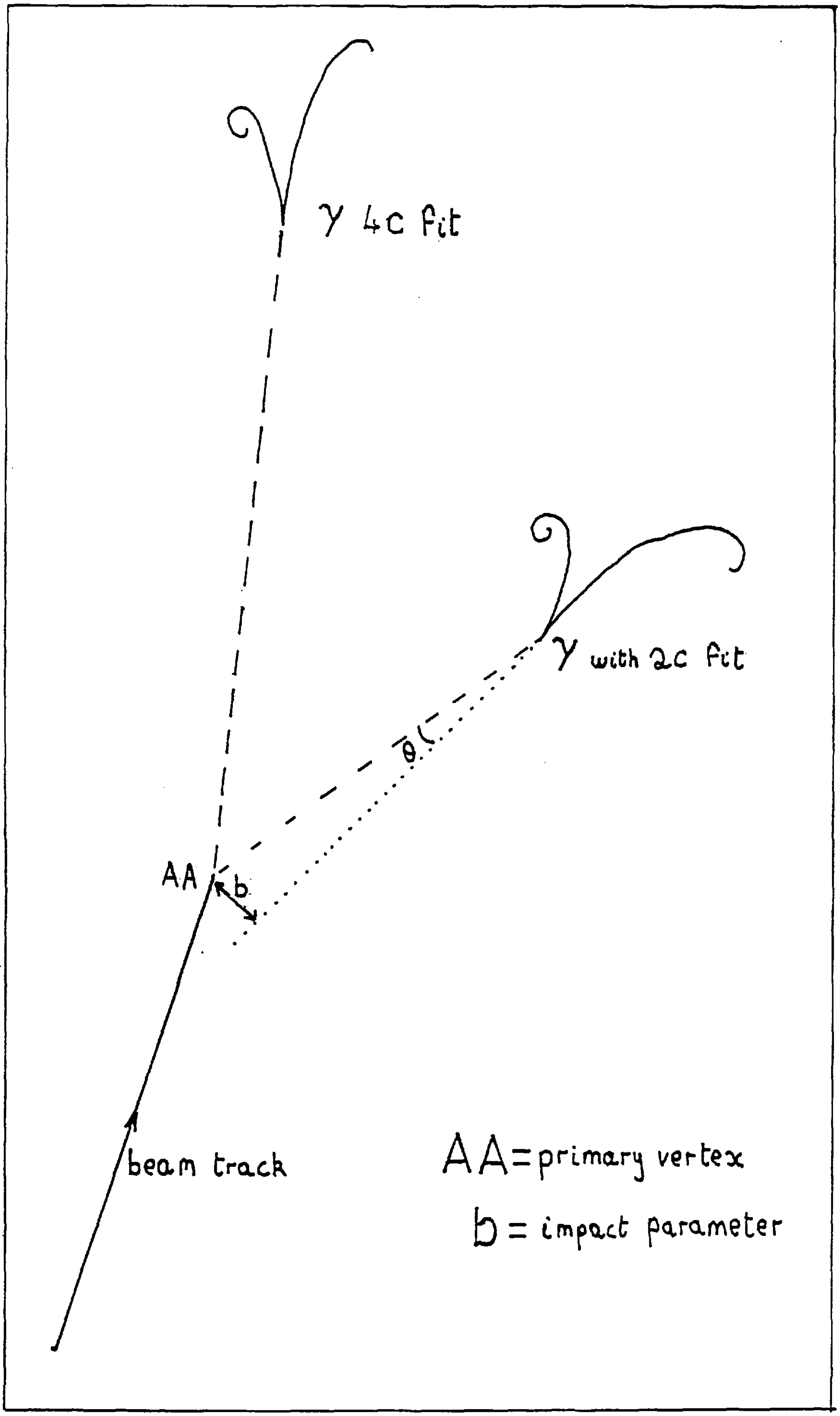
γ 4c fit
γ with 2c fit
θ
AA
b
beam track
AA = primary vertex
b = impact parameter

Fig 4.7

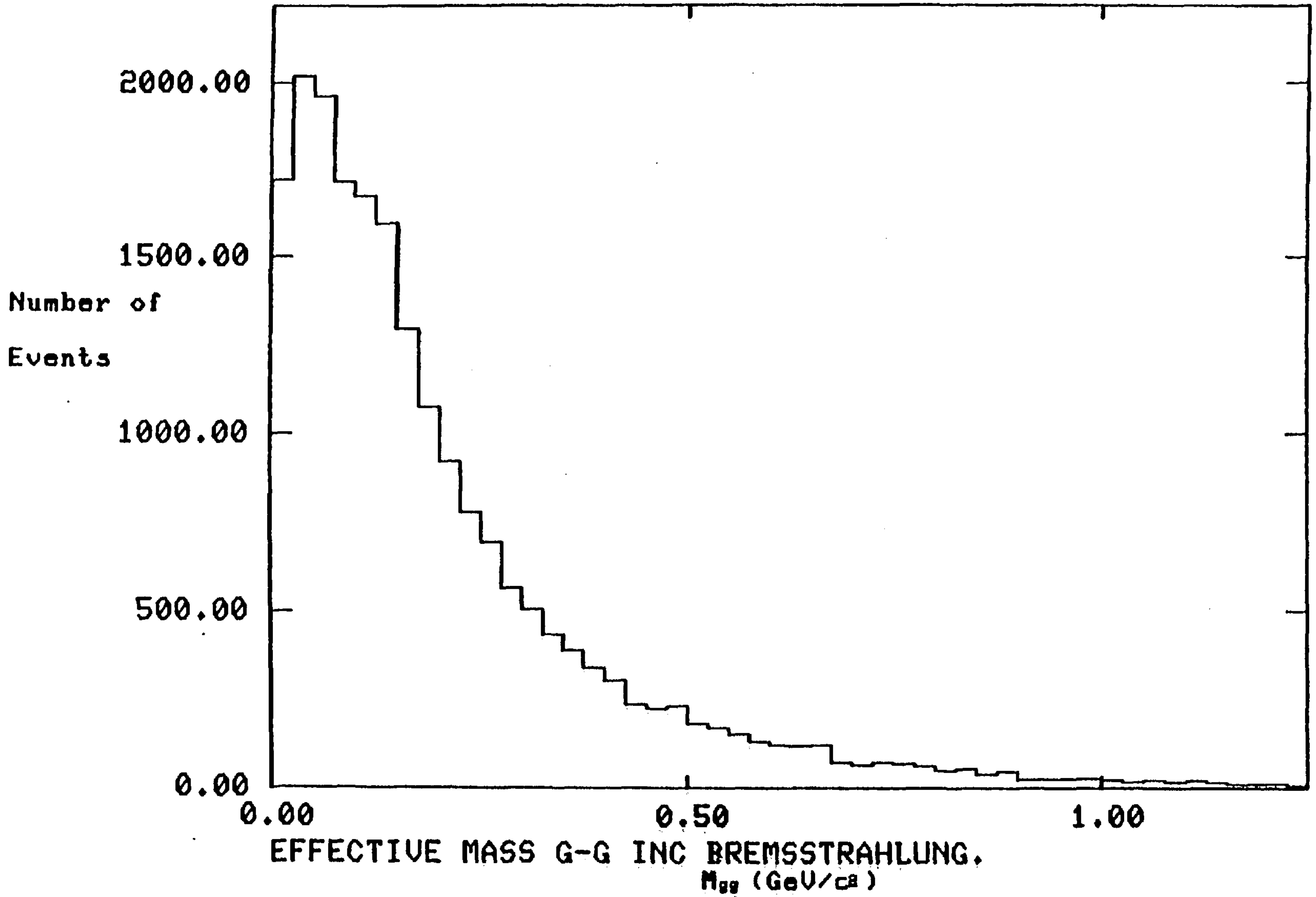
2000.00
1500.00
1000.00
500.00
0.00
Number of Events
0.00
0.50
1.00
EFFECTIVE MASS G-G INC BREMSSTRAHLUNG.
Mgg (GeV/c²)

Fig 4.8

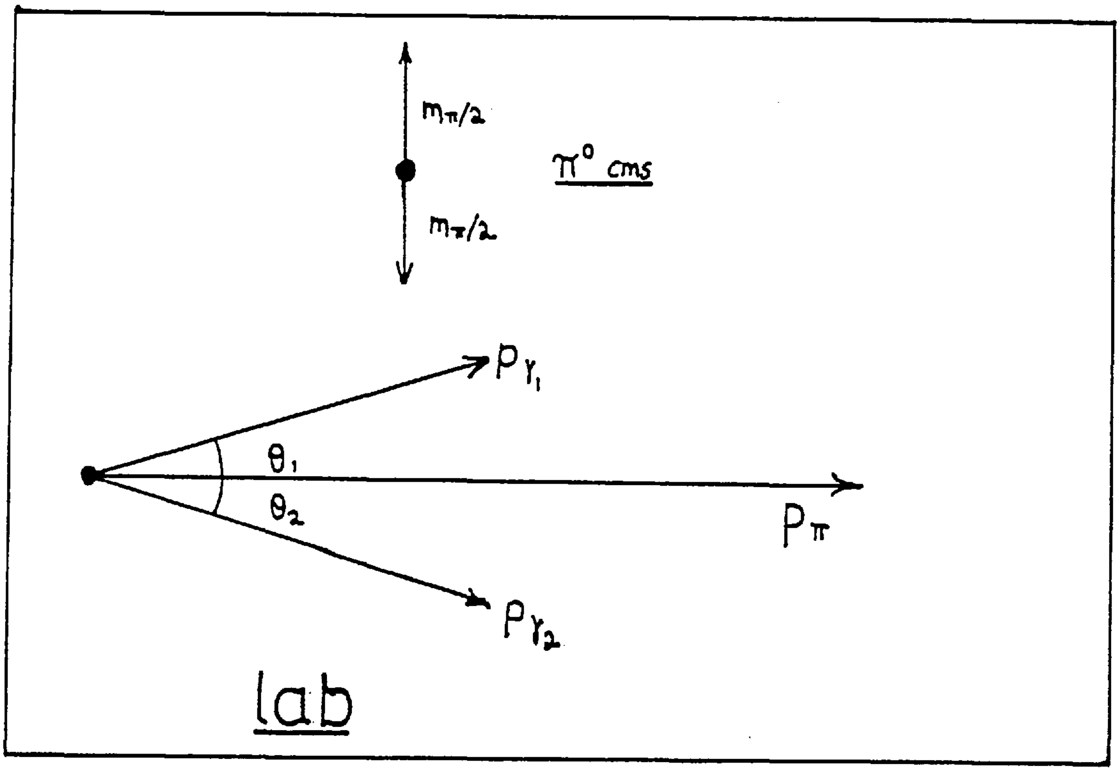

$$P_{\parallel\gamma_1} = P_{\parallel\gamma_2} = P_\pi/2$$

$$P_{T\gamma_1} = P_{T\gamma_2} = m_\pi/2$$

$$\theta_1 = \theta_2 = \tan^{-1} m_\pi/P_\pi$$

$$\theta = \theta_1 + \theta_2 = 2\tan^{-1} m_\pi/P_\pi$$

Fig 4.9

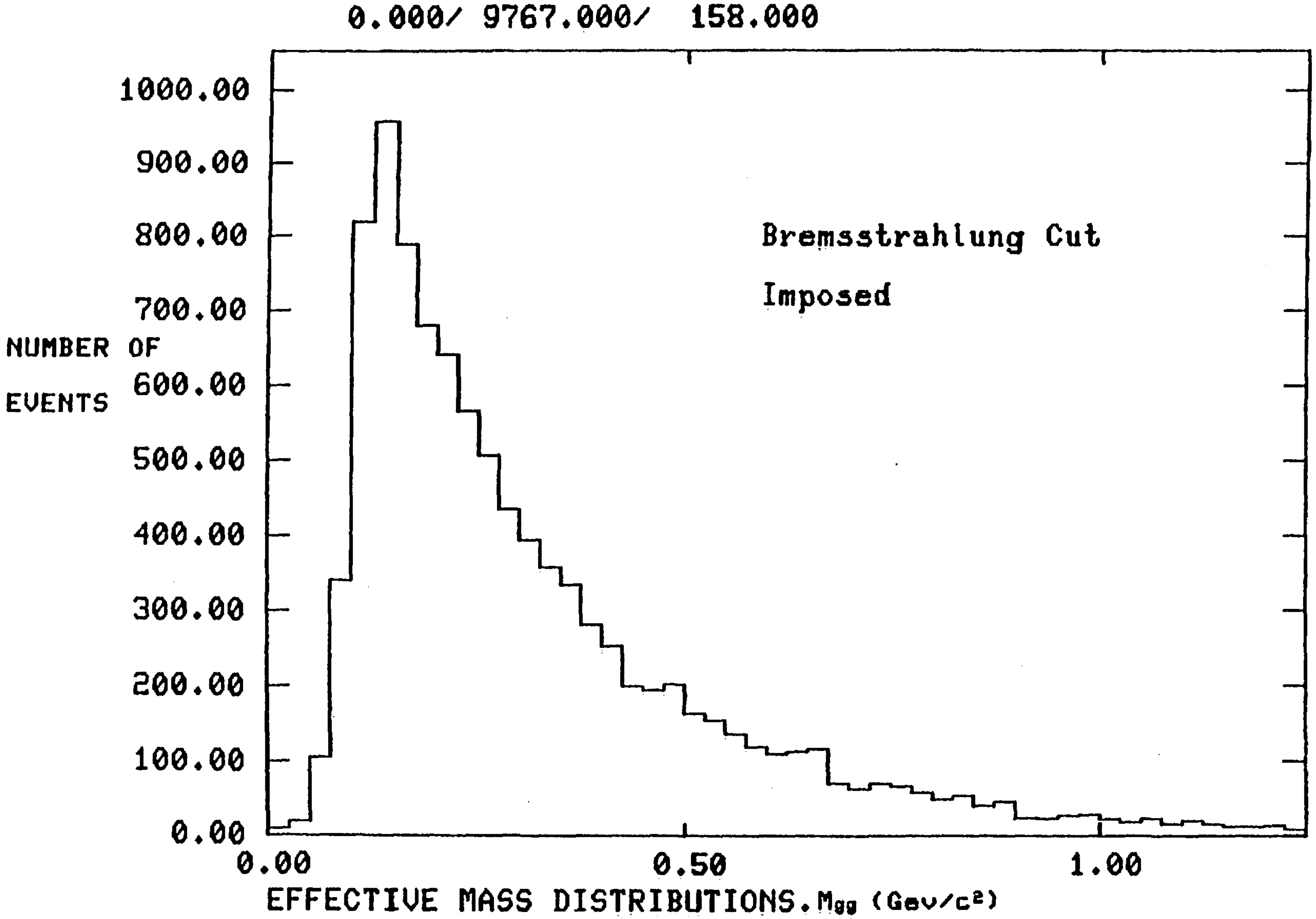
0.000/ 9767.000/ 158.000
1000.00
900.00
800.00
700.00
600.00
500.00
400.00
300.00
200.00
100.00
0.00
NUMBER OF
EVENTS
Bremsstrahlung Cut
Imposed
0.00
0.50
1.00
EFFECTIVE MASS DISTRIBUTIONS. Mgg (Gev/c²)

Fig 4.10

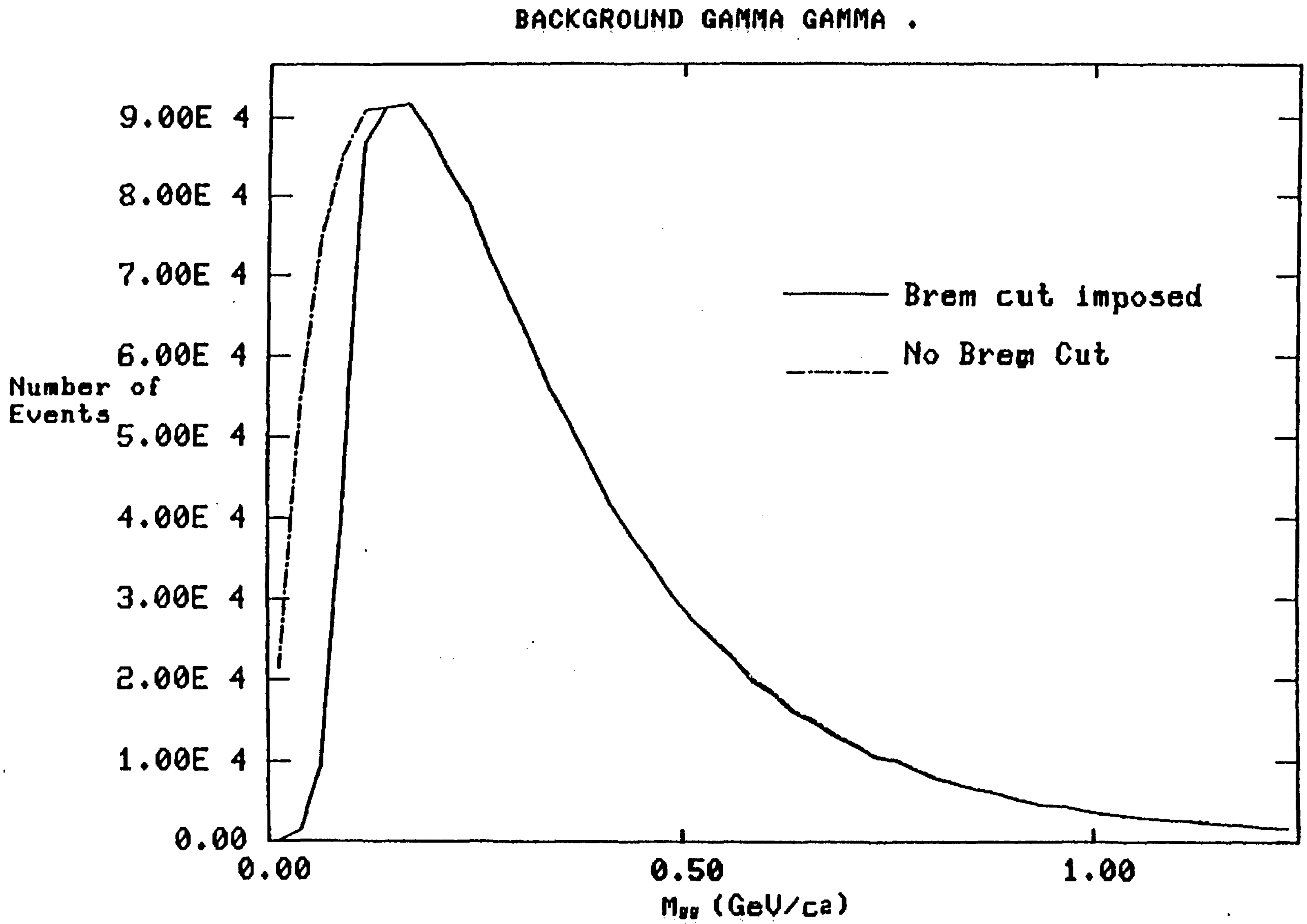
BACKGROUND GAMMA GAMMA .
Number of Events
9.00E 4
8.00E 4
7.00E 4
6.00E 4
5.00E 4
4.00E 4
3.00E 4
2.00E 4
1.00E 4
0.00
0.00
0.50
1.00
Brem cut imposed
No Brem Cut

Fig 4.11

CHAPTER 5

Physics Analysis

Introduction

This chapter concerns itself with the main physics analysis of this experiment. The first section describes the selection criteria for choosing π^0's or η's amongst the $\gamma\gamma$ mass combinations formed as described in chapter 4. The $\gamma\gamma$ mass plot is thus cleaned up by choosing the "best" π^0. The mass resolution is discussed followed by a description of how the refining of the mass plot can still produce a good π^0 inclusive cross-section.

A discussion of the charged multiplicity then follows, in an attempt to derive a value for the π^0 multiplicity. The gamma detection efficiency, an important factor is then discussed, outlining both γ sources and losses. The Parent-Child factors in the high P_T range for both $\pi^0 \to \gamma\gamma$ and $\eta \to \gamma\gamma$ are calculated using a Monte-Carlo method followed by a compilation and comparisons of γ and π^0 production cross-sections.

The Feynman x distribution for both gammas and selected π^0 are plotted followed by the reconstruction of the π^0 x distribution from that of the γ. γ and π^0 invariant P_T distributions are plotted and parameterised.

η production is estimated in several ways : directly from the $\gamma\gamma$ mass plot; high P_T cuts and by requiring a minimum P_T from one gamma. The latter method is shown to be the most successful. An attempt is made to detect the ω^o using its $\pi^o\gamma$ decay mode but only an upper limit to the cross-section is obtained due to both the low $\omega \to \gamma\pi^o$ branching ratio and the experimental resolution.

5.1 π^o,η Selection

Because of the limitations of the kinematic fitting of many gammas described in chapter 4, a different approach is necessary to form π^o's or η's from gammas. It should be remembered, however, that the principal aim of this experiment was to search for unpaired gammas in the P_T range 0.5 to 1.0 GeV/c. Hence the object is to look for any gamma in this P_T range which does not form a π^o or η. Corrections can be introduced to take into account spurious combinatorial background and detection/ recontruction efficiencies. A cut is thus necessary to decide if a certain gamma-gamma combination is compatible with a π^o or η.

5.1.1. Selection Criteria

It was decided to choose as a π^o or η candidate any mass combination which fell within two standard deviations of these masses. For each mass satisfying these criteria, a chi-squared was calculated such that :

$$\chi^2_p = \frac{(M_p - M_{\gamma\gamma})^2}{\Delta M^2_{\gamma\gamma} + \sigma^2_p} \qquad p = \pi \text{ or } \eta \quad ,$$

where σ_p is the width of the fitted π^0 peak. The choice of this parameter was originally arbitrary (in fact, 0) but was evaluated by fitting a gaussian distribution to the π^0 mass. The final choice of σ_p was 20 MeV. This parameter is essentially determined by the finite momentum resolution in Ne/H_2.

For each gamma therefore the effective mass combination with lowest $\chi_\pi^{\,2}$ was chosen as the π^0. All other mass combinations for the two gammas forming this π^0 were rejected. This procedure does not ensure that real π^0's are selected exclusively, as shall be seen. However, it means that gammas from π^0's can be found. If a particular gamma forms two or more combinations compatible with being π^0's, one can be sure that a gamma does come from a π^0, though which is the true π^0 is not necessarily known.

This $\gamma\gamma$ effective mass plot is shown in fig. 5.1a. Superimposed on this is the background (normalised so that the areas above 250 MeV are equal) together with a gaussian. Fig. 5.1b shows this with background subtracted. At the η mass (550 MeV) no enhancement is obvious, but within 20% of this mass (the mass resolution) is an enchancement at 625 MeV. This is probably the η signal. More will be said about this in due course.

The width of the gaussian fit to the π^0 is 20 MeV, the fitted mass 137 MeV. As a comparison fig. 5.2 shows a 2 gamma mass plot for 110 K^-p interactions in

BEBC filled with liquid H_2. Here the width is less than 3 MeV. What one gains in resolution one loses in numbers; that particular experiment loses 90% of its gammas so in order to look for direct photons one would need over 20 to 50 times the number of events of this experiment. Also one is not hindered as much by bremsstrahlung or the massive combinatorial problems in H_2 as in a heavy neon mix. However to determine the gamma detection inefficiency one would need a very much greater number of events in hydrogen and the matter is further complicated by the much stronger dependence of radiation length on energy for hydrogen.

5.1.2 Mass Resolution

Fig. 5.3 shows a plot of $< \Delta M_{\gamma\gamma}/M_{\gamma\gamma} >$versus $M_{\gamma\gamma}$ where $\Delta M_{\gamma\gamma}$ is the error on $M_{\gamma\gamma}$ as computed from the error matrix on P, λ, ϕ of the two gammas. From 75 MeV upwards $<\Delta M_{\gamma\gamma}/M_{\gamma\gamma}>$ is virtually constant at around 20%, $< \Delta M_{\gamma\gamma} >$ is about 25 MeV in the π^o region and has increased to 110 MeV in the η region, making any η signal relatively difficult to resolve.

5.1.3 Number of real π^o's

The determination of the true number of π^o's in the data sample was made as follows. Let there be N_a π^o candidates, that is gamma-gamma combinations satisfying the π^o χ^2 cut. By insisting that no gamma forms more than one π^o and accepting as the "true" π^o the one with lowest χ_π^2 there are N_t (true) π^o's left.

The resulting mass plot is fitted with a gaussian in the π^o mass region together with the background as calculated in Chapter 4, resulting in N_f (fitted) π^o's in the fitted peak. (Fig. 5.1a). Now $N_a > N_t > N_f$. So of the N_t π^o's $N_t - N_f$ are spurious (i.e. from background) combinations. So the other $N_a - N_t$ combinations should be searched to solve further ambiguities.

$$\text{Let } \alpha = \frac{N_f}{N_t}$$

$$\text{and } \beta = \frac{N_t}{N_a}$$

of the $N_a - N_t$ combinations to try, the number left after the second fitting would be $\alpha\beta\ (N_a - N_t)$. After an iterative process- the true number of π^o's should be :

$$N_{true} = N_f + \alpha\beta \sum_{n=1}^{N} (1 - \beta)^n$$

$$= N_f \sum_{n=o}^{N} (1 - \beta)^n \quad .$$

N should be chosen such that the number gained from continuing the series to infinity becomes comparable with the statistical error.

$$N_{true} \simeq \frac{N_f}{\beta} = \frac{N_f . N_a}{N_t} \quad . \tag{5.1}$$

However, we have little idea which combinations are the real π^o's, only how many there are in total. This is a useful result as it means we can make conclusions about the π^o

distributions without actually knowing which are π^o and which are background, and be able to normalise the respective distribution to N_{true}.

5.2. Charged Multiplicities

The distribution of charged multiplicities, $n_c / < n_c >$ is shown in fig. 5.4. The mean multiplicity is 9.15 ± 0.1. Superimposed on this is a curve of :

$$f(z) = (3.79\ z + 33.7\ z^3 - 6.64\ z^5 + 0.332\ z^7)\ e^{-3.04\ z} ,$$

where $z = n_c / < n_c >$, due to Slattery(5.1). The agreement is quite good. Where they differ, particularly one prong events, this can be attributed to scanning biases : most one prong's would appear as through going tracks. As the charged hadrons tend to go forward in a close cone, counting the number of tracks accurately is not easy. There appears to be an oscillation about the curve, with even topologies consistently higher than odd topologies. Two possible reasons are :

(1) scanning bias - the scanner confronted with a large number of tracks tends to round them to an even number. This would be most likely to happen with higher topologies when far more tracks are present. Above multiplicities of 14, odd and even topologies are much closer to the curve than at low multiplicities so this explanation may not be valid.

(2) collisions with hydrogen nuclei - these must be even prongs with a minimum of 2. Only 10% of

interactions are expected to be with hydrogen[2.7] but these may be enough to increase the number of even topologies as shown. Moreover, p-Ne interactions may tend to prefer even multiplicities. Separation, on the scanning table, of p-p and p-Ne collisions is impossible.

The negative multiplicity has a mean of 3.48 ± 0.12.

5.3 Gamma Detection Efficiency

Let the gamma detection efficiency η be defined as the probability for any gamma produced at the primary interaction to appear on the final DST. In order to calculate this we must first consider the possible sources of photons, the processes by which they escape detection and the number of them actually appearing on the final DST.

5.3.1 Sources of Gammas

(a) $\pi^o \rightarrow \gamma\gamma$

This is the major source of photons, produced in 70 GeV/c p-N interactions and so it is important to estimate their yield.

Reviewing the literature on inclusive π^o production at these energies one finds that the π^o multiplicity per event would be of the order of 2.2 to 2.6 in the energy range 69[5.2], to 100 GeV/c[5.3] proton-proton interactions. For p-Ne collisions this would be higher. From ref. 5.4 the number of π^o's per inelastic pp collision for 70 GeV/c lab momentum would be between 2.5 to 2.8. Thus we take the mean π^o multiplicity per event to be 2.8.

From the table of Grote, Hagedorn and Ranft (ref. 2.6), the ratios listed in table 5.1 are approximately true for 70 GeV/c proton-Aluminium interactions and should be approximately true for 70 GeV/c proton - Ne interactions.

Thus the ratio $< n^+ > / < n^- >$ should be roughly 1.6 and :

$$< \pi^- > \quad \simeq \quad 0.86 \ < n^- >$$

and

$$< \pi^+ > \quad \simeq \quad 0.53 \ < n^+ > \quad .$$

Hence the average number of π^0's expected per event will be approximately :

$$< \pi^0 > \ \simeq \ \frac{0.86 < n^- > + 0.53 < n^+ >}{2} \quad .$$

Thus from a measure of the charged multiplicities a reasonable estimate of the number of π^0's per event can be found.

The mean multiplicity is 9.1 and the mean negative multiplicity 3.48, thus the number of π^0's per event will be of the order of 3.0. The value $< n^+ >/< n^- > = 1.63 \pm 0.11$. This estimate of number of π^0's/event is approximate only. Several factors are involved likely to cause considerable error, the chief of these being :

(1) The theoretical model used by ref. 2.6 to calculate the production ratios is open to question and the problem of interpreting this data causes large errors in these ratios.

(2) The problem of scanning the film close to the vertex to count the charged tracks.

(3) Secondary interactions close to the primary vertex which may be counted amongst those from the vertex, lead to an increase in the values of both $< n^+ >$ and $< n^- >$.

Hence the value of 3 π^o's per event estimated in this way should be used more as a crude check on the value of 2.8/event, quoted in table 5.2.

(b) $\eta \to \gamma\gamma$

This process is the second most dominant source of photons. An estimate of η production in this experiment will be attempted later. Results from previous data shows :

$\frac{\eta}{\pi^0}$ = 0.44 ± 0.05 for π^+p and pp interactions, independent of beam momentum for beam momenta above 100 GeV/c and P_T for P_T > 1.5 GeV/c. (Donaldson et al[5.5]).

$\frac{\eta}{\pi^o}$ = 0.55 ± 0.11 at ISR energies and P_T > 3 GeV/c[5.6].

Most data at these energies agree that η/π is in the region of 0.4 to 0.5 and is constant with P_T.

The ratio :

$$\frac{\eta \to \gamma\gamma}{\eta \to \text{all}} = 0.38 \pm 0.01 \quad ,$$

thus around 15% of all gammas are from this source.

(c) $\Sigma^o \rightarrow \Lambda\gamma$

Little data is available at these energies on Σ^o production but using available[5.4] multiplicity data then one would expect about one Σ^o every ten events. In chapter 6 it shall be shown that all gammas from this source are at P_T below 250 MeV.

Other Sources

These are :

$$\omega^o \rightarrow \pi^o\gamma$$

$$\eta' \rightarrow \rho^o\gamma$$

$$\eta' \rightarrow \gamma\gamma$$

These have both low branching ratios and are expected to have low cross-sections so are not major sources of gammas. These will be discussed in more detail in chapter 6 to see if they in any way produce a significant number of high P_T gammas.

These sources are summarised in table 5.2.

5.3.2 Losses of Gammas

The following lists major losses of gammas :

(i) leaving chamber (4%)

(ii) Reconstruction/measuring (14%)

These arise from the following :

(a) asymmetric gammas

(b) low momentum gammas

(iii) Scanning ($\sim$ 20%)

(a) near vertex ($\sim$ 14%)

(b) in the forward "hadron cone"

(i) has been discussed in chapter 3; (ii) was mentioned in chapter 4, but it is clear from plot 4.4 that there is a loss of asymmetric gammas. Fig. 5.5 shows the gamma momentum spectrum - there may be a loss at momenta less than 200 MeV. (iii) will be discussed below.

The plot of gamma conversion length is shown in fig. 5.6. This should trivially be an exponential and above lengths of 40 cm this is clearly the case. Below this value, however there is a definite loss of gammas. This loss can be estimated by fitting an exponential and is approximately 14%. The reasons for this loss are due to the charged hadrons from the primary collision, and secondary hadron interactions near the primary, obscuring gammas close to the vertex. Scanning for and measuring gammas in this region is difficult.

Other losses can be seen in a plot of $\cos\theta^*$ in the gamma-gamma centre of mass, the direction of the gamma-gamma pair defining the axis (fig. 5.7). This should be an isotropic distribution but as can be seen, there is a large loss at $|\cos\theta^*| \simeq 1$. The loss could be due to the background gamma being of low energy when boosted into the lab frame.

Many of the losses are related, e.g. low momentum asymmetric gammas near the vertex are both difficult to scan for, to measure and to reconstruct. Estimating the scanning efficiency at 80%, the overall loss is roughly 34%, agreeing with the efficiency as calculated from the possible gamma sources.

Thus by considering the processes which cause losses of gammas and making reasonable estimates of those losses one cannot directly calculate, we obtain an overall γ detection efficiency of 66%. An estimate of the error on this is 5%. Using this information we can proceed to calculate γ production cross-sections.

In any event the inefficiency for finding gammas on the scanning table can be made almost zero by scanning again and again those frames with an unassociated high P_T gamma, so the scanning efficiency does not ultimately affect the value of γ/π^o obtained.

5.3.3 Parent-Child Effects for π^o and η

Given a P_T and x distribution for a π^o we need to know the P_T and momentum distributions of the gammas from the decay, and to investigate the parent-daughter relation in the P_T range of interest.

Adapting the Monte Carlo of chapter 3, used to calculate the gamma detection efficiency, the author generated 10,000 π^o and η, with the same P_T and x spectra for both particles. These decayed and the momentum and P_T distributions for the gammas found. Also, the gammas were given a momentum spread of 20% to simulate the measurement error and the π^o's and η's reconstructed.

For π^o's

Fig. 5.8a shows the momentum spectrum of the π^o

b	"	"	"	"	"	"	γ's
c	"	"	P_T	"	"	"	π^o
d	"	"	P_T	"	"	"	γ's
e	"	"	mass of the π^o				

In the range of $P_T > 0.5$ the child-parent ratio is :

$$\frac{\gamma_\pi}{\pi^o} = 0.577 \pm 0.02 \quad .$$

It can be seen that the γ momentum is peaked much lower than that of the π^o and is much narrower.

The P_T distributions are very dissimilar - the π^o being a broad distribution peaked at around 150 MeV and falling slowly, the γ P_T distribution is peaked towards zero and falls rapidly so that few gammas occupy the region above 0.5 GeV/c compared to the π^o.

From fig. 5.8 the π^o is quite wide - about 25 MeV half width half maximum.

For η's

The relevant distributions are shown in figs. 5.9 a to e. The η momentum distribution is much wider and flatter than that of the π^o and the resultant γ momentum spectrum is broader and peaked at about 300 MeV.

More importantly the γ P_T spectrum is very similar to the parent η spectrum - broad and falling slowly. The child-parent ratio above P_T of 0.5 GeV/c :

$$\frac{\gamma_\gamma}{\eta} = 1.1 \pm 0.03 \quad .$$

The P_T distribution for γ's from π^0's illustrates that the parent-daughter ratio falls below unity only for $P_T < 350$ MeV/c and consequently why the P_T region above 0.5 GeV/c was chosen for this experiment. Below 400 MeV/c P_T the number of gammas rises rapidly, requiring more gammas to be looked at individually and the consequent increase in combinatorial problems.

5.3.4 Gamma Production Cross-Section

At this stage we can now produce a cross-section for the reaction :

$$p + Ne \rightarrow \gamma + X \quad .$$

With 4832 γ's selected from 1102 events, a γ detection efficiency of (67 ± 5)% and a p-p cross-section of 40 mb :

$$\sigma\ (p + Ne \rightarrow \gamma + X) = 262 \pm 22 \text{ mb/nucleon}$$

If the cross-section :

$$\sigma\ (p + Ne \rightarrow \pi^0 + X) = 112 \text{ mb} \quad (\text{i.e. } 2.8\ \pi^0/\text{event}),$$

and $\qquad \gamma/\pi^0 \simeq 0 \quad ,$

then $\qquad \eta/\pi^0 \simeq (45 \pm 26)\%.$

This figure should not be treated as being significant as the detection efficiency was calculated assuming an η/π^o of around 40%.

5.4.1 X Distributions of Gammas

The Feynman x distribution $(2P_L^*/\sqrt{S})$ for all gammas is shown in fig. 5.10a. This peaks at x slightly greater than 0.0. This has been seen in another heavy liquid bubble chamber experiment[5.7] and is due to the approximation that the beam particle interacts with a free nucleon, neglecting any effects due to the nucleus. In p-p collisions we would expect the distribution to be symmetric. From this plot it is possible to see that there is no evidence, in this experiment, of an excess of photons at low x. (Unlike ref. 1.23).

For a set of π^o's with momentum projection $P_i\ (\pi^o)$ on some i^{th} axis, the γ momentum projection on this axis is a rectangular distribution bounded by :

$$\frac{P_i\ (\pi^o)\ -\ (m_{\pi^0}^2\ +\ P_i^{\ 2}(\pi^o))^{\frac{1}{2}}}{2}\ \leqslant\ P_i(\gamma)\ \leqslant$$

$$\frac{P_i\ (\pi^o)\ +\ (m_{\pi^0}^2\ +\ P_i^{\ 2}(\pi^o))^{\frac{1}{2}}}{2}$$

Considering only π^o's of $P_i(\pi^o) > 0$ we get a flat distribution for $0 < P_i(\gamma) < m_{\pi^o}/2$ and components falling to 0 at $m_{\pi^o}/2$ and the upper limit of $P_i(\gamma)$ $(\sqrt{S}/2)$, likewise for $P_i(\pi^o) < 0$ resulting in a $P_i(\gamma)$ distribution in fig. 5.11, peaking at $P_i(\gamma) = 0$.

This also shows that :

$$\left[\frac{d\sigma}{dP_i(\gamma)}\right]_{P_i(\gamma)=0} \doteq \left[\frac{d\sigma}{dP_i(\gamma)}\right]_{P_i(\gamma)=m_\pi/2} + \left[\frac{d\sigma}{dP_i(\gamma)}\right]_{P_i=+m_\pi/2}$$

Fig. 5.10b shows the x_F distribution for gammas from π^o's selected as described earlier, and fig. 5.10c shows the x distribution for these π^o's.

5.4.2 Reconstruction of π^o x Distribution

It can be shown (Appendix B) that :

$$N(P_i) = - q_i \frac{dn}{dqi} \tag{5.2}$$

$$q_i = \tfrac{1}{2}\left[P_i \pm \sqrt{P_i^{\,2} + m_\pi^{\,2}}\right],$$

where $N(P_i)$ is the number of π^o's with projection. P_i and $n(q_i)$ is the number of gammas with momentum projection q_i along the same axis. Transformed to x_F this becomes :

$$N(x_\pi) = - x_\gamma \frac{dn_\gamma}{dx_\gamma} \qquad x_\gamma = x_\pi \pm \sqrt{x_\pi^{\,2} + 4m_\pi^{\,2}/S} \ . \tag{5.3}$$

Hence by differentiating the x distribution of gammas we can reconstruct the π^o x distribution.

Several parameterisations were attempted, the three most successful being :

(A) $$n(x_\gamma) = Ae^{B(x-x_o)} \qquad x > x_o \qquad 5.4a$$
$$= Ae^{C(x_o-x)} \qquad x < x_o \qquad 5.4b$$

4 parameters

(B) $$n(x_\gamma) = Ae^{B|x-x_o|} + Ce^{Dx^2} \qquad \text{all } x \qquad 5.5$$

5 parameters

(C) $$n(x_\gamma) = Ae^{B(x-x_o)} + Ce^{Dx^2} \qquad x > x_o \qquad 5.6a$$
$$= Ae^{E(x_o-x)} + Ce^{Dx^2} \qquad x < x_o \qquad 5.6b$$

6 parameters

The parameter x_o is used because the gamma x distribution is clearly offset from $x = 0$. (See fig. 5.10a)

In each case MINUIT(5.8) was used for the fitting and the resulting parameterisation differentiated to reproduce the π^o x distribution. This was then superimposed on, and normalised to the x distribution from the selected π^o's.

Parameterisation A

This was the least successful of the three : χ^2 for the fit was 109.7 with 20 degrees of freedom.

The curves for both gammas and π^o's are shown in fig. 5.12a,b.

For $x < 0$ the curve poorly fits the π^o distribution. The problem around $x = 0$, common to all three parameterisations, is that the region $- m_\pi/\sqrt{S} < x < m_\pi/\sqrt{S}$ is not used in the differentiation and so at $x_\pi = 0$, the fit is not well constrained. In an attempt to solve this, the region around $- m_\pi/\sqrt{S} < x_\pi < m_\pi/\sqrt{S}$ was a superposition of the fits to the two separate hemispheres.

Parameterisation B

The χ^2 for this fit was 72.4 with 19 degrees of freedom. Again the π^o curve fails to adequately fit the data . Fig. 5.13a,b.

The value of x_o in this parameterisation was 0.0083, or 96 MeV, the highest of the three.

Parameterisation C

$\chi^2 = 21$, 18 degrees of freedom, a significant improvement.

The respective gamma and π^o curves are shown in figs.5.14a,b. The curves appear to fit the data extremely well. Certainly the π^o distribution is fitted better with this parameterisation than the other two.

The values for the parameters are shown in table 5.3. The value of x_o is equivalent to a CMS P_L^* of 45 MeV.

This may indicate that some frame dependent process is taking place.

It should be emphasised that the parameterisation has little physical interpretation, it is simply a means of obtaining a reasonable, analytic function, which adequately fits the x_γ data, and can be differentiated to obtain the π^o x distribution.

If all the gammas are due to π^o decay, the first order exponential fall off would be expected to be approximately $m_\pi/\sqrt{S}\ \ln\frac{1}{2}$ or 59.25. For $x > x_0$ this parameter (B in equation 5.6a) is 47.0 ± 2.7 and for $x < x_0$ 76.9 ± 6.6, the mean being 61.8 ± 4.6.

From the parameterisation we can now see if there is an excess at $x = x_0$.

$$\left| n(x_\gamma) \right|_{x_\gamma = x_0} = 739.6 \pm 34$$

$$\left| n(x_\gamma) \right|_{x_\gamma = x_0 - m_\pi/\sqrt{S}} + \left| n(x_0 + m/\sqrt{S}) \right| = 793 \pm 69$$

In other words no low x excess is observable, in constrast to ref. 1.23. However, that particular experiment had over 20 times the statistics of this experiment and was particularly sensitive to the low x region whereas this experiment is not. Also, using their measured π^+ and π^- data they reconstructed the γ x distribution by Monte Carlo. This is a more exact way of recreating the true γ x distribution from π^0's. However, as we have no information on the charged π's we cannot perform this sort of analysis. All we can report is that no low x excess is apparent. The difference may be due to the lower (10.5 GeV/c πp) momentum or the lower density (32% molar Ne) bubble chamber mix of that experiment.

5.4.3 Problem of Gammas from η

The gammas from η decay would have a much broader x distribution with a half height at $x = \pm\, m_\eta/\sqrt{S}$. Moreover, with the number of gammas from etas, probably no more than 15% of those from π^o's, this source is but a minor contribution of the total.

5.5 P_T Distribution Gammas

The raw P_T distribution for gammas is shown in fig. 5.15. Also plotted in fig. 5.16 is the distribution

$$\frac{E_{cm}}{P_T} \frac{dN}{dP_T} \quad \text{versus } P_T \quad .$$

A least squares Fit to is this exponential parameterisation :

$$\frac{E_{cm}}{P_T} \frac{dN}{dP_T} = Ae^{-\alpha P_T} \quad ,$$

gives $\alpha = 6.25 \pm 0.08$. The mean P_T is 194.5 MeV/c.

In Fig. 5.17 is plotted for all π's with a $\chi^2 < 0.5$ distribution.

$$\frac{E_{cm}}{P_T} \frac{dN}{dP_T} \quad \text{versus } P_T \quad ,$$

Also shown is a curve resulting from a least squares fit to the exponential parameterisation which gives $\alpha = 5.3 \pm 0.15$.

$$\frac{E_{cm}}{P_T} \qquad \frac{dN}{dP_T} \quad = \quad Ae^{-5.3P_T} \quad .$$

The mean P_T of the π^o's is 340 MeV/c.

Thus for the gammas the invariant differential cross-section :

$$\frac{E_{cm}}{\pi\ \sqrt{S}\ P_T} \qquad \frac{d\sigma}{dP_T} \quad = \quad 10.2\ e^{-6.2\,P_T}\ \ \text{mb}\ C^2/\text{GeV}^2 \quad .$$

For π^o's the corresponding cross-section is :

$$\frac{E_{cm}}{\pi\ \sqrt{S}\ P_T} \qquad \frac{d\sigma}{d\ P_T} \quad = \quad 4.4\ e^{-5.3\ P_T}\ \ \text{mb}\ C^2/\text{GeV}^2 \quad .$$

This exponential fall is not inconsistent with the $e^{-6\ P_T}$ found at low P_T in other experiments.[(5.9)]

5.6 η Production

No data is currently available in the P_T region below 1 GeV/c for the production of the η. Moreover, little evidence of the η has been found in heavy liquid bubble chambers. The η has been looked for in this experiment and the results are presented below.

5.6.1 Using γγ Mass Plot

A slight enhancement is observable in the γγ effective mass plot of fig. 4.8 at around 600 MeV. A definite peak is observable in the π^0 enhanced plot of fig. 5.1a. and shows up even more clearly in fig. 5.1b. The problem with this is that the peak is higher than the η mass (550 MeV/c^2) by 75 MeV. Although within 1SD of the η mass one should treat the η/π^0 value obtained by fitting this peak with caution.

A least squares gaussian fit to this enhancement produces a mass at 635 MeV, 24 MeV wide, half width half maximum (fig. 5.18), much smaller than the 100 MeV width one would expect. From this fit the η/π^0 ratio for the P_T region 0 - 1 GeV/c is :

$$\frac{\eta}{\pi^0} = (30 \pm 14)\%$$

However, as the $< \Delta M_{\gamma\gamma}/M_{\gamma\gamma} >$ is 20%, any η signal will be smeared over the region 440 to 660 MeV, as can be seen in fig, 5.9e., and swamped by the background. At the 95% confidence level, though, $2\% < \eta/\pi^0 < 58\%$. Attempts will now be made to increase the signal/Background ratio.

5.6.2 Significance of this Approach

In order to check the significance of the η signal we must see how many η's we would expect above the back-ground for a given value of η/π^0 and a mass resolution $\Delta m/m$ of 20%. The number of π^0's in fig. 5.1a is :

$$N_\pi = \sqrt{2\pi}\; A_\pi\; \sigma_\pi \qquad .\; A_\pi = 285$$
$$\sigma_\pi = 19\ \mathrm{MeV/c^2}$$

For a gaussian :

$$N_\eta = \sqrt{2\pi}\; A_\eta\; \sigma_\eta \qquad ,$$

$$\text{if } N_\eta/N_\pi = 0.3 \times 0.38 = 0.114 \qquad ,$$

$$\text{and } \sigma_\eta = \frac{m_\eta\, \sigma_\pi}{m_\pi} \qquad ,$$

$$\text{then } A_\eta = A_\pi \times 0.114 \times m_\pi/m_\eta \qquad ,$$

$$= A_\pi \times 0.028 \qquad ,$$

$$= 8 \qquad .$$

Thus a gaussian distribution around the η mass would yield a peak above the background of 8 events. The number of background events at the η mass is 55 ; so the bin at the η mass should contain 63 events. The statistical error on this is 8, so that a 1SD effect would not be expected to be apparent. Doubling the size of the histogram bins would produce 126 hits in the η bin with 16 η's expected. The data are clearly not statistically significant enough to measure the η/π^0 in the P_T region up to 1 GeV/c, in this way.

5.6.3 High P_T Region

In an attempt to determine the η production cross-section for $P_T < 1$ GeV/c, the author selected only those $\gamma\gamma$ mass combinations with a P_T with respect to the beam axis of 0.5 GeV/c or greater and, to cut down combinatorial backgrounds, less than 6 reconstructed gammas on each frame. This is plotted in fig. 5.19. An enhancement at around the mass of the η is clearly visible though lacking statistics. However, it is enough to produce an upper limit.

A gaussian drawn through the η region plus a straight line background are shown in this figure. The gaussian curve is illustrative only, as a large number of equally good curves would serve just as well.

The number of η's found this way, by subtracting the straight line background is 14.2 ± 11.2.

The number of π^o's found in this P_T range on this plot is 80 ± 9.

Hence :

$$\frac{\eta}{\pi} = \frac{14.2}{80 \times 0.38} = .47 \pm 0.39 \quad .$$

It is expected that the cut on the number of gammas per frame should affect π^o and η equally.

Again, the quoted error on the η π^o ratio reflects the poor statistics available. We need a means of evaluating η π^o without actually observing a significant η signal. (It should be remembered that as the η is known to exist then we are not necessarily looking for an unambiguous η signal to extract a value for η/π^{o}).

5.6.4 Using High P_T Gammas

At high P_T (> 0.5 GeV/c) the Parent-Child factor helps considerably. Considering only those gammas in this P_T range , the $\gamma\gamma$ mass plot for these gammas, once spurious π^{o} combinations have been removed (i.e. no more than one π^{o} association per high P_T gamma) is shown in fig. 5.20. Only $\gamma\gamma$ combinations where one gamma has P_T > 0.5 GeV/c are plotted. No background curve is plotted. It is clear that there is a definite enhancement around the η region.

Pairing these high P_T gammas we can make decisions to see which gammas form best a π^{o} or an η. The cut on both these is that the χ^2 as defined in section 5.1 must be less than 2.0 and the best π^{o} or η candidate is taken as being the particle from which this gamma comes. These criteria are better outlined in the next chapter but should a gamma form two or more reasonable π^{o}'s, then this gamma is assumed to be from a π^{o}, and likewise for an η. π^{o} 's can be associated reasonably easily, the η's by hand. If we select only the best π^{o} or η combinations for the 337 high P_T gammas we find 214 associating to π^{o}'s and 75 to η's and 48 unassociated (see next chapter).

With a 67% gamma detection efficiency we should expect only 226 ± 12 gammas to be associated in total (assuming negligible direct gamma contribution), leaving 63 ± 29 combinations which must be spurious associations. Assuming that these are divided between π^o's and η's in the proportion 5 : 2 (this will be justified in chapter 6) then we have :

$$57 \pm 17 \ \eta\text{'s}$$

and $$169 \pm 37 \ \pi^o\text{'s} \quad ,$$

producing γ's of $P_T > 0.5$ GeV/c using the Parent-Child factors from section 5.1. This leads to :

$$\frac{\eta}{\pi^o} = \frac{57}{169 \times 0.38} \times \frac{0.57}{1.1}$$

$$= 0.46 \pm 0.19 \quad .$$

This is, in the P_T range 0.5 to 1 GeV/c, a more convincing value of η/π^o produced by this experiment as it relies on known factors and not on fitting a statistically insignificant bump. All one needs to know about these gammas is which particle, π^o or η, is the parent. No other information about this parent need be known. The gammas in this P_T range can be paired off to form a π^o or an η reasonably unambiguously, and the γ detection efficiency and Parent-Child relations are known.

This value fits in well with the values found from the other methods, and can be used to normalise the value of η/π^0 at low P_T. When this is done then for the range $0 < P_T < 1.0$ GeV/c :

$$\frac{\eta}{\pi^0} = 0.35 \pm 0.16 \quad .$$

These values, η/π^0 vs P_T are plotted in fig. 5.21. Within error bars, then η/π^0 could be constant with P_T over this range. However, there is a definite tendency for η/π^0 to rise with P_T, levelling off to a constant value above P_T of 0.5 GeV/c, at around 0.45, consistent with ISR, FNAL data showing η/π^0 constant with S and P_T. What is important, moreover, is that this is the only available data on η/π^0 in this P_T domain at these energies. At the upper end, η/π^0 seems to be levelling off to the high P_T value of around 0.45. Also no data on η production has been obtained in a heavy liquid bubble chamber before, presumably because these have mainly been confined to very low P_T.

5.7 ω^0 Production

The effective $\pi^0\gamma$ mass plot is shown in figs. 5.22a and b, for π^0 candidates and selected π^0's respectively. The value :

$$\frac{\omega \to \pi^0\gamma}{\omega \to \text{all}} = 8.8\% \quad .$$

A recent experiment[5.10] finds at large P_T :

$$\frac{\omega}{\pi^0} = 0.44 \quad .$$

Therefore the number of gammas from this source would be less than 2% of those from π^o's. Bearing in mind the problems with η's we would not expect to see this decay mode of the ω. Nevertheless, the $\pi^o\gamma$ plots are shown for completeness.

As can be seen no peak is clearly visible, though a slight enhancement is apparent in the region 800 to 950 MeV in 5.22b. This is not statistically significant however. A crude estimate of the number of ω's in this enhancement is 21 but with an error of 27. This would give a limit on ω/π^o of $(22 \pm 30)\%$. though this limit is not significant.

5.8 Conclusions

In summary of the results presented in this chapter :

The gamma production cross-section in the reaction $P + N_e \rightarrow \gamma + x$ at 70 GeV/c beam momentum is :

$$\sigma\ (P + Ne \rightarrow \gamma + x) = 262 \pm 22 \text{ mb / nucleon}$$

and the invariant differential cross-section is :

$$\frac{E_{cm}}{\pi \sqrt{S}\, P_T} \quad \frac{d\sigma}{d\, P_T} = 10.2\ e^{-6.2\, P_T} \quad \text{mb } C^2/\text{GeV}^2 \quad .$$

The gamma x distribution may be parameterised by :

$$\frac{dN}{dx} = Ae^{B(x - x_o)} + C\,e^{Dx^2} \qquad x > x_o$$
$$= Ae^{E(x_o - x)} + C\,e^{Dx^2} \qquad x < x_o \quad ,$$

where the parameters A,B,C,D and E are listed in table 5.3.

The π^o x distribution can satisfactorily be reproduced from this parameterisation by the methods outlined in Appendix B, by differentiating the γ x distribution. No low x gamma excess is apparent.

The π^o cross-section is :

$$\sigma\ (P + Ne \rightarrow \pi^o + x) = 112 \text{ mb/nucleon}$$

the invariant differential cross-section being :

$$\frac{E_{cm}}{\pi\ \surd S\ P_T}\ \frac{d\sigma}{d\ P_T} = 4.4\ e^{-5.3\ P_T} \quad \text{mb}\ \ C^2/\text{GeV}^2 \quad ,$$

consistent with the $e^{-6\ P_T}$ dependence found elsewhere.

η production, studied in a number of reasonably independent ways produces a value of η/π^o in the P_T range below 1 GeV/c of : 0.35 ± 0.16, with a clear indication that η/π^o rises with P_T to a constant value of around 45%. The η cross section is :

$$\sigma\ (P + Ne \rightarrow \eta + x) = 39 \pm 18 \text{ mb/nucleon}$$

These last results are important as they are the only data currently available on η production at low P_T at these energies.

At the 95% confidence level, η/π^o < 66% in the P_T region below 1 GeV/c.

REFERENCES CHAPTER 5

5.1 P. Slattery, Phys. Rev., D7, 2073 (1973).

5.2 V.V. Ammosov et al, Il Nouvo Cimento, 40, 237 (1977).

H. Blumenfeld et al, Phys. Lett., 45B, 525 (1973), and 528 (1973).

5.3 J.W. Chapman et al, Phys. Lett., 47B, 465 (1973).

5.4 E.L. Berger et al, CERN/D.PhII/PHYS., 74-27, 1974.

5.5 G.J. Donaldson et al, Phys. Rev. Lett., 40, 684 (1978).

5.6 F.W. Busser et al, Phys. Lett., 55B, 232 (1975).

5.7 J.R. Elliot, Private Communication to T.C. Bacon.

5.8 MINUIT CERN Program Library, D506.

5.9 See (e.g.) D.R.O. Morrison, CERN/D.PhII/PHYS., 73-11.

5.10 G.J. Donaldson et al, BNL, 26316 OG473 (1979).

TABLE CAPTIONS

5.1 Approximate particle production ratios in 70 GeV p-N collision from Hagedorn-Ranft.

5.2 Sources of Gamma.

5.3 Best parameterisation for gamma x distribution.

TABLE 5.1

Approximate Particle Production Ratios in 70 GeV

p-Nucleon Collision

$\langle \pi^+ \rangle / \langle \pi^- \rangle$	$\sim$ 1
$\langle \pi^+ \rangle / \langle p \rangle$	$\sim$ 1.5
$\langle \pi^+ \rangle / \langle K^+ \rangle$	$\sim$ 6
$\langle \pi^- \rangle / \langle K^- \rangle$	$\sim$ 10
$\langle \pi^- \rangle / \langle \bar{p} \rangle$	$\sim$ 100
$\langle \pi^- \rangle / \langle \Sigma^- \rangle$	$\sim$ 20
$\langle \pi^+ \rangle \quad \langle \Sigma^+ \rangle$	$\sim$ 20

TABLE 5.2

Sources of Gammas

		$\underline{\gamma/ev}$
$\pi^o \rightarrow \gamma\gamma$ at 2.8 π^o/event (5.2, 5.3, 5.4)		5.6
$\eta \rightarrow \gamma\gamma$ at $\eta/\pi = 0.4$ (5.5, 5.6) and $\dfrac{\eta \rightarrow \gamma\gamma}{\eta \rightarrow \text{all}} = 0.38$		0.85
$\Sigma^o \rightarrow \Lambda\gamma$ at 0.1/event (5.3, 5.4)		0.1
Others	<	0.06
		6.55

Expect 6.55 γ/event

We find 4.4 γ/event

Efficiency for any γ to appear on DST is therefore

(67 ± 2.2)%.

TABLE 5.3

Parameterisation C

Parameter	Value	Error
A	673.2	22.5
B	- 47.0	2.7
C	66.4	11.7
D	- 97.5	24.4
E	- 76.9	6.6
x_o	0.0039	0.0006

FIGURE CAPTIONS CHAPTER 5

5.1a $\gamma\gamma$ effective mass plot after removing multiple π^o combinations with a gaussian plotted around the π^o and the background.

b As above but with the background subtracted.

5.2 $\gamma\gamma$ mass plot for the 110 K^-p experiment.

5.3 Plot of $\Delta m\gamma\gamma/m\gamma\gamma$ versus $m\gamma\gamma$.

5.4 Plot of number versus z (z = charged multiplicity/ mean multiplicity).

5.5 γ momentum spectrum.

5.6 Track length γ with exponential fit.

5.7 Plot of cos θ^* where θ^* is the angle of a gamma in the $\gamma\gamma$ centre of mass system.

5.8 Monte Carlo results for $\pi^o \to \gamma\gamma$.

(a) Momentum π^o,

(b) Momentum γ,

(c) P_T π^o,

(d) P_T γ,

(e) Reconstructed π^o from γ's with 20% mean error.

5.9 Monte Carlo results for $\eta \to \gamma\gamma$.

(a) Momentum η,

(b) Momentum γ,

(c) P_T η,

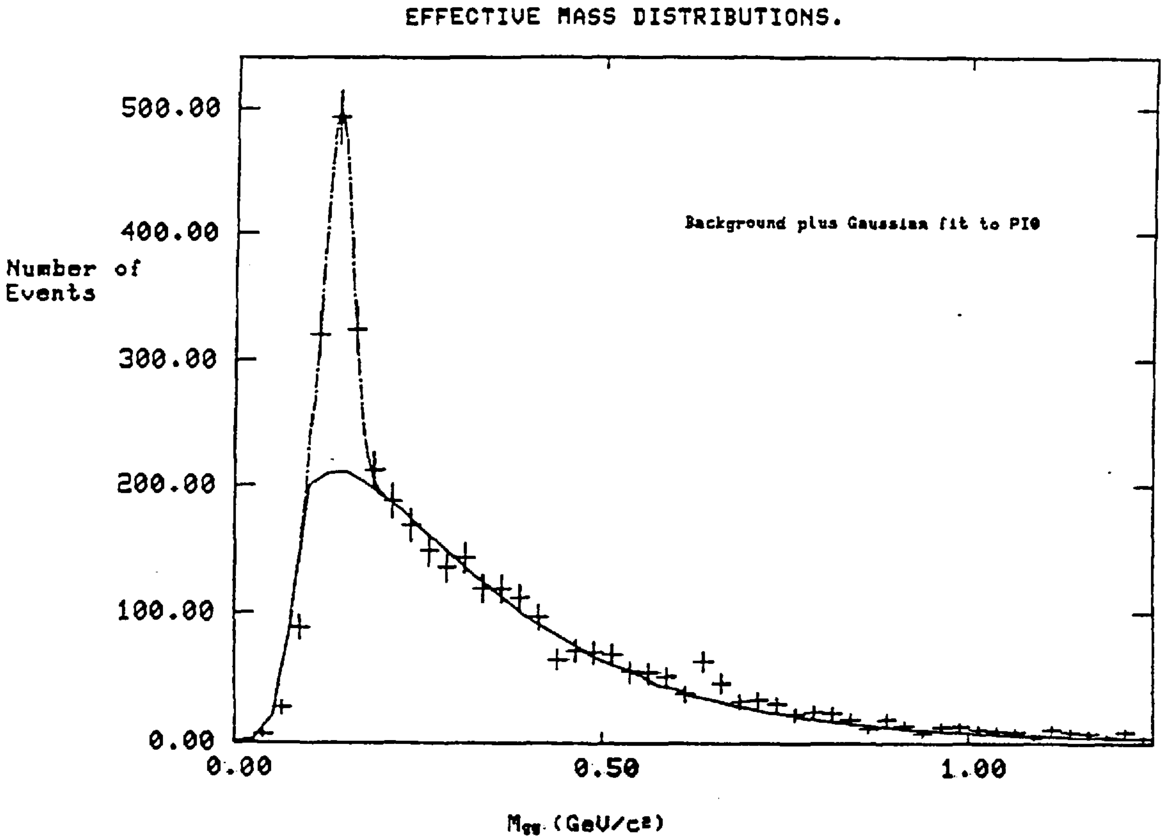

Fig 5.1a

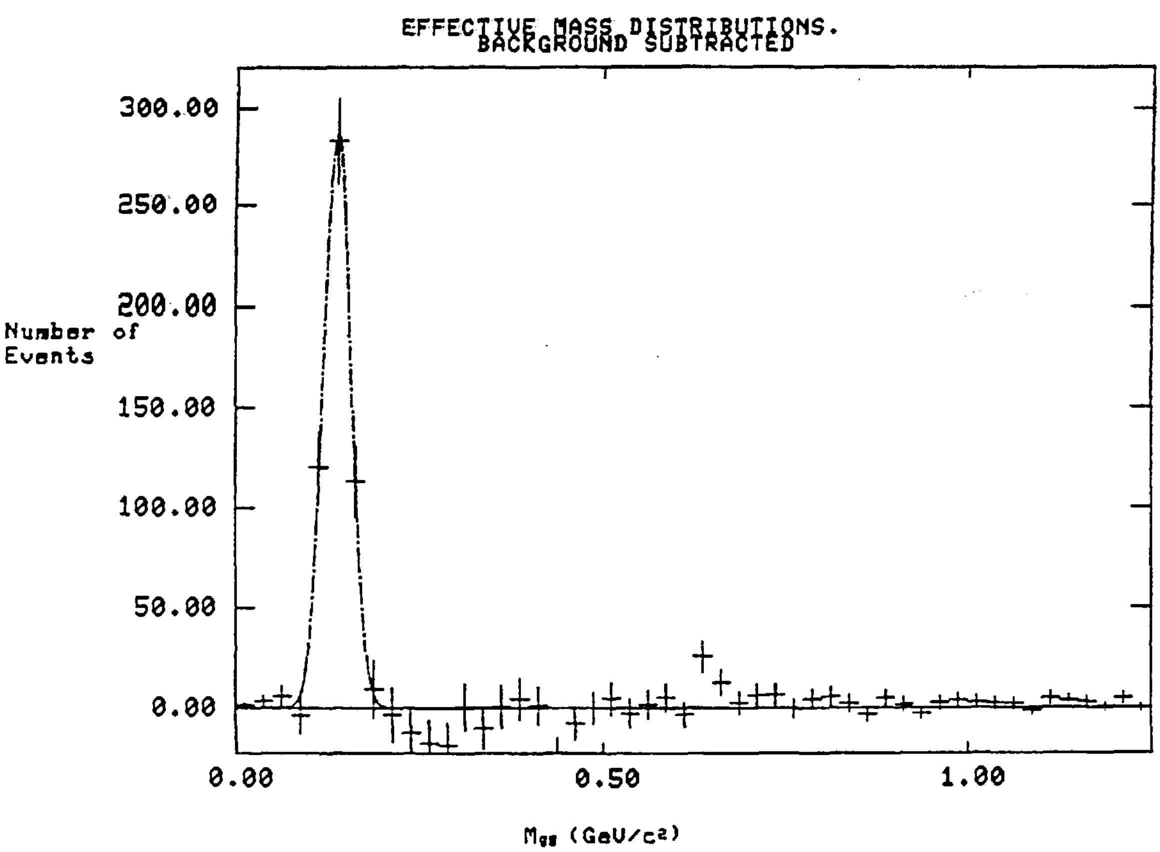

Fig 5.1b

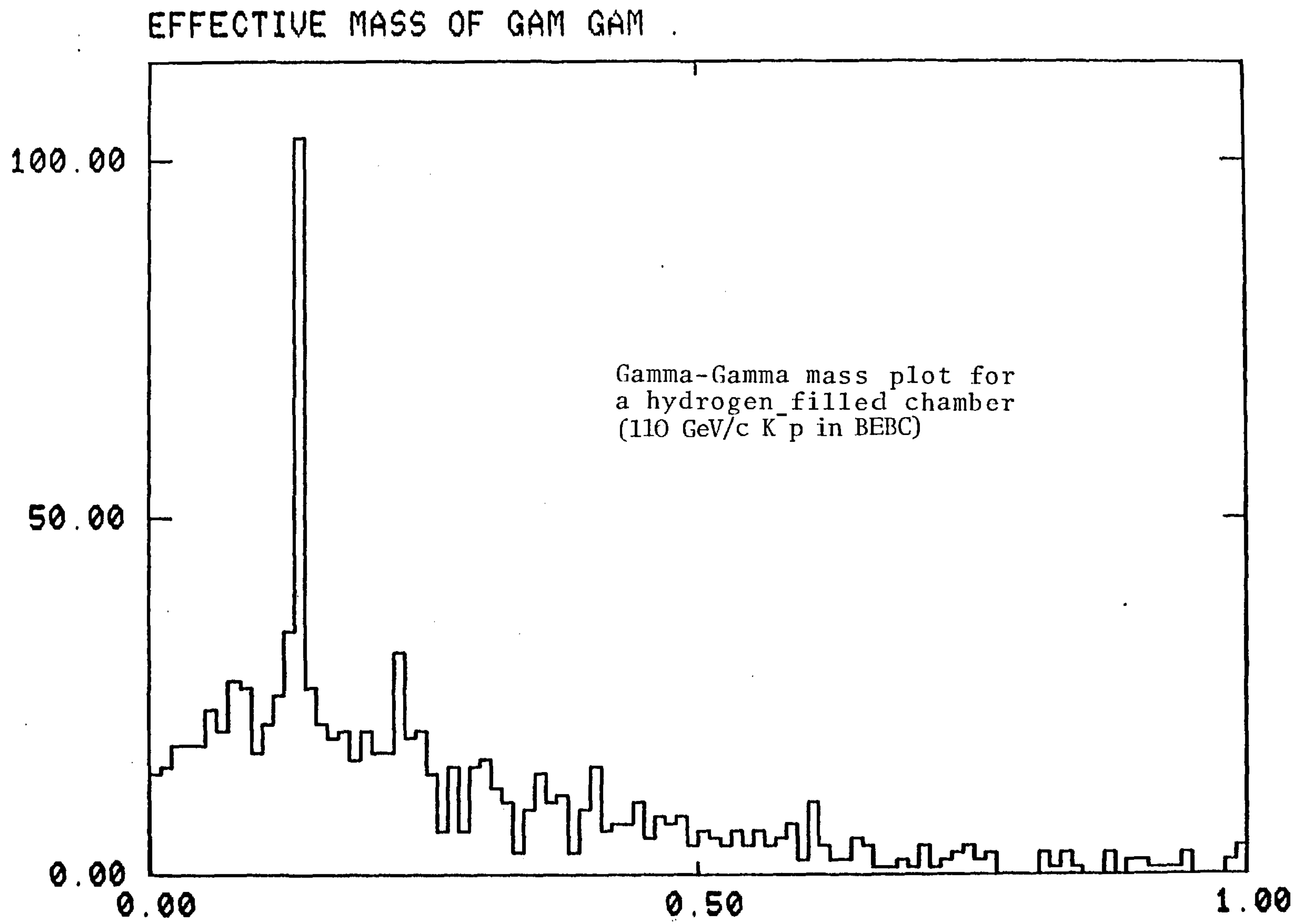

EFFECTIVE MASS OF GAM GAM .
100.00
50.00
0.00
0.00
0.50
1.00
Gamma-Gamma mass plot for
a hydrogen filled chamber
(110 GeV/c K⁻p in BEBC)

Fig 5.2

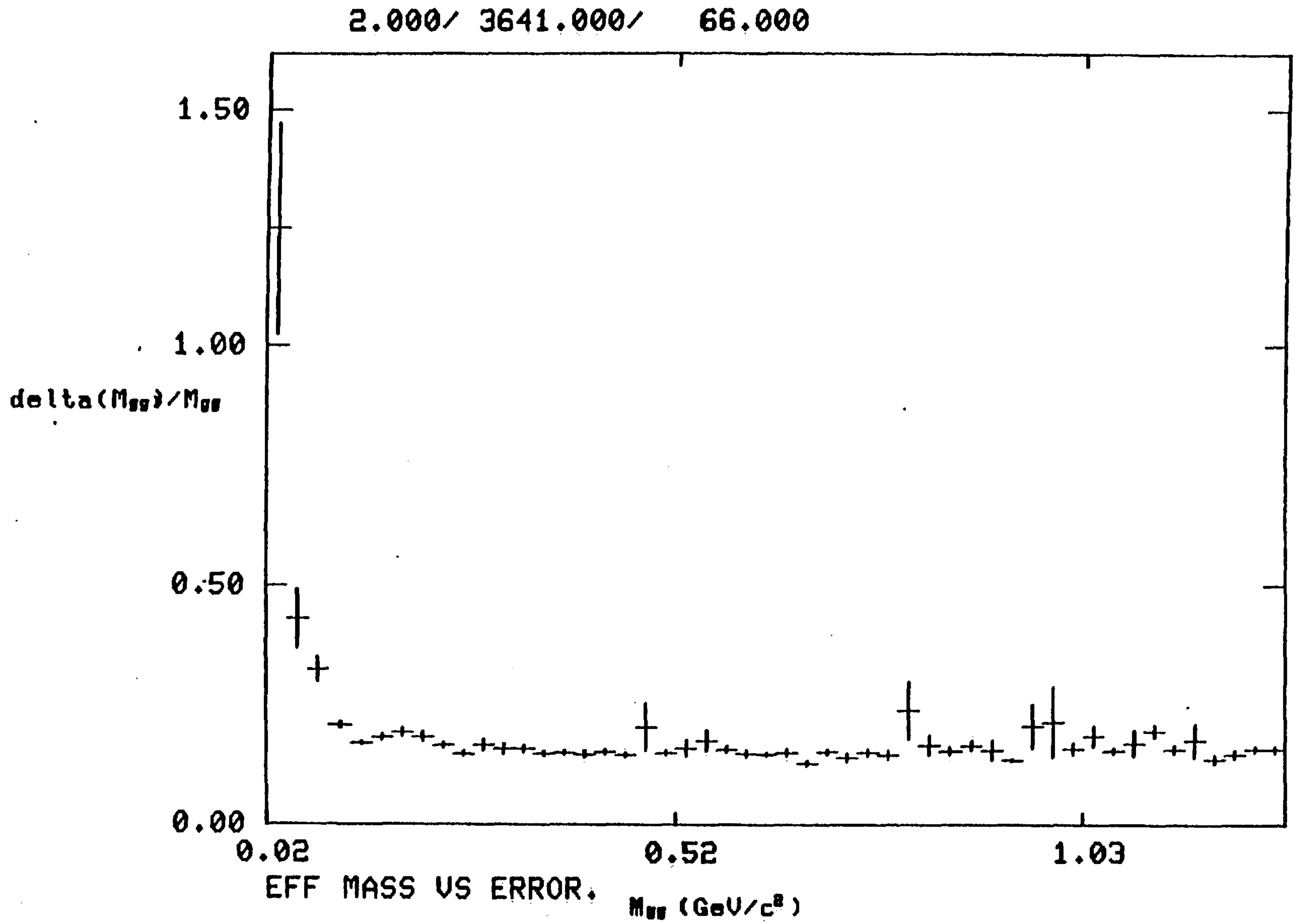

2.000/ 3641.000/ 66.000
1.50
1.00
delta(Mgg)/Mgg
0.50
0.00
0.02
0.52
1.03
EFF MASS VS ERROR.
Mgg (GeV/c²)

Fig 5.3

CHARGED MULTIPLICITY.

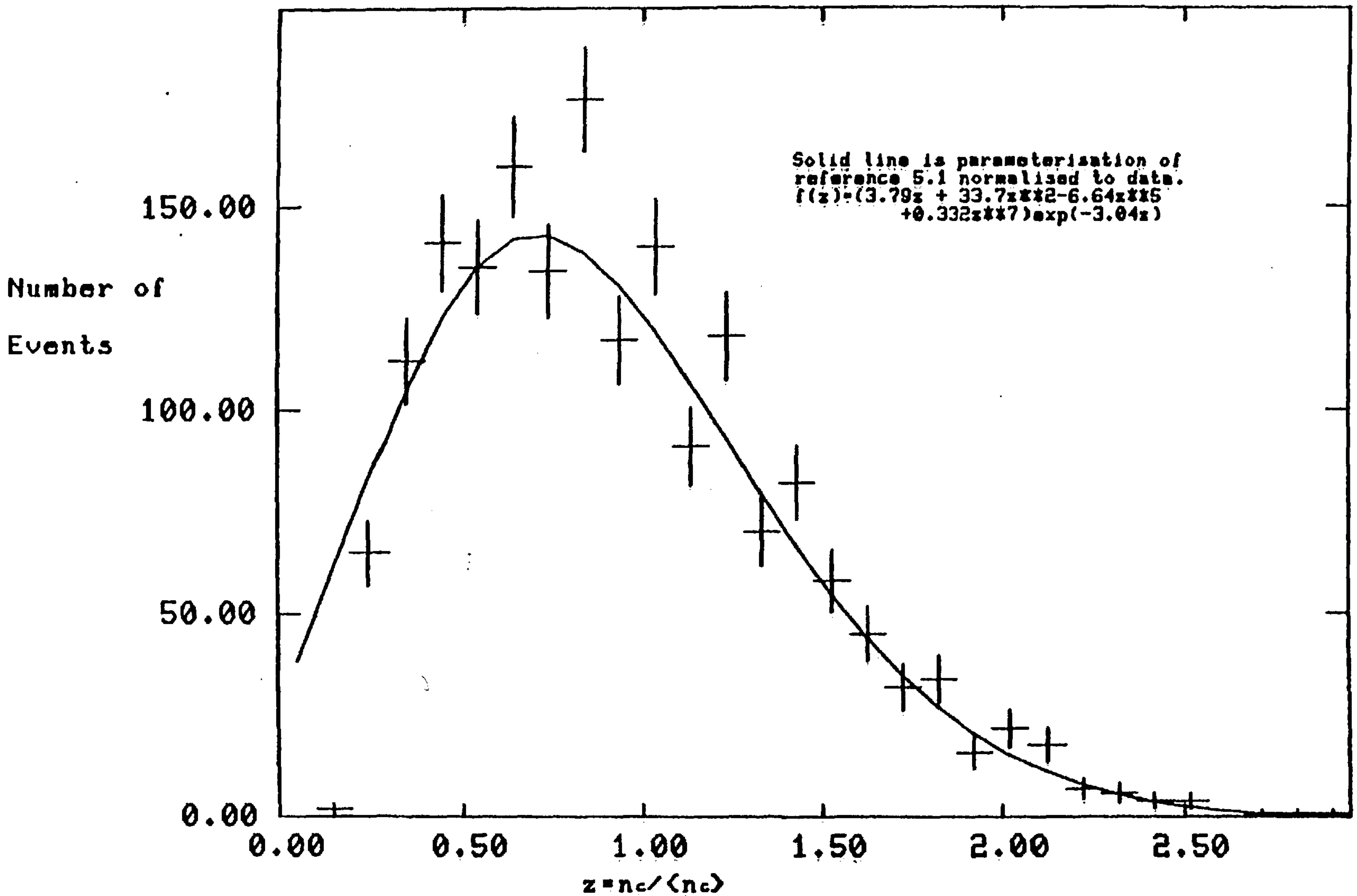

Fig 5.4

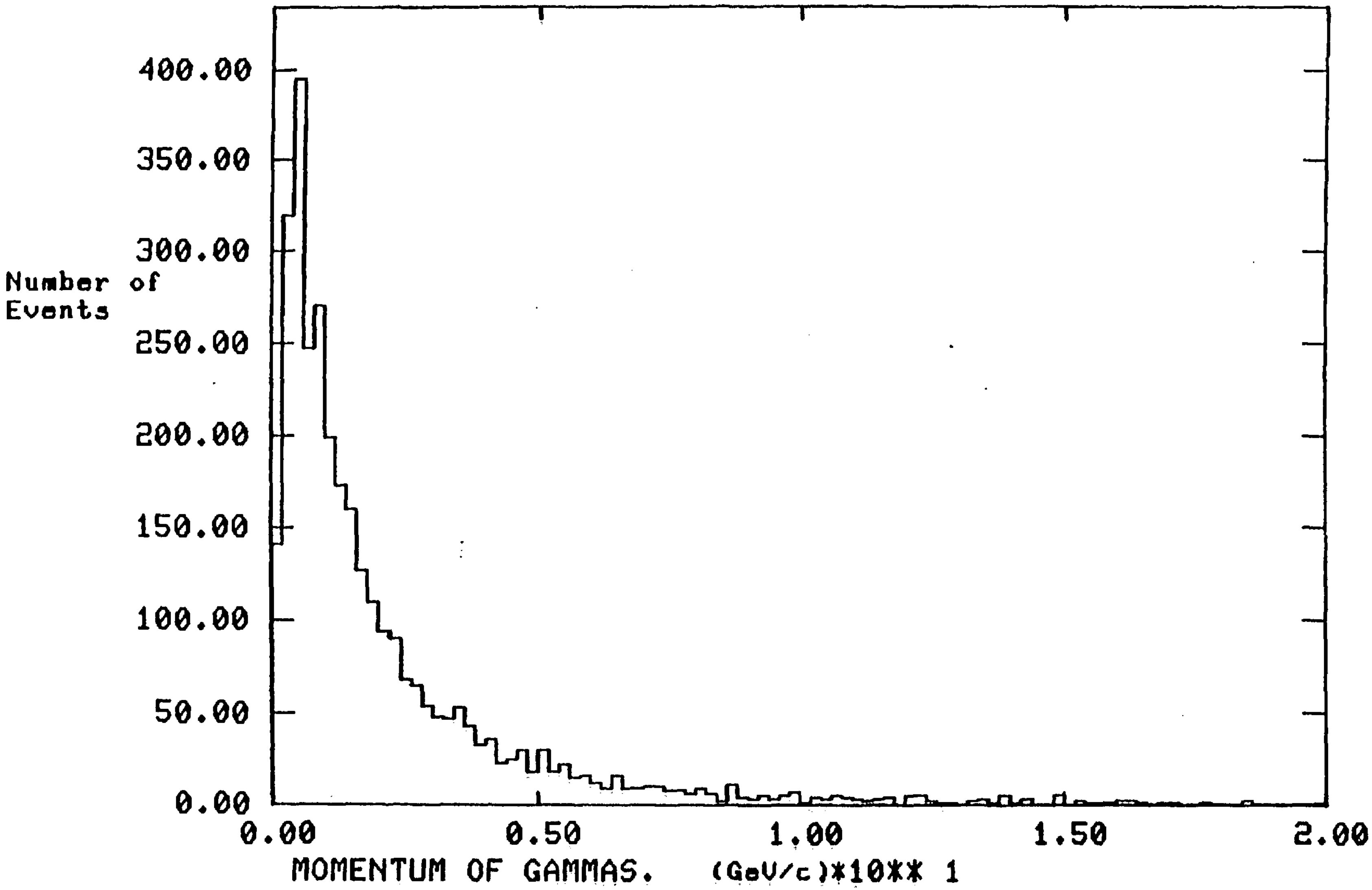
400.00
350.00
300.00
250.00
200.00
150.00
100.00
50.00
0.00
Number of Events
0.00
0.50
1.00
1.50
2.00
MOMENTUM OF GAMMAS. (GeV/c)*10** 1

Fig 5.5

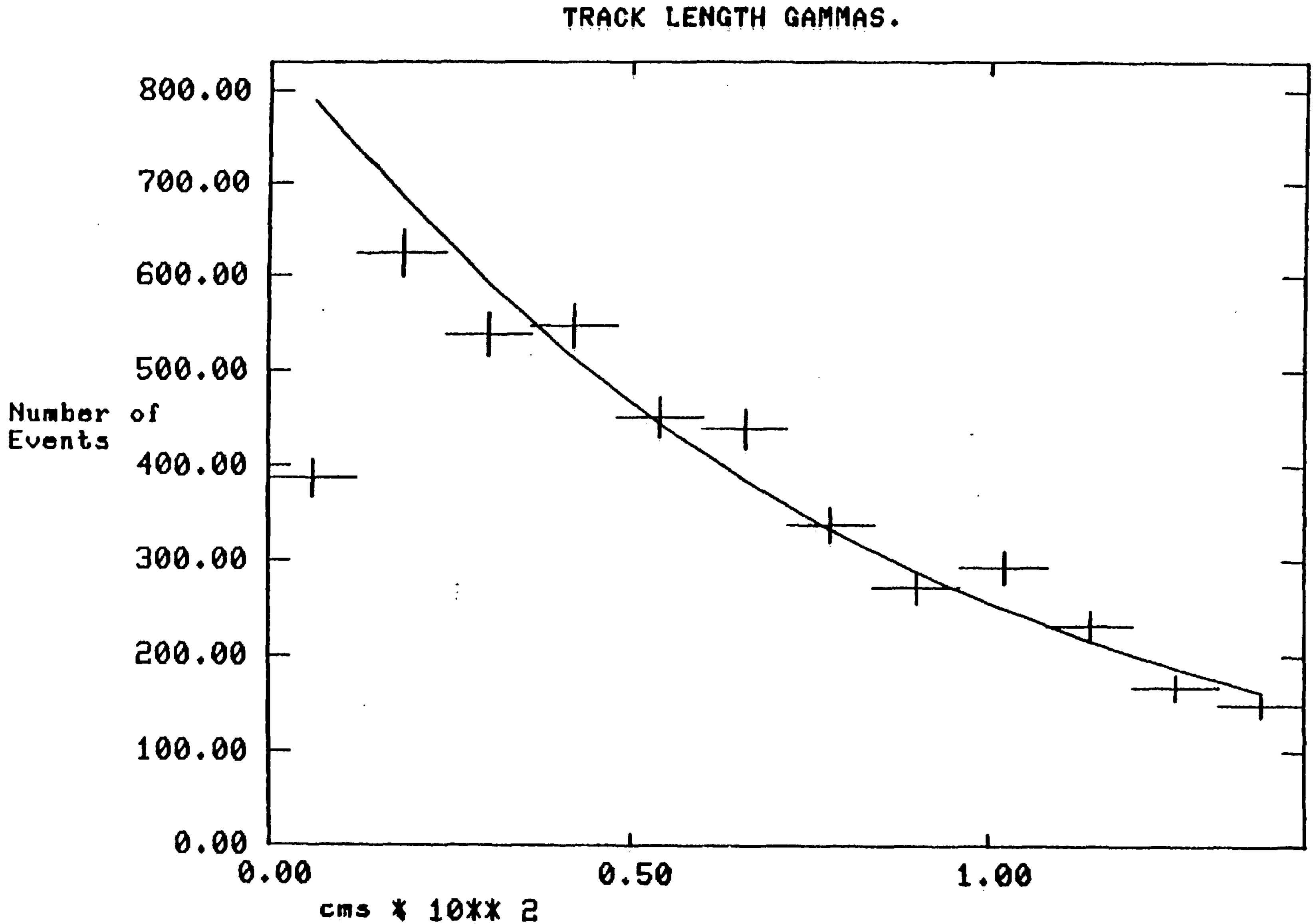
TRACK LENGTH GAMMAS.
800.00
700.00
600.00
500.00
Number of
Events
400.00
300.00
200.00
100.00
0.00
0.00
0.50
1.00
cms * 10** 2

Fig 5.6

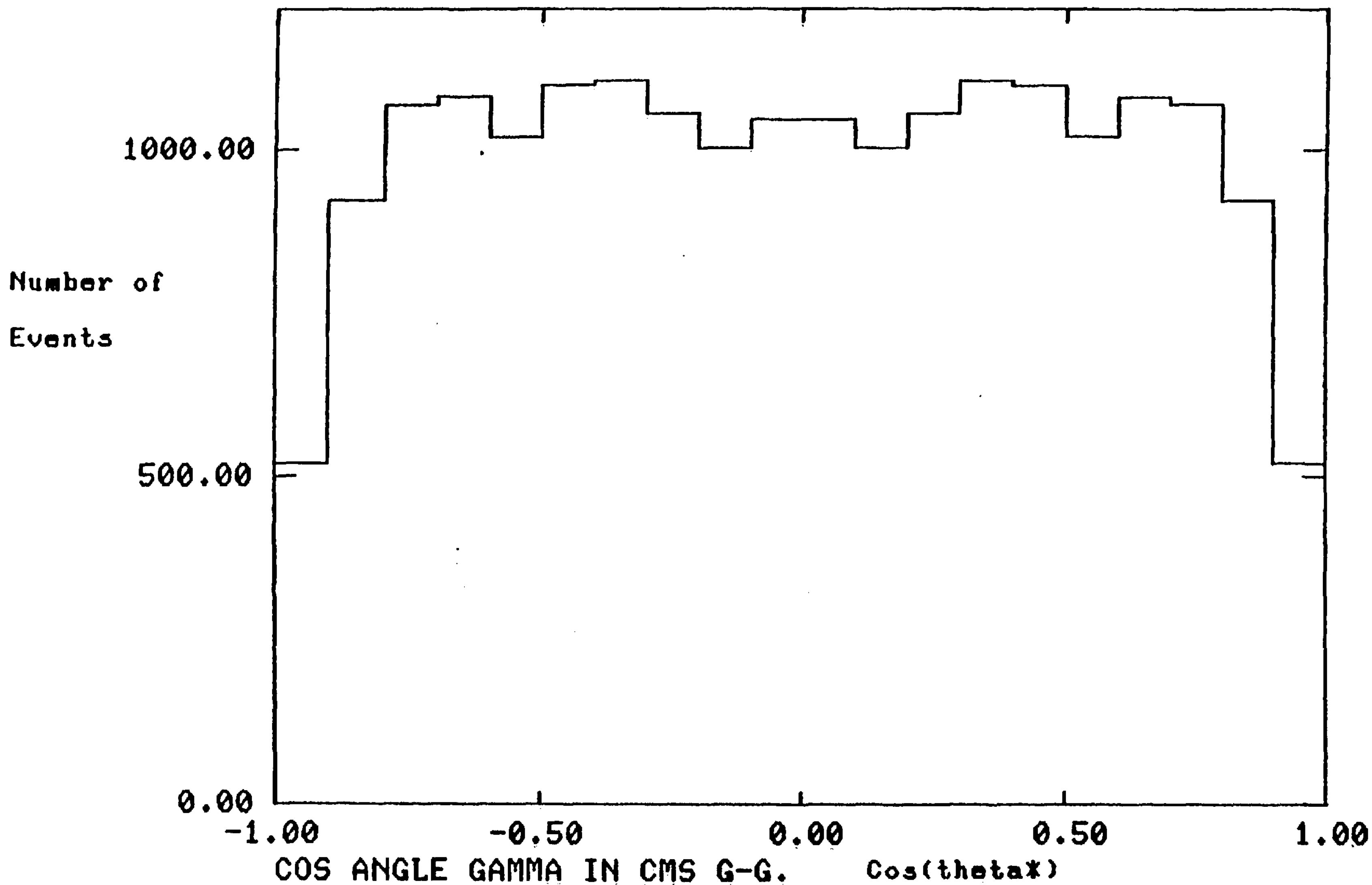

1000.00
500.00
0.00
Number of
Events
-1.00
-0.50
0.00
0.50
1.00
COS ANGLE GAMMA IN CMS G-G.
Cos(theta*)

Fig 5.7

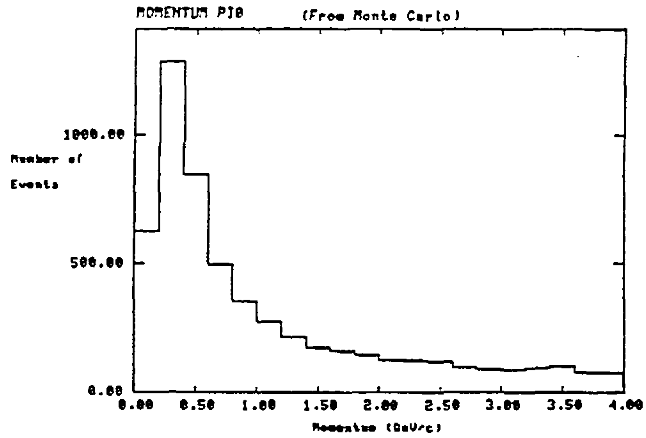

Fig 5.8a

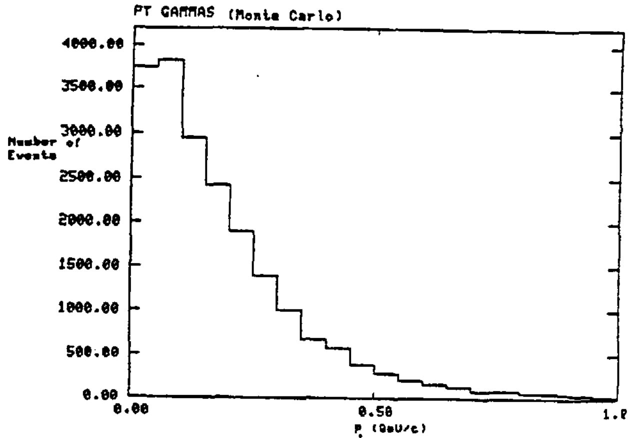

Fig 5.8d

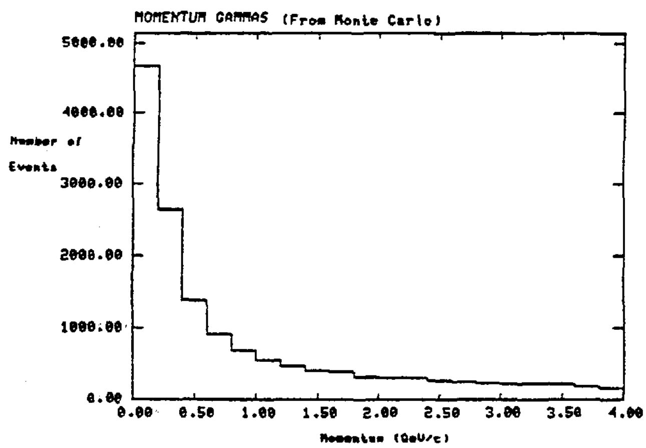

Fig 5.8b

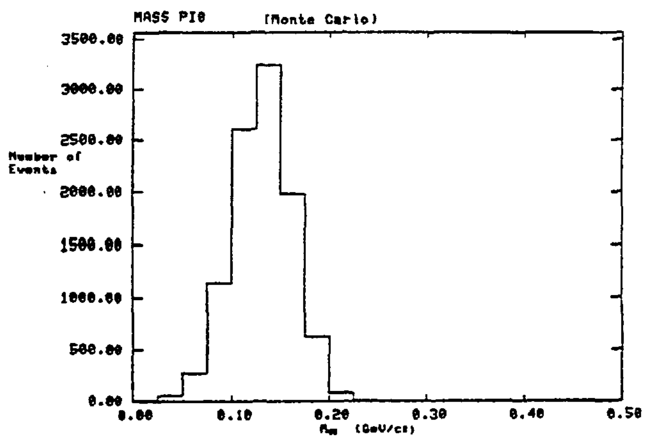

Fig 5.8e

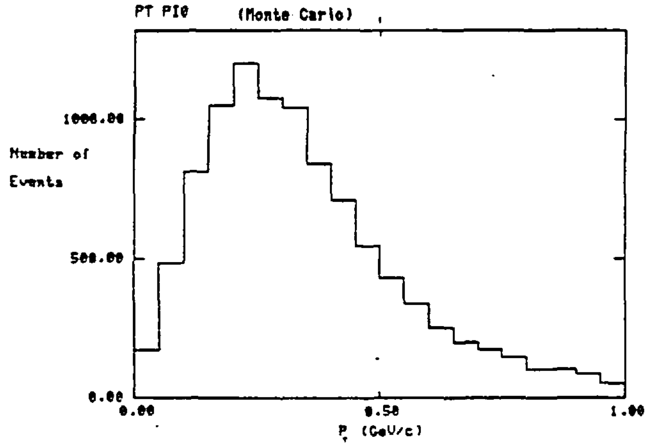

Fig 5.8c

Monte Carlo Plots for pizero to gamma-gamma

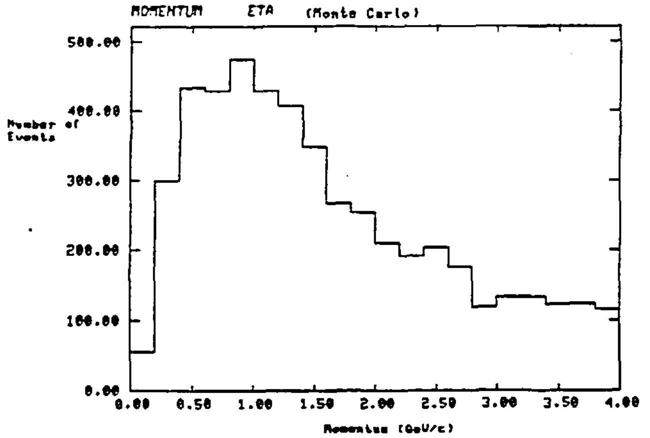

Fig 5.9a

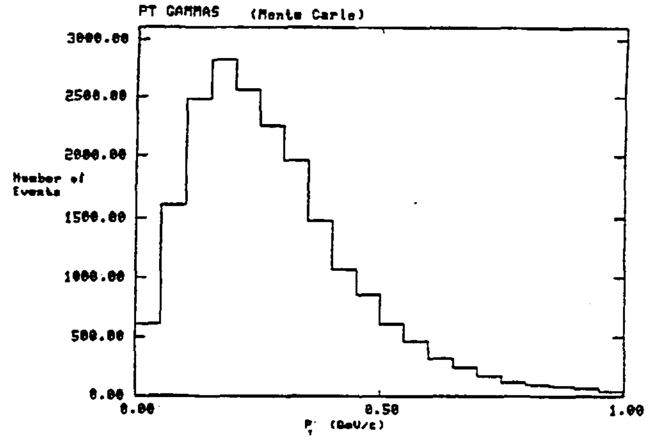

Fig 5.9d

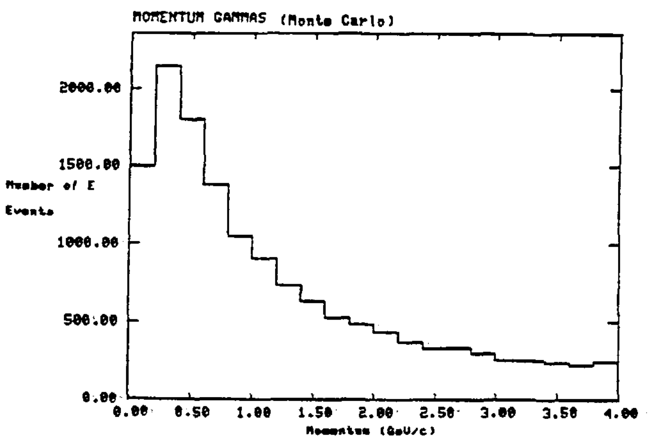

Fig 5.9b

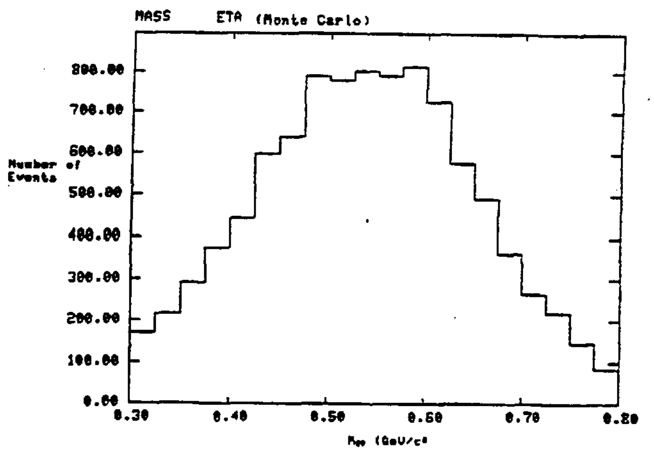

Fig 5.9e

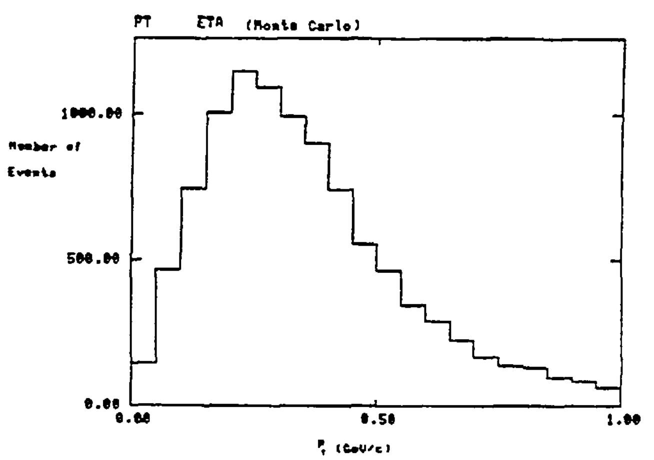

Fig 5.9c

Monte Carlo Plots for eta to gamma-gamma

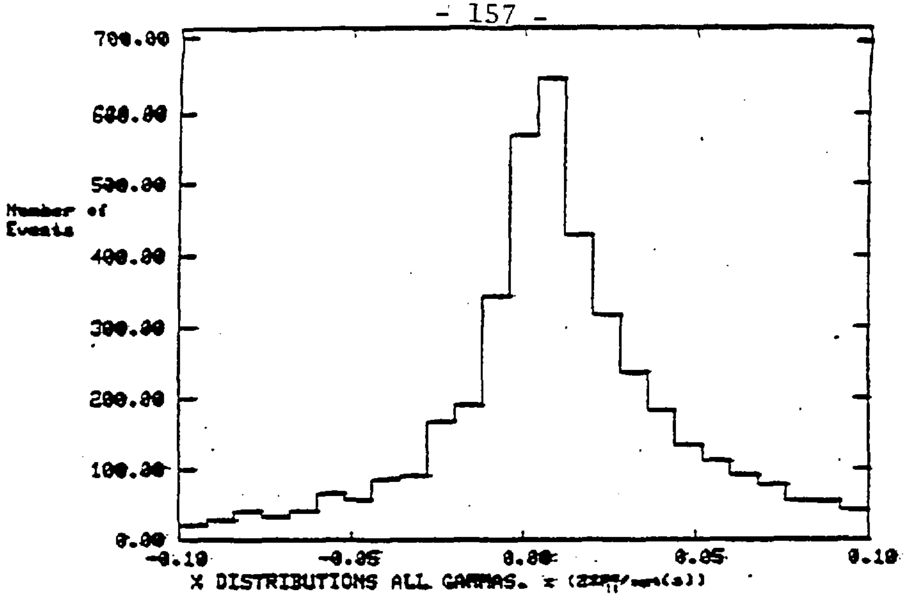

Fig 5.10a

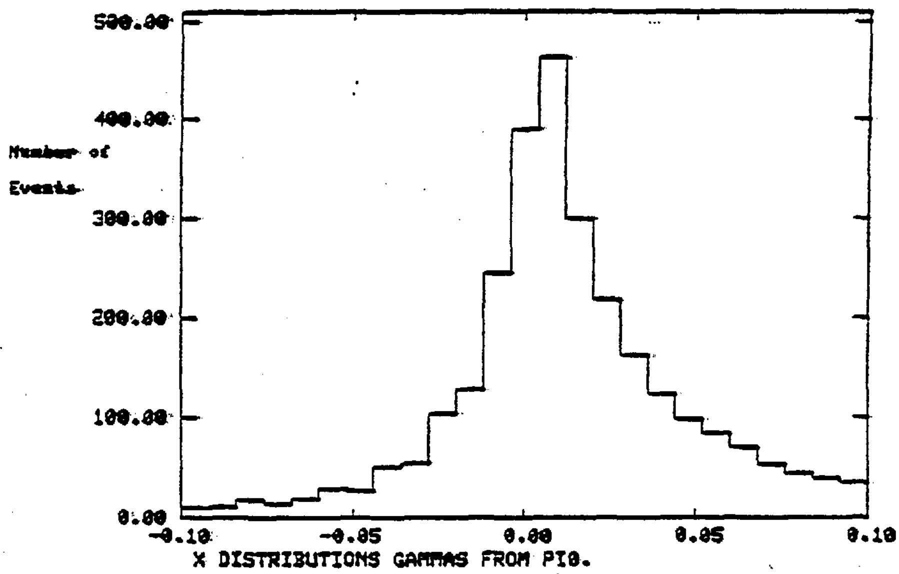

Fig 5.10b

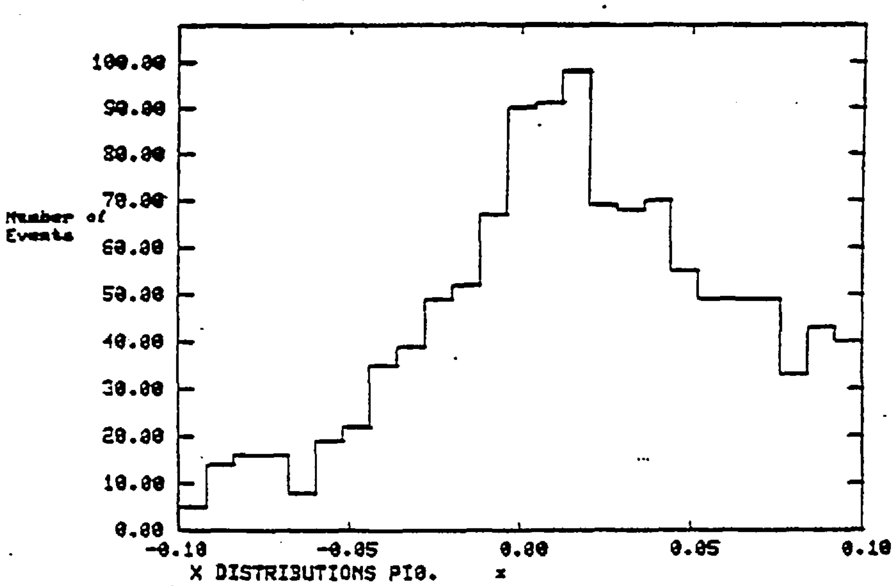

Fig 5.10c

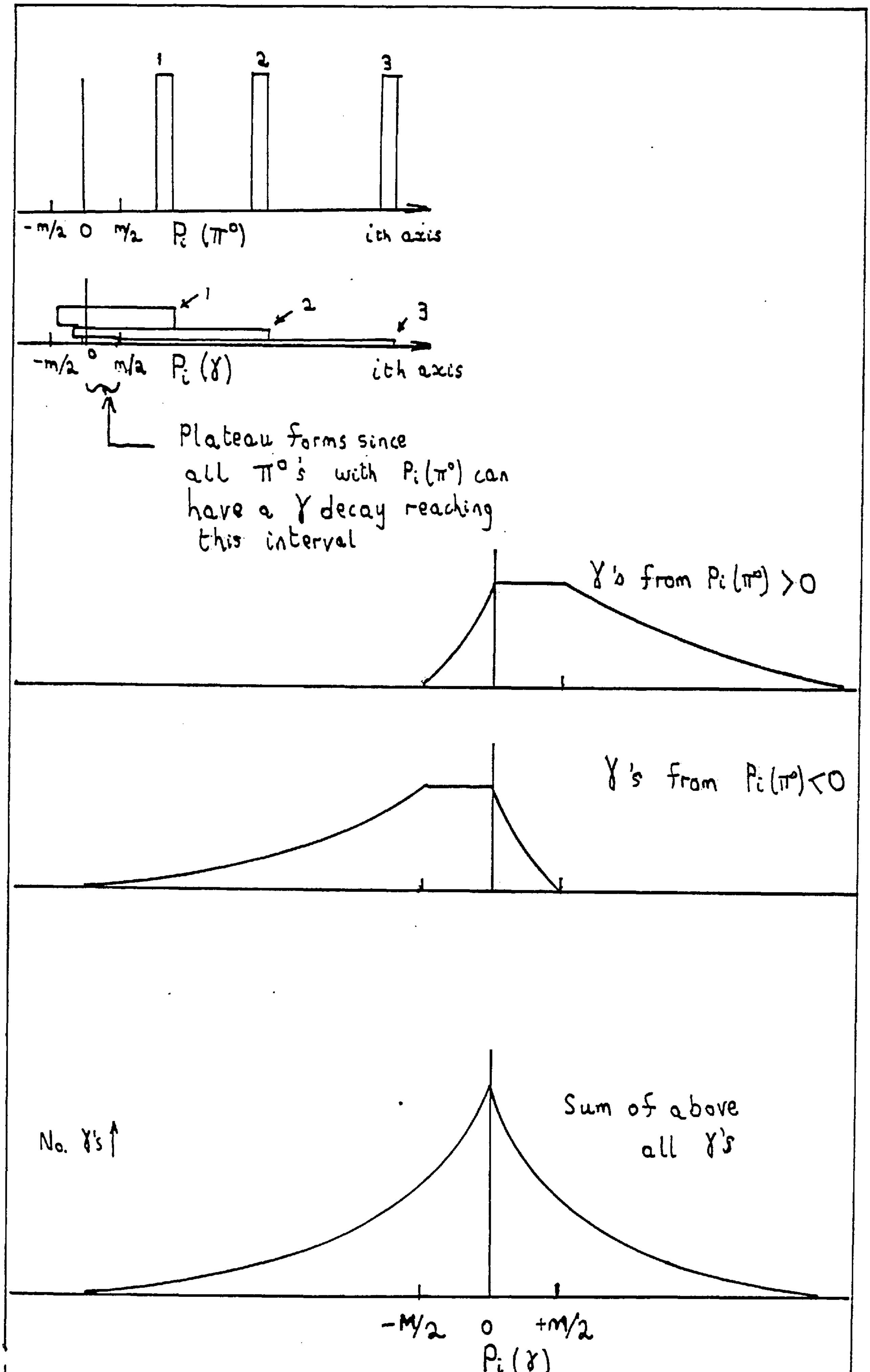

1
2
3
-m/2 0 m/2 $P_i(\pi^0)$ ith axis
1
2
3
-m/2 0 m/2 $P_i(\gamma)$ ith axis
Plateau forms since all π^0's with $P_i(\pi^0)$ can have a γ decay reaching this interval
γ's from $P_i(\pi^0) > 0$
γ's from $P_i(\pi^0) < 0$
Sum of above all γ's
No. γ's
-M/2 0 +M/2
$P_i(\gamma)$

Fig 5.11

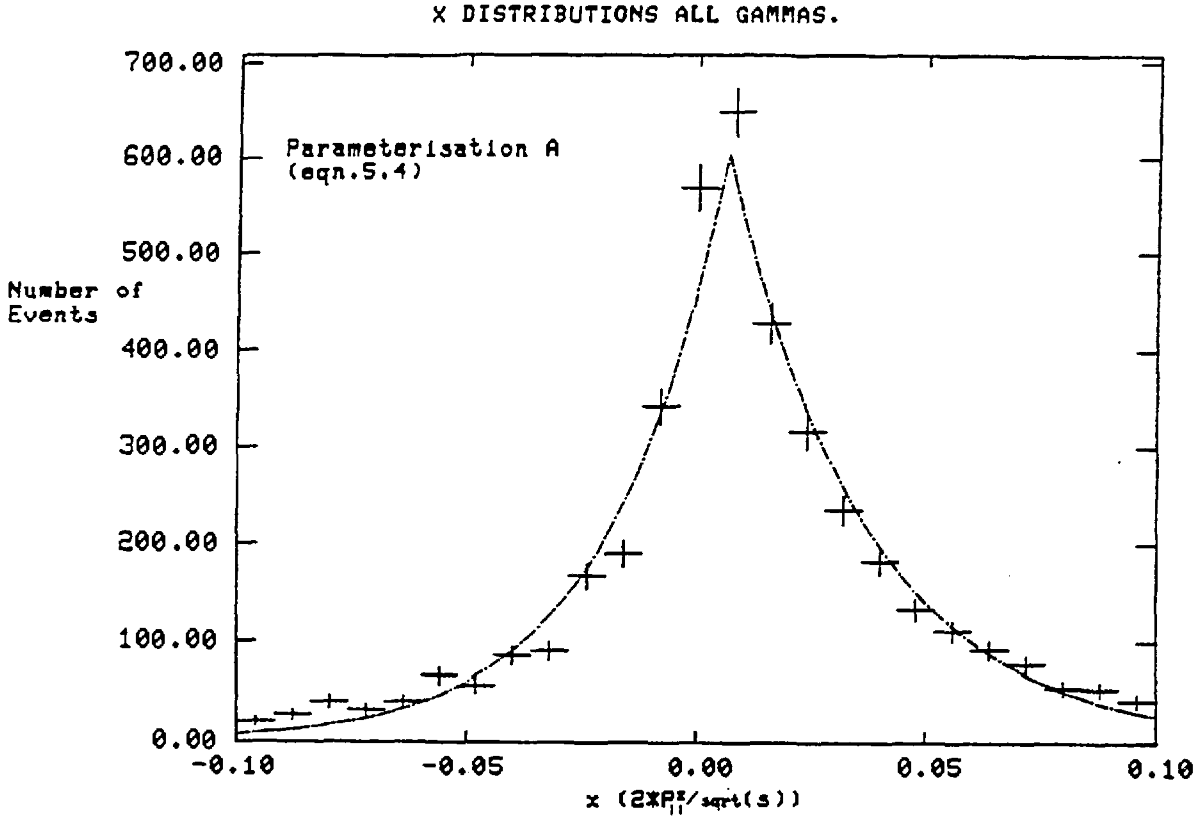

Fig 5.12a

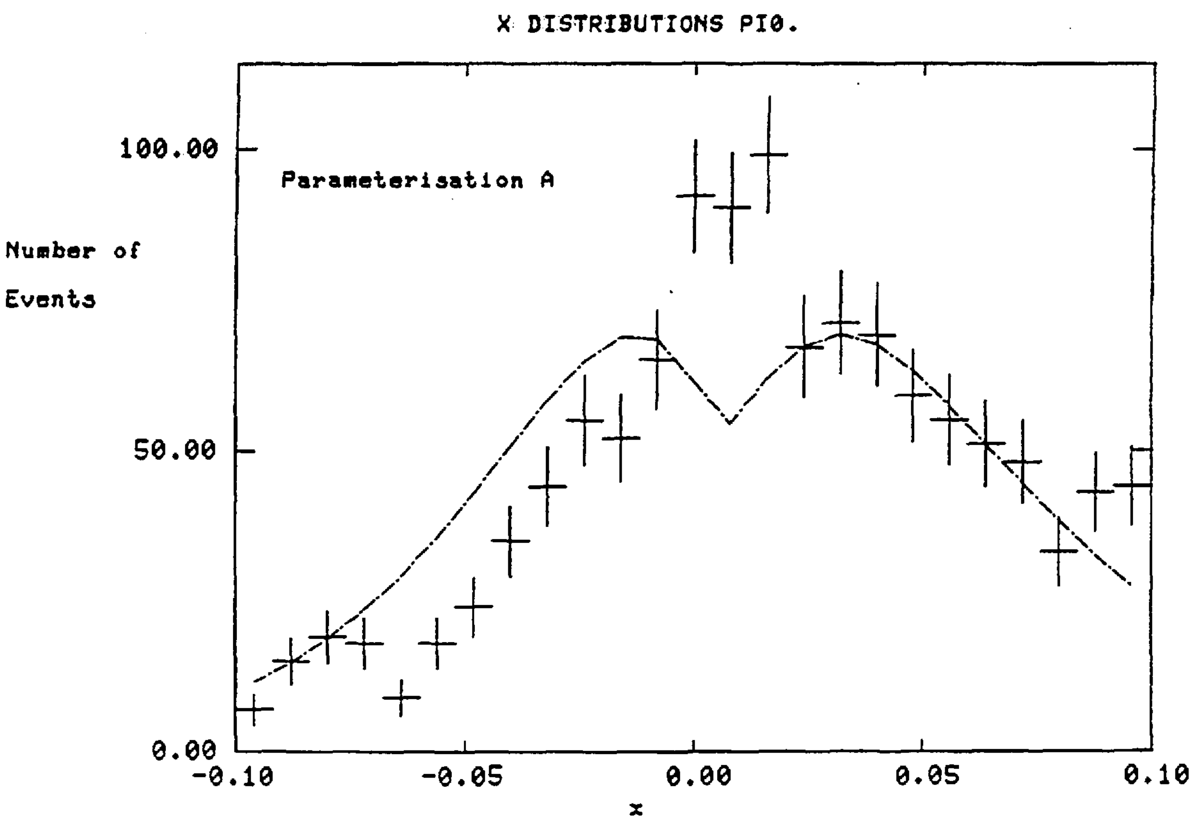

Fig 5.12b

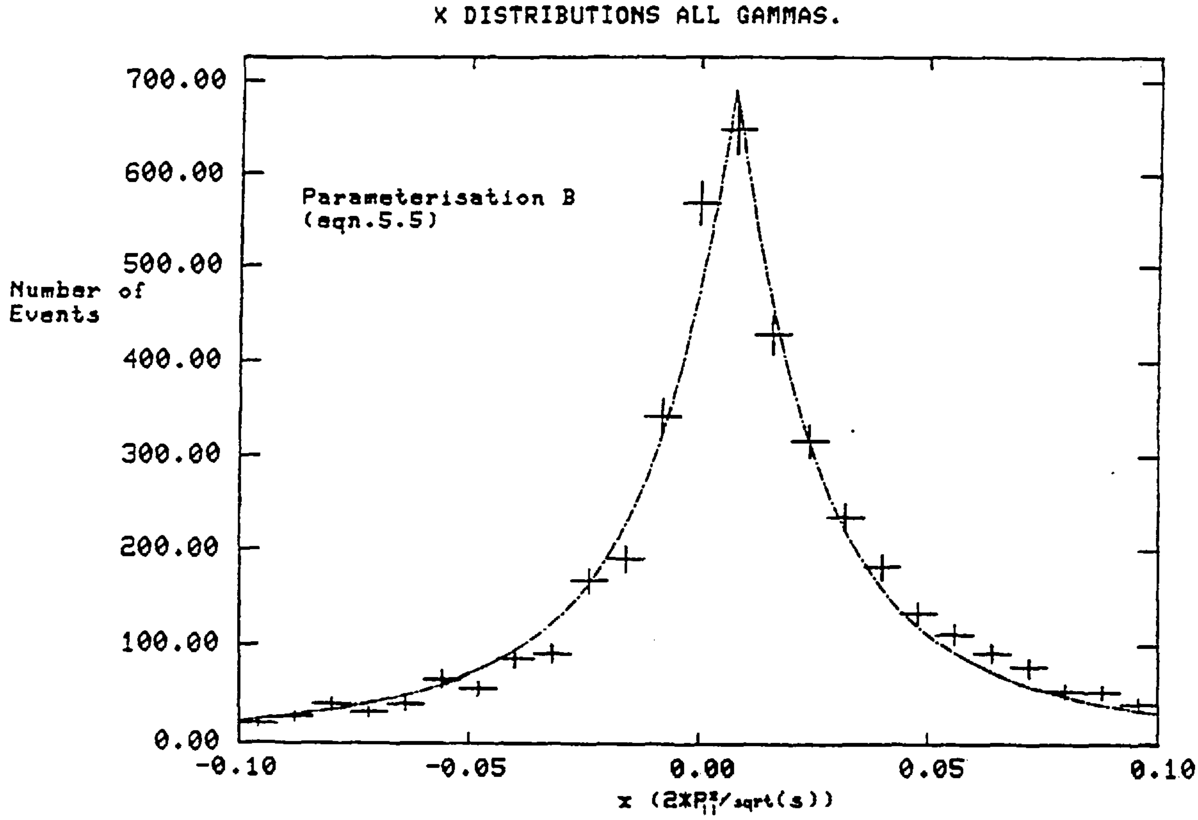

Fig 5.13a

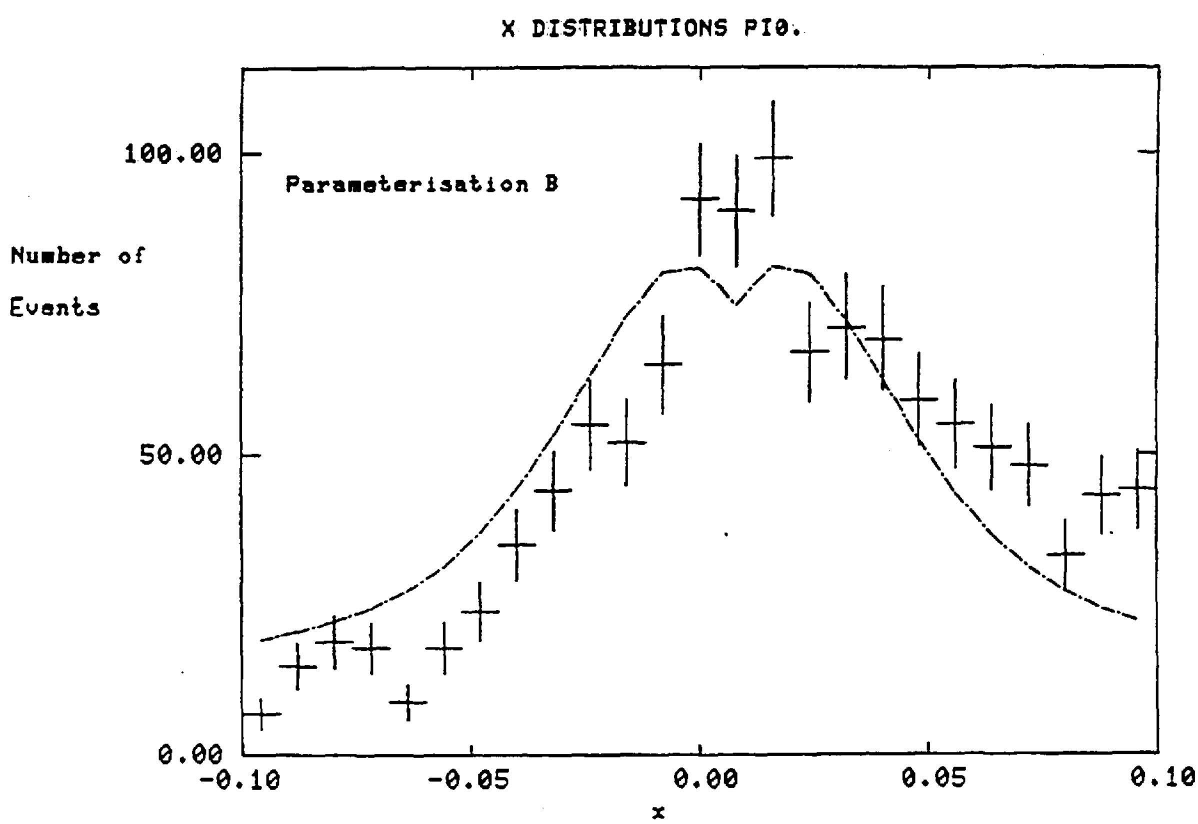

Fig 5.13b

X DISTRIBUTIONS ALL GAMMAS.

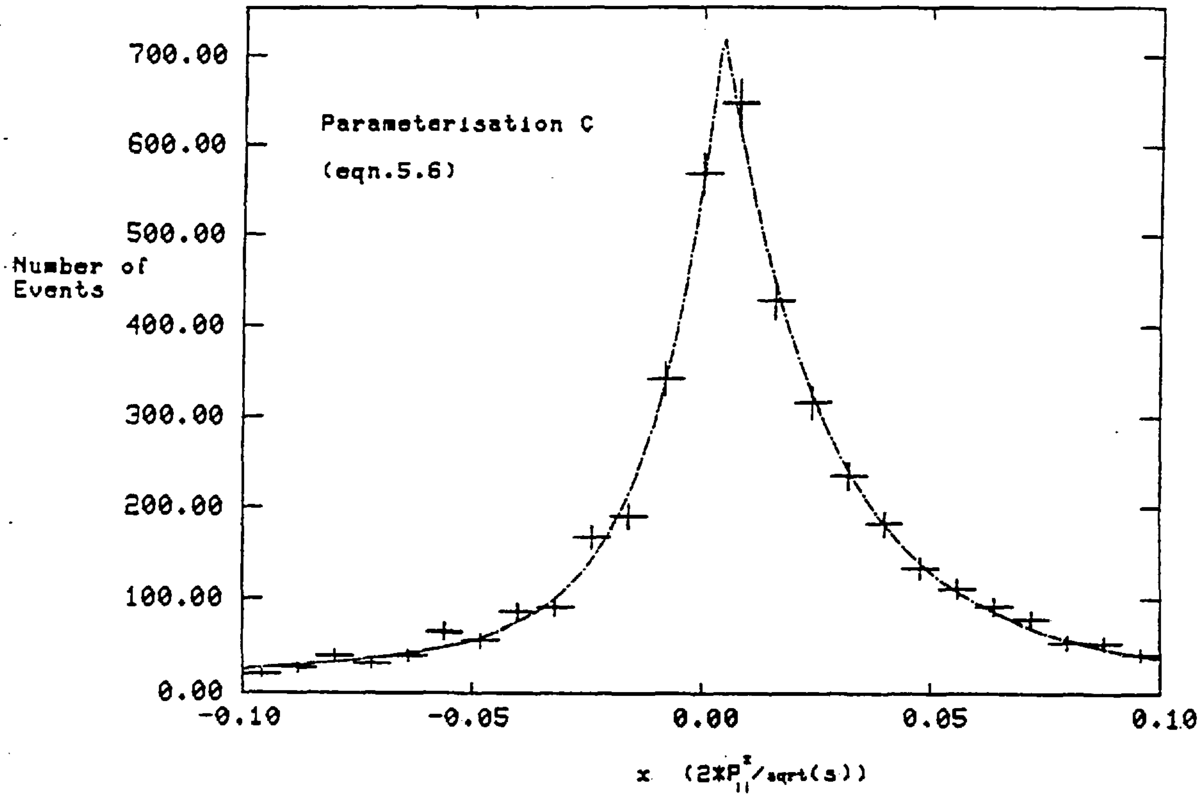

Fig 5.14a

X DISTRIBUTIONS PI0.

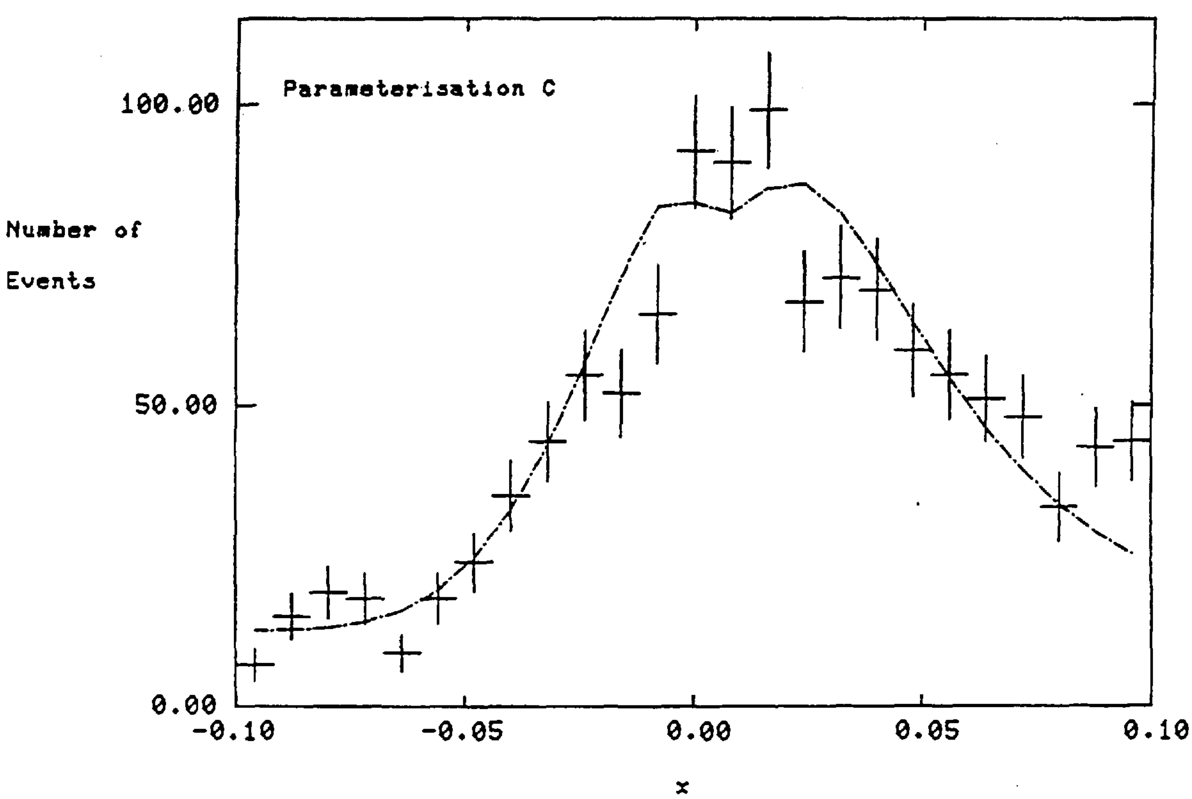

Fig 5.14b

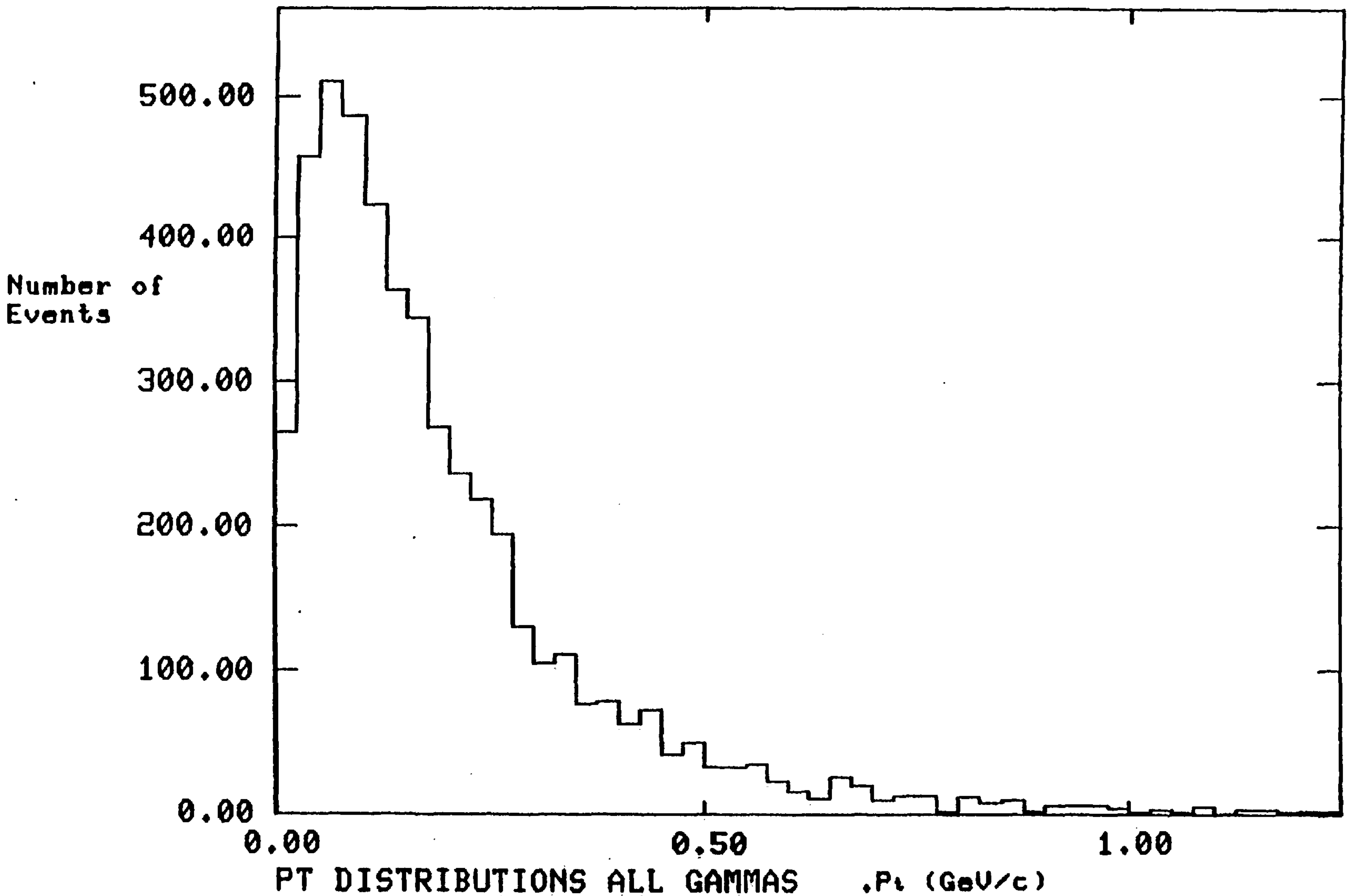
500.00
400.00
300.00
200.00
100.00
0.00
Number of
Events
0.00
0.50
1.00
PT DISTRIBUTIONS ALL GAMMAS
.Pt (GeV/c)

Fig 5.15

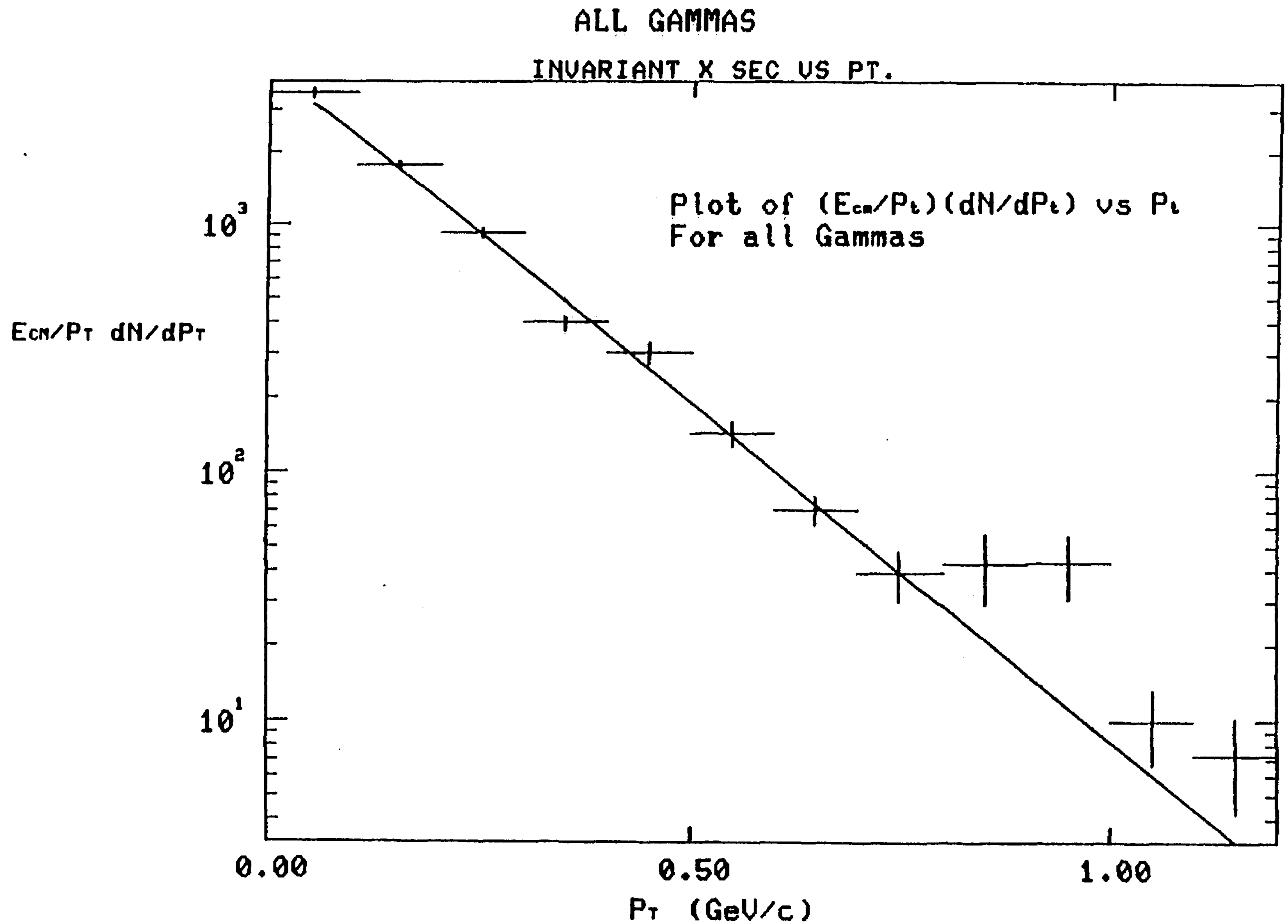

ALL GAMMAS
INVARIANT X SEC VS PT.
Plot of (Ecm/Pt)(dN/dPt) vs Pt
For all Gammas
ECM/PT dN/dPT
10³
10²
10¹
0.00
0.50
1.00
PT (GeV/c)

Fig 5.16

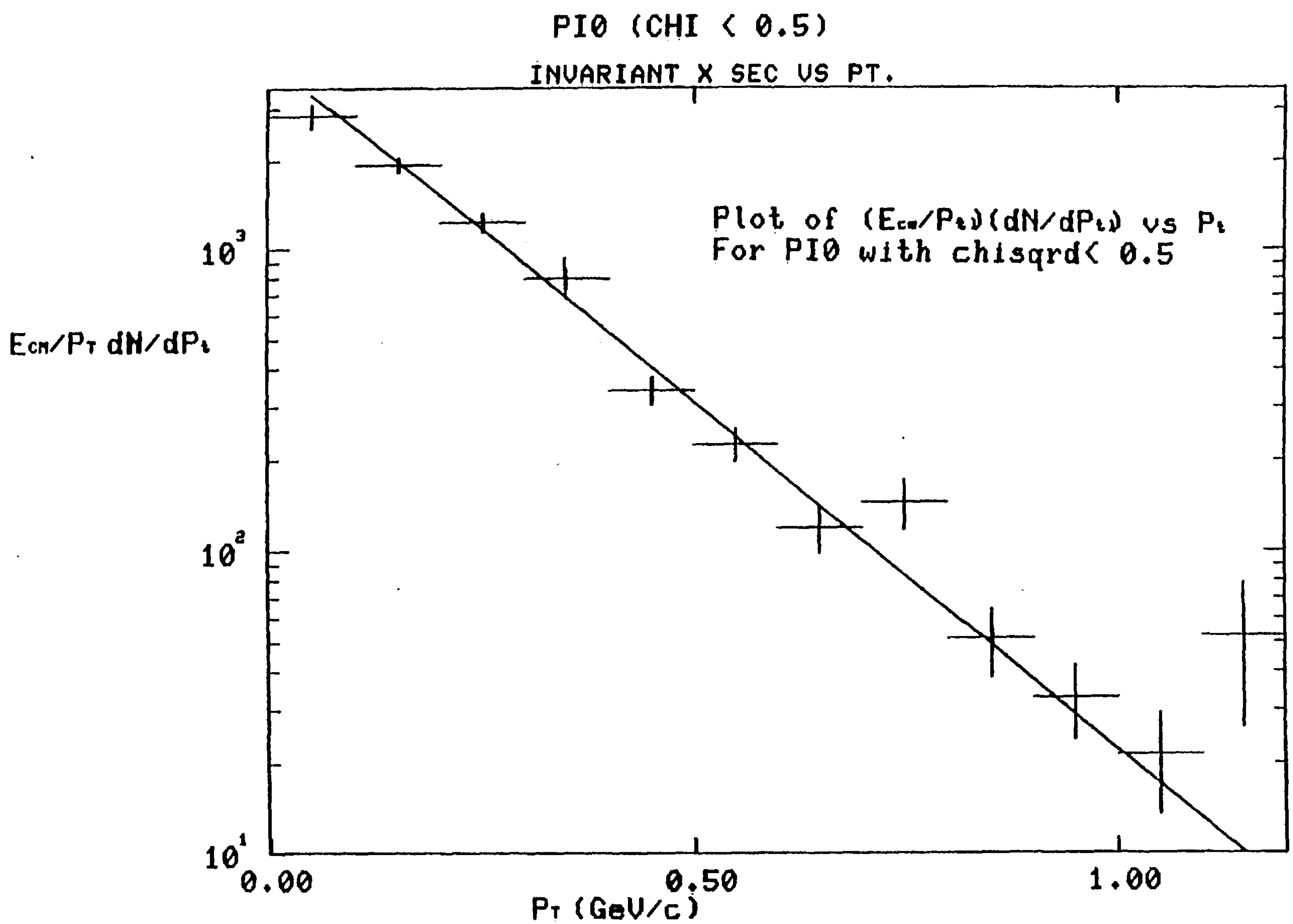

PI0 (CHI < 0.5)
INVARIANT X SEC VS PT.
Plot of (Ecm/Pt)(dN/dPt) vs Pt
For PI0 with chisqrd< 0.5
Ecm/PT dN/dPt
10³
10²
10¹
0.00
0.50
1.00
PT (GeV/c)

Fig 5.17

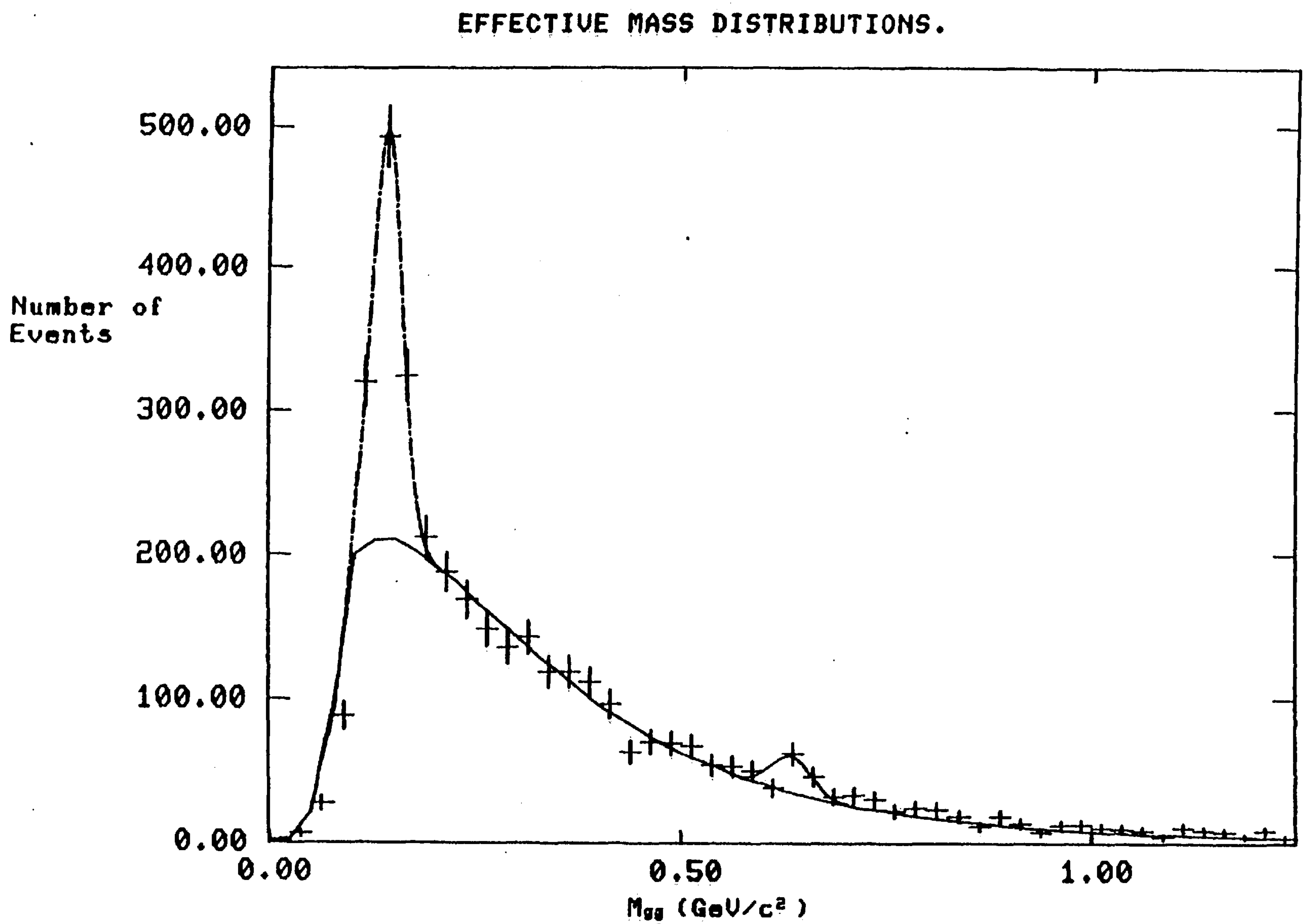
EFFECTIVE MASS DISTRIBUTIONS.
500.00
400.00
300.00
200.00
100.00
0.00
Number of Events
0.00
0.50
1.00
Mgg (GeV/c²)

Fig 5.18

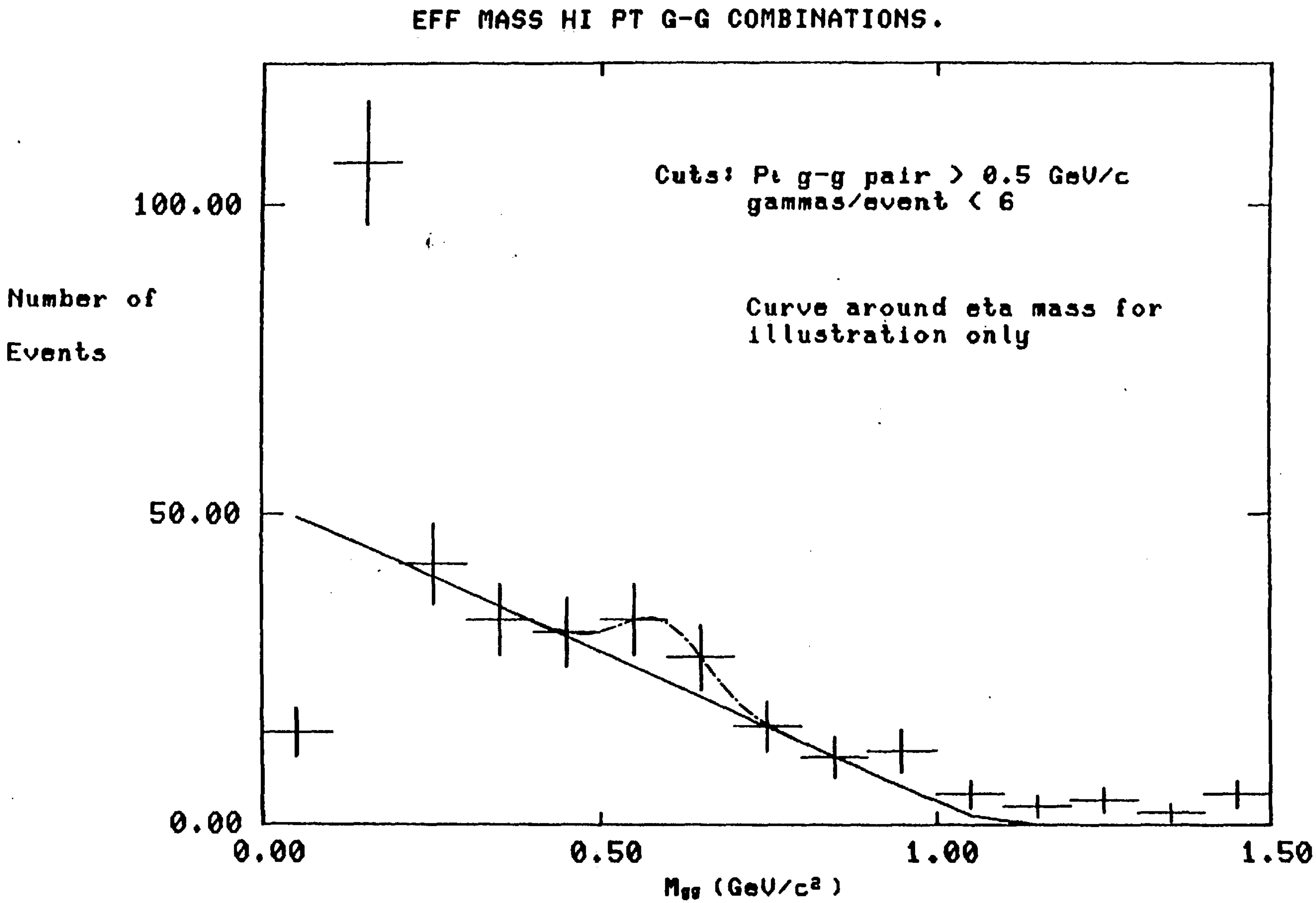
EFF MASS HI PT G-G COMBINATIONS.
Cuts: Pt g-g pair > 0.5 GeV/c
gammas/event < 6
Curve around eta mass for illustration only
Number of Events
100.00
50.00
0.00
0.00
0.50
1.00
1.50
Mgg (GeV/c²)

Fig 5.19

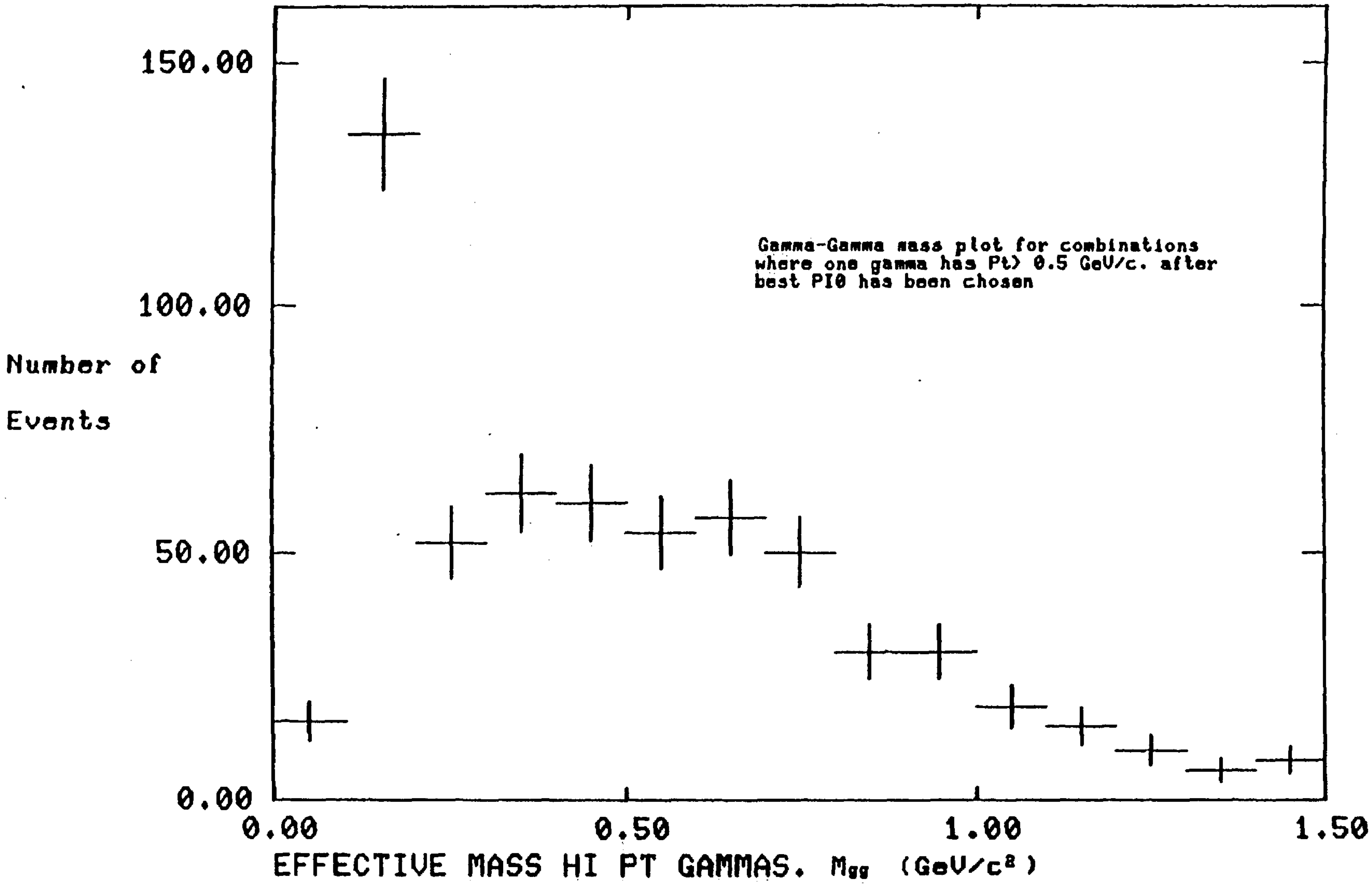
150.00
100.00
50.00
0.00
Number of
Events
Gamma-Gamma mass plot for combinations
where one gamma has Pt> 0.5 GeV/c. after
best PI0 has been chosen
0.00
0.50
1.00
1.50
EFFECTIVE MASS HI PT GAMMAS. Mgg (GeV/c²)

Fig 5.20

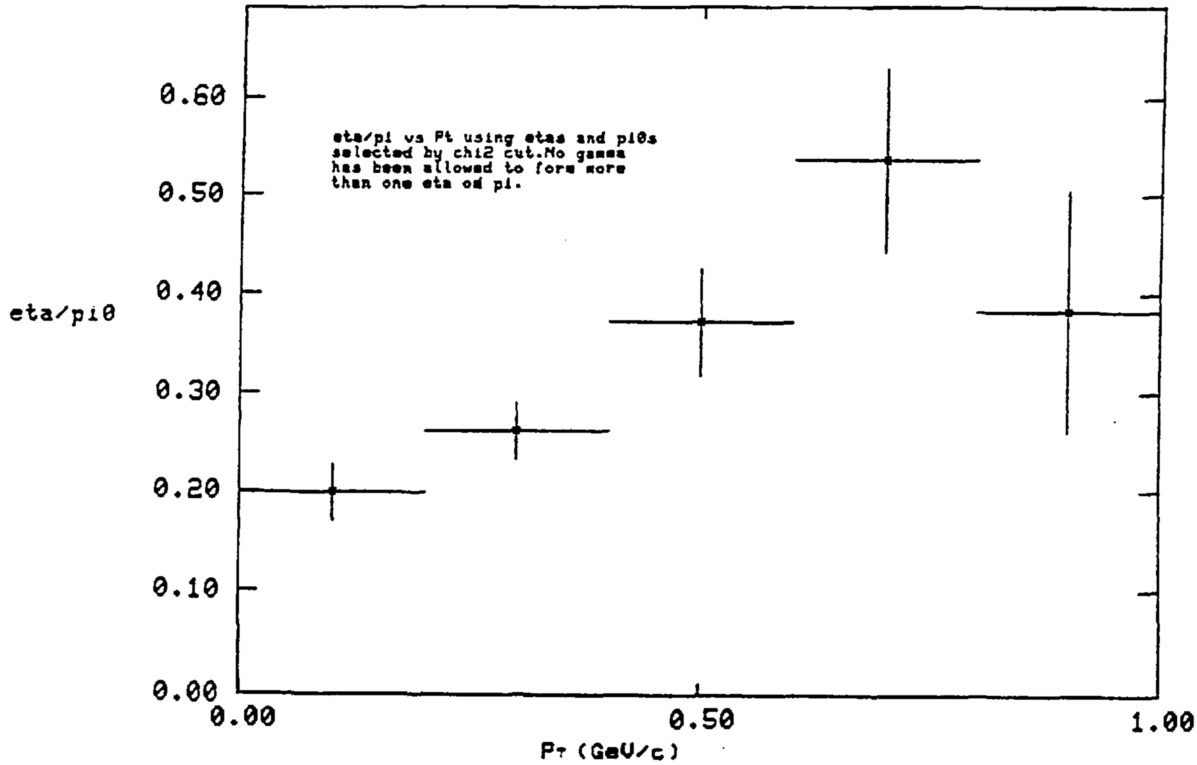

Fig 5.21a

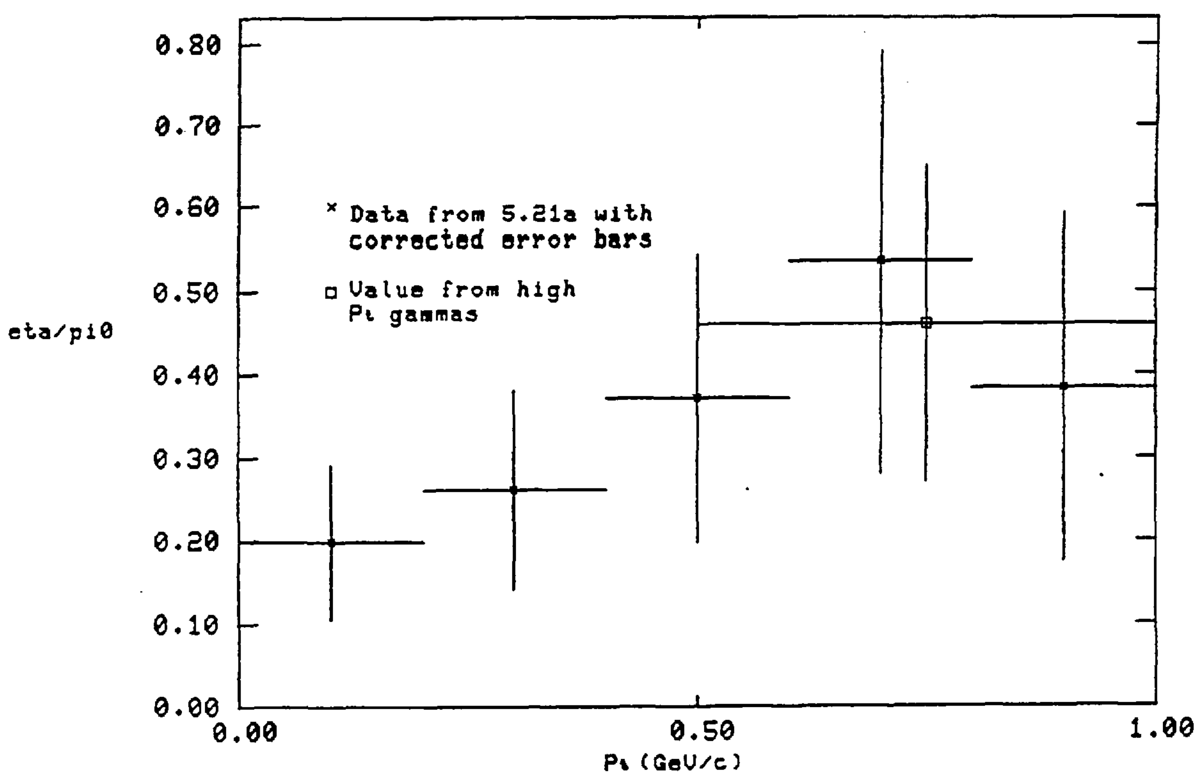

Fig 5.21b

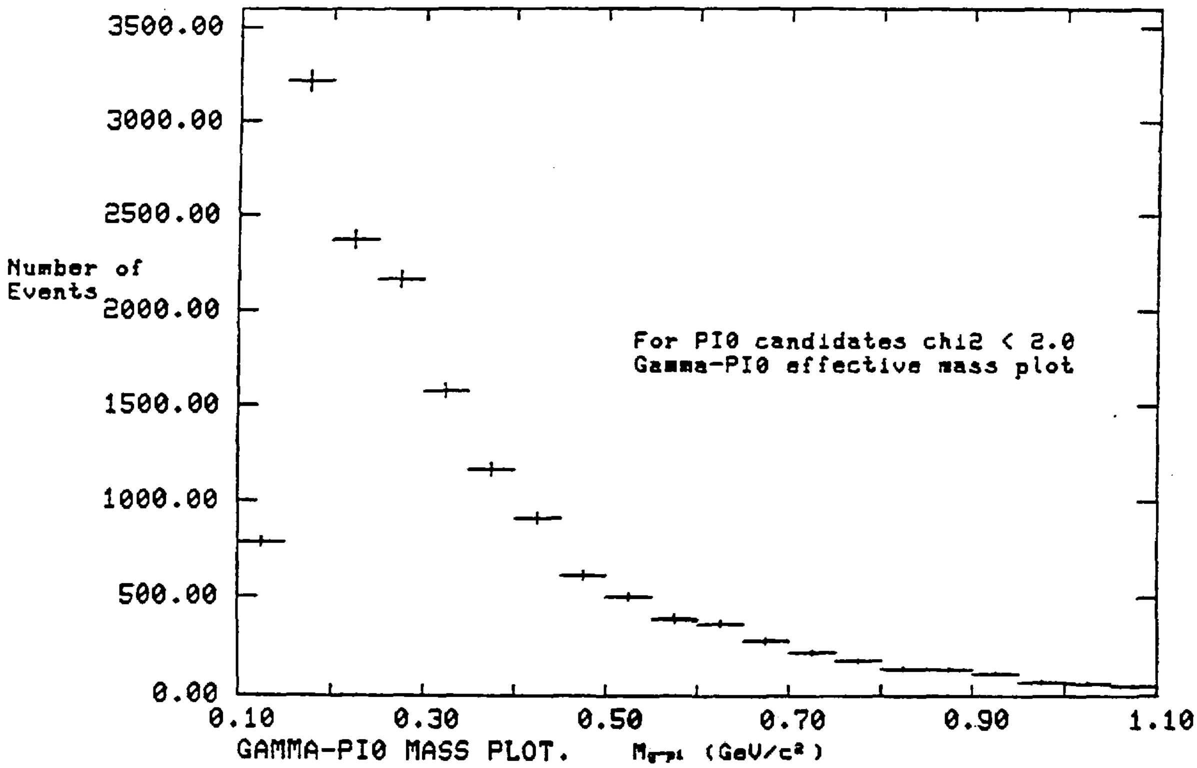

Fig 5.22a

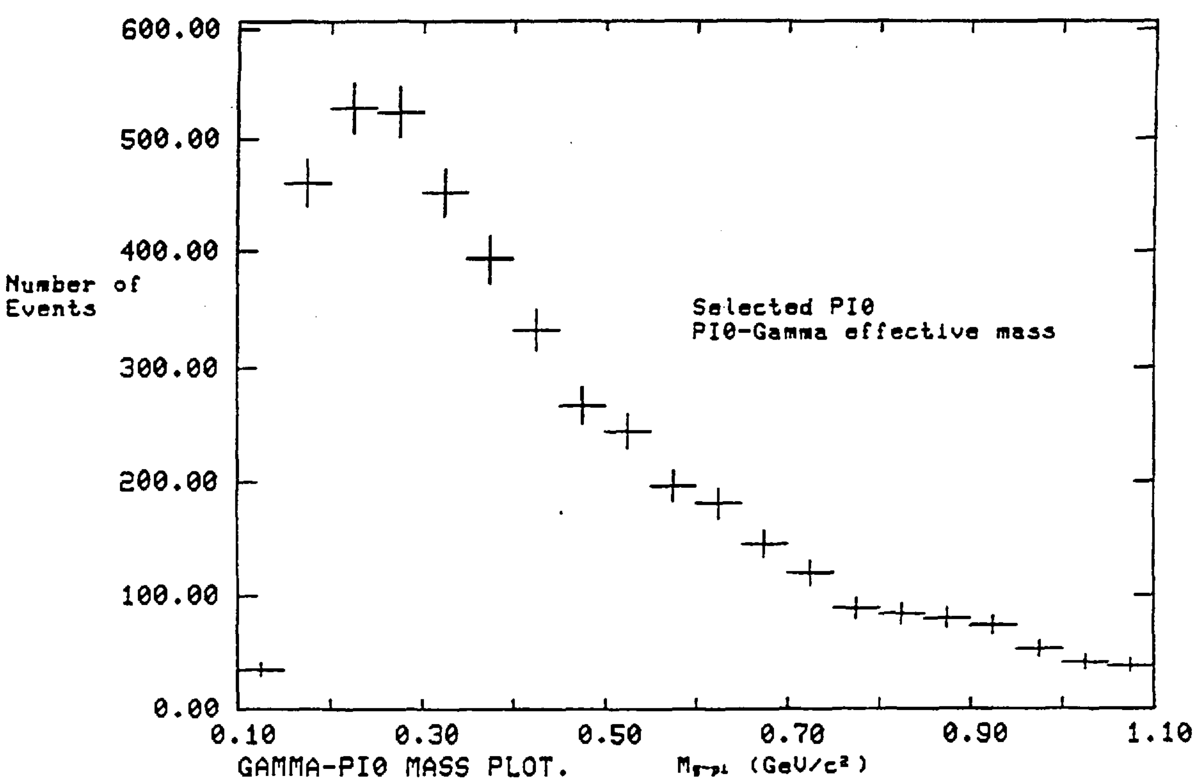

Fig 5.22b

CHAPTER 6

γ/π^o At Low P_T

Introduction

This chapter completes this account of the experiment. γ/π^o in the P_T region 0.5 to 1.0 GeV/c is evaluated.

Firstly, the backgrounds from all conceivable sources of gammas in this P_T range with total cross-section 5% that of the π^o or greater are considered. These, except the gammas from π^o and η, are shown to contribute less than 0.5% of the total number of gammas in this P_T region.

Next the χ^2 cuts for π^o and η are described in more detail and their importance in selecting these particles. Frames with gammas in the high P_T region are then inspected to search for additional photons which could form a π^o or η combination. A calculation is made of the probability for a direct gamma to form a π^o or η on the basis of the χ^2 cut. From this information and the gamma detection efficiency, a crude value for γ/π^o is found using only data from the first measurements.

Those frames with high P_T gammas not associating to a π^o or η are remeasured and combinations attempted.

It is found that all gammas can be paired to a π^o or η. Any unassociated gamma above the number one would expect from a knowledge of the gamma detection efficiency and the probability of forming a wrong combination would have been evidence for directly produced gamma. Using this data, a limit for γ/π^o of 2% can be established.

6.1 Background

In looking for direct photons we must consider the background sources of gammas which might confuse or obliterate the direct photon signal. These are shown in table 6.1.

The π^o and η decay modes are by far the most dominant and have been discussed already. It remains to show that the other processes produce negligible background in the P_T range above 0.5 GeV/c.

6.1.1 Monte-Carlo Calculations

The same Monte-Carlo as used in chapter 5 was used to generate the decays:

$$\Sigma^o \rightarrow \Lambda\gamma$$
$$\omega \rightarrow \pi^o\gamma$$
$$\eta' \rightarrow \rho\gamma$$
and
$$\eta' \rightarrow \gamma\gamma.$$

1000 events for each were generated in this way. For the Σ^o decay, using a Σ^o P_T distribution similar to π^o, no gammas were found with a P_T greater than 250 MeV.

Thus we expect no background in the P_T region above 0.5 GeV/c from this source.

For the decay

$\omega \rightarrow \pi^o\gamma$

we find that 18% of gammas from this source have a P_T > 0.5 GeV/c. If $\omega/\pi^o \sim 30\%$ and the branching ratio for $\omega \rightarrow \pi^o\gamma$ = 8.8%, then approximately 0.2% of all gammas with P_T > 0.5 GeV/c are from this source (i.e. less than 1 gamma in the entire sample).

Thus we can be sure that these two processes $\Sigma^o \rightarrow \Lambda\gamma$ and $\omega \rightarrow \pi^o\gamma$ do not contribute in any significant way to the background above 500 MeV/c P_T. Below 250 MeV/c, however, the Σ^o decay would contribute quite a large background.

For the η' decays: little data is available on η' cross-sections at these energies. For the decay

$\eta' \rightarrow \rho^o\gamma$

we can safely say from Monte-Carlo studies that the number of high P_T gammas is negligible (< 0.1% of those from π^o's), as little phase space is available.

The decay mode

$\eta' \rightarrow \gamma\gamma$

would produce approximately 30% of its gammas in this high P_T range. With a 2% branching ratio then roughly 0.6% of the total number of η' produce high P_T gammas.

If $\eta'/\pi^0 \sim 25\%$. (say) then η' production would contribute less than 0.15% of the back ground.

Hence we can be certain that all these sources summed together (i.e. Σ^0, ω and η') contribute no more than half a percent of the gammas in the P_T range above 0.5 GeV/c. By far the biggest contributors are the $\pi^0 \to \gamma\gamma$ and $\eta \to \gamma\gamma$ decays.

6.1.2 Dalitz Decays

Of the 337 gammas found unpaired, if they had all come from π^0's, then approximately 4 will be unpaired because the other gamma converts internally to give a Dalitz pair. It might be possible to find the Dalitz pairs by scanning and thus remove from the list of potential direct photons. However, of these 4, on average 2 will probably have formed a spurious π^0 or η anyway. Moreover the scanning of these events for Dalitz pairs is difficult as it is very easy to confuse a γ which is close to the vertex for a Dalitz pair, making unambiguous identification very hard. It was thus decided to include this loss in the γ detection efficiency.

6.2 χ^2 cut for π^0 and η

In the P_T range above 0.5 GeV/c, 337 photons in the 1100 events were found. These were thoroughly examined to see if they would combine with another gamma to form a

π^o or an η. A χ^2 cut was applied to each $\gamma\gamma$ mass combination and if the χ^2 for forming a π^o was less than 2.0 then that gamma was associated to a π^o. 158 gammas satisfied this cut. Another 52 satisfied the condition

$$|M_{\gamma\gamma}-M_{\pi}| < 2\Delta M_{\gamma\gamma} + 25 \text{ MeV}$$

(i.e. the mass of the pair fell within 2σ of the range 110 to 160 MeV/c^2) with two or more mass combinations. In these cases the gamma was paired off with the combination of lowest χ^2. This left 117 gammas unpaired. These were looked at by hand to see if they had associated with an η. A stricter method was applied here, as described below, because the proportions of background to signal in the η region is much greater than in the π^o region. If a $\gamma\gamma$ conbination fell in the range 525 to 575 MeV and $\chi^2_\eta < 2.0$ then a definite η association was assigned. Moreover if a gamma formed 2 or more combinations in the range 450 to 650 MeV with a $\chi^2_\eta < 1.0$ then it was taken that one of these combination was probably a real η . This process left 48 unpaired photons. The χ^2 distribution for the selected gamma-gamma combination is shown in fig. 6.1. The χ^2 cut of < 2.0 is reasonable if one considers fig. 6.2, the χ^2 distribution for the best π^o's for all γ. This extends out to χ^2 of 5 but starts to rise at $\chi^2 < 2.0$ indicating that the true π^o's are to be found here. 95% of all real π^o's should be contained in this region.

We must now see how many direct gammas in this high P_T range will satisfy the above cuts with an uncorrelated gamma.

6.2.1 Direct photon forming π^0's or η

Given a number of direct photons, N_1, we wish to know how many would form a π^0 or η combination with uncorrelated photons. This was done by taking photons with a $P_T > 0.5$ GeV/c and combining them with photon from the next frame.

Of the 311 photons used, and applying the same cuts as for the real sample, 111 formed π^0's and 41 formed η's making 152 spurious combinations in all. Thus $(49 \pm 5)\%$ of all direct photons with $P_T > 0.5$ GeV/c would be expected to form a combination with another gamma, compatible with a π^0 or η. This correction must be applied to the limit set on γ/π^0 to take into account the possibility of spurious combinations.

This verifies the number of spurious combinations found by assuming the γ detection / reconstruction efficiency as being around 67%:of 337 high P_T gammas we would expect to find the "other" gamma for 226 of these but in fact find it for 289 of these 337. In other words 63 out of the 101 gammas we would expect not to be paired, have been.

6.3 γ/π^0

Using this information we can now proceed to evaluate γ/π^0. The first method uses only the information available from the first measurements. In the second, frames with unpaired high P_T gamma were remeasured in an attempt to pair off these gammas.

6.3.1 Method 1)

Let:

η = efficiency for any gamma to appear on the DST (includes detection/scanning/reconstruction

$N\gamma$ = Number of gammas from real π^o's or η (unknown)

Nd = Number direct gammas (unknown)

$N\pi$ = Number of gammas fitted to $\pi^o + \eta$ (known)

$N\pi^1$ = Number of real $\pi^o + \eta$

N = Number of gammas (known)

α = Probability of a gamma forming a π^o or η combination with an uncorrelated gamma

$N\gamma$, N and N all refer to gamma with P_T 0.5 GeV/c.

Now

$$N = N\gamma + Nd$$

$$N\pi^1 = \eta N\gamma$$

$$\begin{aligned} N\pi &= N\pi^1 + \alpha\,(N - N\pi^1) \\ &= N\gamma\,(\alpha + \eta(1-\alpha)) + \alpha Nd \\ &= (N-Nd)\,(\alpha+\eta(1-\alpha)) + \alpha Nd \end{aligned}$$

$$N\pi - N(\alpha + \eta(1-\alpha)) = Nd\ \eta(1-\alpha)$$

$$Nd = \frac{N\pi - N(\alpha + \eta(1-\alpha))}{\eta(1-\alpha)} \qquad 6.1$$

If $M\pi$ = Number of π^0 with $P_T > 0.5$ GeV/C then number expected = $\frac{M\pi}{\eta^2}$

$$\frac{\gamma}{\pi^0} = \frac{Nd\eta^2}{M\pi}$$

$$= \frac{\eta(N\pi - N(\alpha + \eta(1 - \alpha))}{M\pi(1 - \alpha)} \qquad 6.2$$

$N\pi = 289 \pm 17$

$N = 337 \pm 18$

$M\pi = 340 \pm 18$ (the number of π^0 combination with $P_T > 0.5$ GeV/c and confirmed using Parent-Child relation)

$\alpha = 0.49 \pm 0.05$

$\eta = 0.67 \pm 0.022$

$\therefore \frac{\gamma}{\pi^0} = (3.34 \pm 14)\%$

Using Method 1

$\frac{\gamma}{\pi^0} = (3.3 \pm 14)\%$

Clearly the error on this ratio, calculated from the first round of scanning and measurement, is too large to set useful upper limits on the ratio. Moreover, the calculation is particularly sensitive to the value of η. Should the number of direct photons be assumed to be zero, equation 6.1 can be used to calculate the value of η. In this case, η becomes 72%.

Method 1 shows, however, that γ/π^0 is small and consistent with zero, but that low statistics prevent a good limit being imposed.

6.3.2 Remeasurements

Of the 48 high P_T gammas found which did not, on the first measure, appear to be from the decays of π^o's or η's, it was decided to remeasure 30. These 30 were those worst case events where no possible association could be found. All the 48 were looked at by hand, examining all mass combinations to see if there were any associations, even with a gamma rejected by the bremsstrahlung cut.

6.3.3 Online π^o reconstruction

For the remeasurements, the high P_T gamma was measured first of all and its track parameters stored. A minor problem was to retain this information should the PDP10 crash. This was done by writing this information to a disc file as soon as this gamma has been measured. Whenever the measuring program is restarted, this file is read and the information restored.

All gammas measured subsequently are then combined with this gamma to form an effective mass, $M\gamma\gamma$ with error $\Delta M\gamma\gamma$. The χ^2's are then calculated:

$$\chi^2_\pi = (M\pi - M\gamma\gamma)^2 / (\Delta M\gamma\gamma^2 + \sigma^2)$$

and $$\chi^2_\eta = (M\eta - M\gamma\gamma)^2 / (\Delta M_{\gamma\gamma}{}^2 + \sigma^2)$$

where σ = 20 MeV

Should the following conditions be satisfied, the measurer is told to proceed to the next event :

if $\chi^2_\pi < 1.0$ this combination is a definite π^o

or should 3 combinations with $\chi^2_\pi < 2.0$, be found one of them is probably a π^o.

if $\chi^2_\eta < 0.2$ this combination is an η

or 3 combinations with $\chi^2_\eta < 1.0$

The limits are much stricter for the η than the π^o because the background under the η is much higher than the η signal itself, therefore background combinations are more likely to be accepted, should the η and π^o limits be the same.

6.3.4 Method 2

One problem is what happens when the high P_T gamma fails at the remeasure stage :

The measurer is told to continue measuring all gammas on the frame. The result of this procedure is to effectively increase the reconstruction/scanning efficiency (η in equation 6.1). Should any gamma fail on the remeasure, but have passed on the first measure, then the first measure parameters for the gamma are used and vice versa. η thus becomes of the order 90%.

Of the 30 high P_T events remeasured, all could be associated with another gamma to form a π^o or η (see table 6.2). From equation 6.1, we can calculate the number of direct gammas we expect to see in this sample given that

$$\eta = 0.89 \pm .044$$

$$\alpha = 0.49 = 0.05$$

$$N\pi = N = 30$$

From equation 6.1, if $N\pi = N$ then the value of α cancels. This is expected, as if $N\pi = N$, then α must tend to equal 1. Hence by forming every high P_T gamma to combine to a π^o or η, then the sample of direct photons tends to the upper limit of :

$$Nd = \frac{N\ (1-\eta)}{\eta}$$

η approaches a value around 90% on the second measure and subsequent remeasures would not increase it much beyond this. For producing a good upper limit, $\eta = 0.9$ serves very well.

$Nd = 3.7 \pm 3.2$

$N = 3.7 \pm 3.2$ in 30 measure for 48 unpaired

high P_T gamma $N = 6 \pm 5.3$

Taking into account spurious combinations

(a factor α)

12 ± 12

$$\frac{\gamma}{\pi^o} = \frac{12 \pm 12}{M\pi}$$

$$M\pi = 340/0.69 = 507$$

$$\frac{\gamma}{\pi^o} = (2.4 \pm 2.6)\%$$

Should other possible sources of high P_T gamma be accounted for (0.5%) this became

$$\frac{\gamma}{\pi^o} = (2^{+3}_{-2.1})\%$$

6.3.5 $P_T > 0.8$ GeV/c

Looking at the P_T range above 0.8 GeV/c we see that all 6 gamma in this P_T range which did not associate on the first measure do so on the remeasure.

From eqn (6.1)

Nd = 0.7 ± 1

in 30

=> 1.2 in 48

=> 2.4 $\pm^{3.2}$ after compensating for spurious combinations.

There are 75 π^0 with P_T > 0.8 GeV/c

$$=> \frac{\gamma}{\pi^0} = (2.1 \pm 2.8)\%$$

At the 95% confidence level, then $\gamma/\pi^0 < 7.5\%$ in the P_T range 0.5 to 1 GeV/c.

6.4 Implications of Result

We have found that in the region 0.5 GeV/c P_T to 1.0 GeV/c, the γ/π^0 ratio is 2.1 +/- 2.8% - i.e. consistent with zero, with the statistical accuracy of the experiment. The implications of this result are discussed below.

1. The result is not in disagreement with the Farrar-Frautschi model which states that γ/π^0 is of order 3% at low P_T.

2. This result is clearly inconsistent with the 10 to 15% γ/π^0 at low P_T postulated to explain the high e/π of the CHORMN result from the ISR. If this result is confirmed then some other process (e.g. charm production) is required to explain this anomaly. On the other hand there may be a threshold effect involved such that at ISR energies γ/π^0 is high at low P_T.

Several hypotheses may be stated

1) γ/π^o in this P_T region is effectively zero.

This may be due to :

a) too low a centre of mass energy, i.e. there is a threshold of $\sqrt{s}$ > 12 - 15 GeV below which γ/π^o is zero.

b) γ/π^o is zero for p - N interaction. Other beam particles might produce a large γ/π^o.

c) γ/π^o is zero in this P_T range over the entire range of s currently available.

2) γ/π^o is of order 2% in this P_T range.

This would be consistent with Farrar-Frautschi and with the data.

3) γ/π^o is greater than 5% but less than 10%. In this case we should have found 10 to 20 clear direct gammas after remeasures, and we did not.

This would still not be high enough to explain the direct lepton anomaly. This is at the upper limit set by this experiment and this hypothesis can be rejected.

This data cannot distinguish between hypotheses 1) and 2) with the available statistics. In order to do so would require something like four times the number of events available.

Taking in all the available γ/π^o data

1c) looks to be the most likely conclusion to draw namely that over the entire s range γ/π^o is close to zero at low P_T.

1b) would require runs with other beam particles and 1a) several runs at various energies.

2) would require a high statistics experiment.

The proposal for this experiment suggested that should a definite signal be observed then other experiments should be run to test beam particle and energy dependence.

The experience of this experiment suggests it was performed near the upper limit of beam energy at which a useful result can be obtained in a bubble chamber. Whilst differing beam particles (π, $\bar{p}$, K) might reveal a higher and detectable γ/π^0 by these method at this energy, there is no case for taking more p - N data at higher energies using BEBC, considering :-

1) the result is a restrictive upper limit. Most gammas may be paired off with another and those that cannot, may be attributed to other factors.

2) After considerations of the systematic problems of this type of experiment, namely the combinatorial problems, backgrounds, measurement errors, bremsstrahlung the author feels that a heavy liquid bubble chamber, in common with other available techniques, has severe limitations for searching for direct photons.

A hydrogen bubble chamber would be far from ideal, for instance, even with unlimited statistics due to the very large conversion length and energy dependence of this length. The gamma detection efficiency needs to be known with an accuracy not achievable with a hydrogen bubble chamber.

An ideal experiment would require :

1) Good energy resolution.
2) Good spatial resolution.
3) Near 4π coverage.
4) Good conversion efficiency.

In a Ne/H_2 chamber we can satisfy conditions 2), 3) and 4). Whilst the γ energy resolution of this experiment cannot be considered poor, other systems afford better energy definition. Lead-glass detectors satisfy 1) and 4) but, in general, not 2) or 3). A hydrogen chamber satisfies 1), 2) and 3) but the bad, and non-uniform, conversion efficiency suggests that direct photon searches would be impracticable. At low P_T, therefore we must conclude that a Ne/H_2 bubble chamber is the detector most suited to a direct photon search at these energies.

Precise optimisation of the Ne/H_2 mixture was not attempted for the experiment but the author believes that a different, probably lighter, Ne/H_2 mix would have yielded a more precise measurement of the γ/π^0 ratio. In determining the optimum mix, consideration must be taken of :

1) γ conversion length, ($\lambda \propto {}^1/\text{density}$)
2) momentum resolution ($\Delta p/p \propto$ density)
3) bremsstrahlung (number brems $\propto$ density)
4) combinatorial background (number γ's $\propto$ density)

To compensate for a longer conversion length, the fiducial volume could be made smaller.

In this sense this experiment did not achieve its objective : namely to set a good limit on γ/π^{o} to decide whether more data should be taken. However, its success lies in the fact that, despite overwhelmimg systematic problems, a reasonable, consistent value of γ/π^{o} was obtained in a P_T region previously unexplored which convincingly reject the hypothesis that a large γ/π^{o} is responsible for observed direct lepton excess at low P_T.

CHAPTER 6

Figure Captions

Table Captions

TABLE 6.1

Source of Gammas likely to produce substantial background at high P_T.

Decay	Branching ratio	Approx Cross-section
$\pi^o \to \gamma\gamma$ $\to e^+e^-\gamma$	99% ∿1%	112 mb
$\eta \to \gamma\gamma$	38%	∿45 mb
$\Sigma^o \to \Lambda\gamma$	100%	∿ 4 mb
$\omega^o \to \pi^o\gamma$	8.8%	< 30mb ?
$\eta^1 \to \gamma\gamma$ $\eta^1 \to \rho^o\gamma$	2% 30%	< 30mb ?

TABLE 6.2

No Gammas	4832
Hi P_T Gammas	337
Hi P_T associating	$289 \pm {}^{17}_{71}$
Hi P_T Gammas left	$48 \pm {}^{78}_{24}$
Dalitz decays	4 ± 0.2
Hi P_T after remeasure (Nd)	12 ± 12
π^o P_T > 0.5 GeV/c ($M\pi$)	340

$$\frac{\gamma}{\pi^o} = \frac{Nd/\eta}{M\pi/\eta^2}$$

$$= \frac{\eta \, Nd}{M\pi}$$

$$= (2.4 \pm 2.6)\%$$

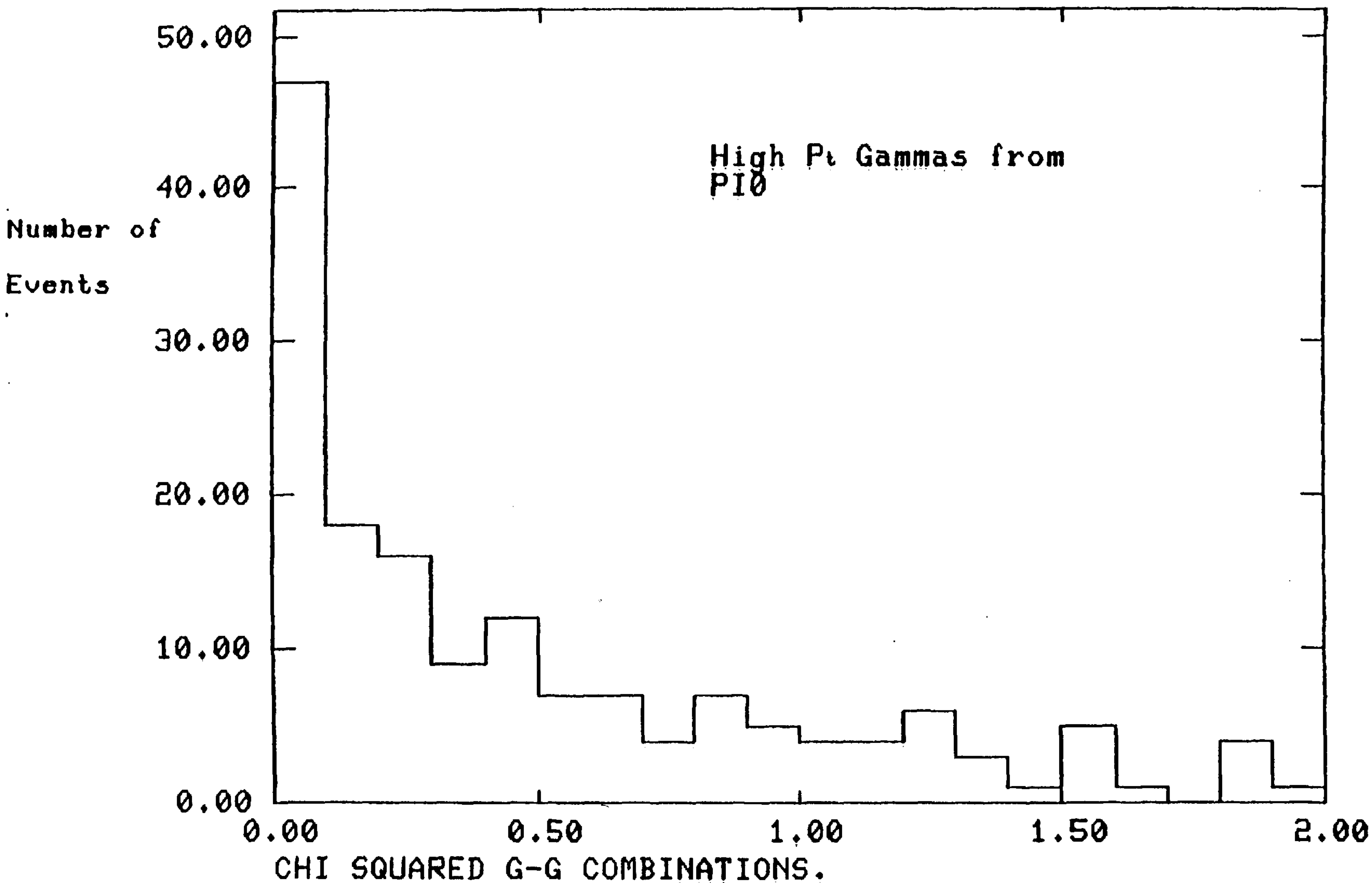

High Pt Gammas from
PI0
Number of
Events
50.00
40.00
30.00
20.00
10.00
0.00
0.00
0.50
1.00
1.50
2.00
CHI SQUARED G-G COMBINATIONS.

Fig 6.1

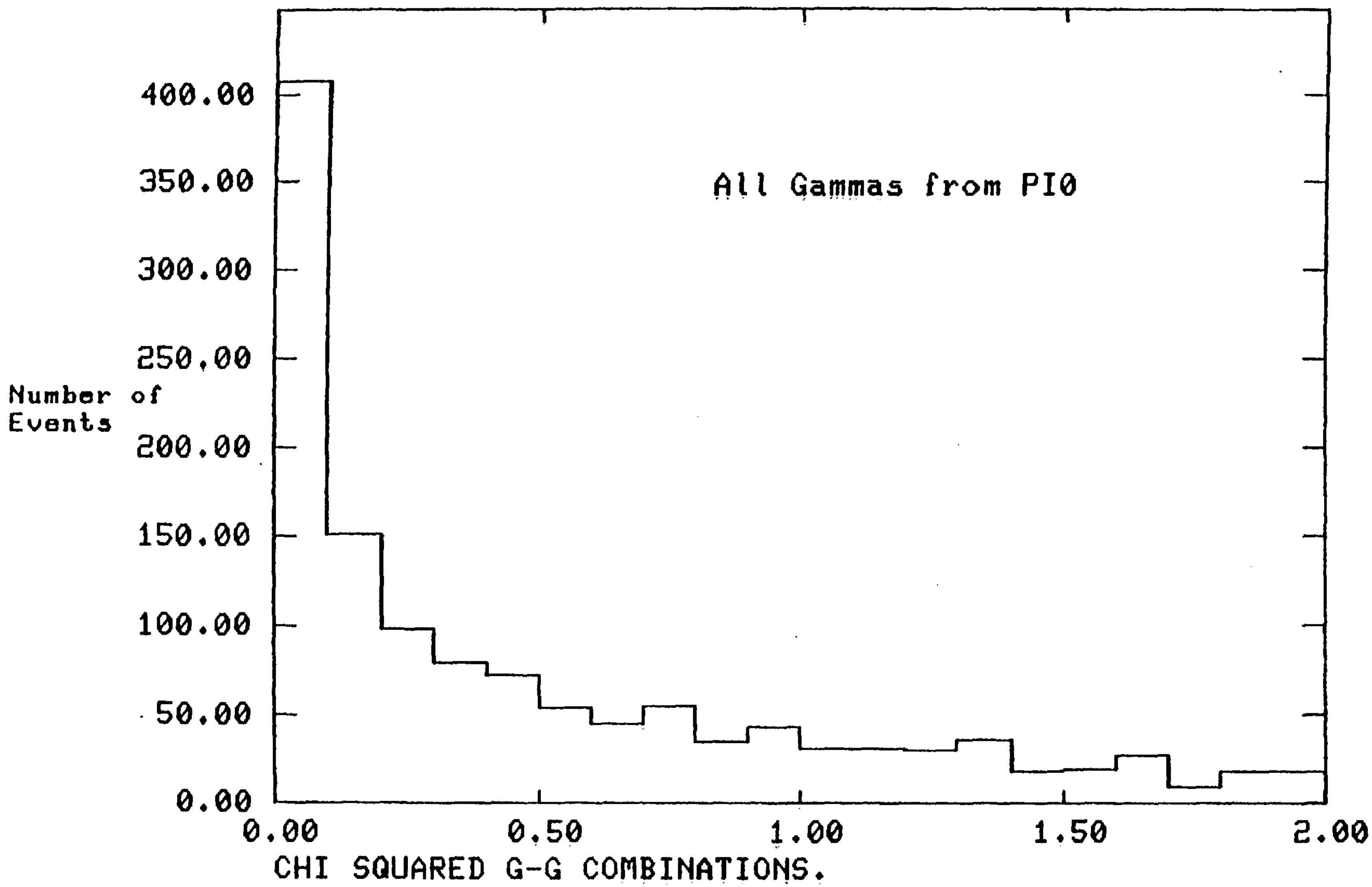
400.00
350.00
300.00
250.00
Number of
Events
200.00
150.00
100.00
50.00
0.00
All Gammas from PI0
0.00
0.50
1.00
1.50
2.00
CHI SQUARED G-G COMBINATIONS.

Fig 6.2

Appendix A

Dimensional counting rules for large P_T reactions. (see e.g. T.C.Bacon "Quarks and Partons" Rutherford Summer School 1977)

Several authors predict that, from field theory, the invariant cross section should depend on:

$$E \frac{d\sigma}{d^3p} \;\alpha\; (P_T^2)^{-N} \, (1-x)^F$$

where N = number of "active" quarks in the subprocess

F = 2 x number of passive quarks - 1.

In figure 1.1a the quarks joining the main interaction "blob" are active whereas the rest are "passive". Hence

$$N = 4 - 2 = 2,$$

$$F = 7,$$

$$E \frac{d\sigma}{d^3p} \;\alpha\; P_T^{-4} \, (1-x)^7.$$

In figure 1.1b

$$N = 6 - 2 = 4,$$

$$F = 2 \times 5 - 1 = 9,$$

$$E \frac{d\sigma}{d^3p} \;\alpha\; P_T^{-8} \, (1-x)^9.$$

Thus the P_T dependence is determined by the complexity of the scattering process.

APPENDIX B

Derivations of π^o Momentum Spectra from Gamma Momentum Spectra and the Parent-Child Relationship.

Consider the two body decay

$A \rightarrow B + C \qquad (\text{e.g. } \pi^o \rightarrow \gamma\gamma)$

In the reference frame of particle A let B have 4 momentum $(\vec{P},E)$. In the absence of spin the vector $\vec{P}$ has an isotropic distribution.

Consider a frame S where A has a 4 velocity $(\vec{\eta},\gamma)$, the Lorentz transformation gives the 4 momentum of B:

$$\vec{P}_s = \vec{P} + \left(\frac{\vec{\eta}\cdot\vec{P}}{\gamma+1} + E\right)\vec{\eta} \qquad (1a)$$

$$E_s = \gamma E + \vec{\eta}\cdot\vec{P} \qquad (1b)$$

The energy distribution of B in frame S (for fixed $\vec{\eta}$) is thus rectangular since E_s is proportional to the cosine of the angle between $\vec{\eta}$ and $\vec{P}$:

$$\rho(E_s|\vec{\eta}|)dE_s = \frac{dE_s}{2|\vec{\eta}|\,|\vec{P}|}$$

$$\gamma E - |\vec{\eta}|\,|\vec{P}| \leqslant E_s \leqslant \gamma E + |\vec{\eta}|\,|\vec{P}| \qquad (2)$$

This is true for the projection of the momentum on any arbitrary direction.

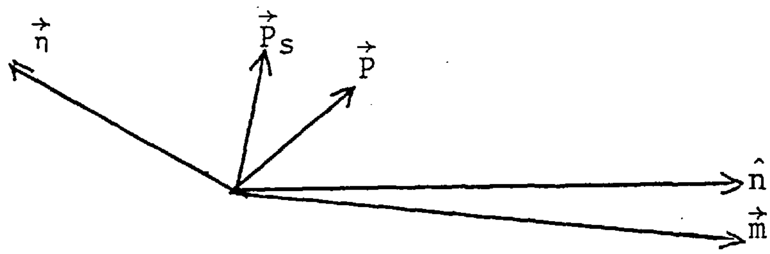

let unit vector $\hat{n}$ define the direction, then if q denote the projection of $\vec{P}_S$ along $\hat{n}$:

$$q = \hat{n}.\vec{P}_S = \hat{n}.\vec{P} + \left(\frac{\vec{\eta}.\vec{P}}{\gamma+1} + E \right) \vec{\eta}.\hat{n} \tag{3}$$

$$= \vec{m}.\vec{P} + \hat{n}.\vec{\eta}E \tag{4}$$

where

$$\vec{m} = \hat{n} + \frac{\vec{\eta}.\hat{n}}{\gamma+1} \vec{\eta}$$

and

$$|\vec{m}| = \left[1 + (\hat{n}.\vec{\eta})^2 \right]^{\frac{1}{2}}$$

For fixed $\vec{\eta}$ the value of q depends only on the cosine of the angle between $\vec{P}$ and $\vec{m}$ in the frame of A, the distribution of q is rectangular:

$$\rho(q|\vec{\eta})\, dq = \frac{dq}{2|\vec{m}|\,|\vec{P}|} \tag{5}$$

$$\hat{n}.\vec{\eta}E - |\vec{m}|\,|\vec{P}| \leqslant q \leqslant \hat{n}.\vec{\eta}E + |\vec{m}|\,|P|$$

The distribution of q depends on $\vec{\eta}$ only through its projection on $\hat{n}$. Also components of $\vec{P}_s$ along different directions are not statistically independent so although we can apply this to three independent directions we do not get the distribution $\vec{P}_s$.

Consider now the case of π^0 decay. The energy and momentum of the photon in the π^0 rest frame are then

$$E = |\vec{P}| = m/2 \qquad \text{where m is the } \pi^0 \text{ mass}$$

(5) thus becomes

$$\rho(q|v) = \frac{1}{(m^2+v^2)^{\frac{1}{2}}}$$

$$\frac{v-(m^2+v^2)^{\frac{1}{2}}}{2} \leqslant q \leqslant \frac{v+(m^2+v^2)^{\frac{1}{2}}}{2} \tag{6}$$

where v is the projection of the π^0 momentum on $\hat{n}$.

Suppose the π^0 momentum component is distributed by some function g(v), then

$$\begin{aligned} f(q) &= \int_{q-m^2/4q}^{\infty} \frac{g(v)\ dv}{(m^2+v^2)^{\frac{1}{2}}} \qquad q > 0 \\ &= \int_{-\infty}^{q-m^2/4q} \frac{g(v)\ dv}{(m^2+v^2)^{\frac{1}{2}}} \qquad q < 0 \end{aligned} \tag{7}$$

Change of variable to $r = q - m^2/4q$ and differentiating with respect to r:

$$g(r) = -\frac{r \pm \sqrt{m^2 + r^2}}{2} \; f'\left(\frac{r \pm \sqrt{m^2 + r^2}}{2}\right) \tag{8}$$

Hence the relation between the photon spectrum f(q) and the parent pion spectrum g(v). For q >> m:

$$g(r) = -rf'(r) \tag{9}$$

similar to the Sternheimer Relation [Phys Rev 99 277 (1955)]

From (2) the distribution of photon energy k for fixed π^0 energy E_π is:

$$\rho(k|E_\pi) = \frac{1}{(E_\pi^2 - m^2)^{\frac{1}{2}}} \tag{10}$$

$$\frac{E_\pi - P_\pi}{2} \leqslant k \leqslant \frac{E_\pi + P_\pi}{2}$$

This leads to

$$h(s) = -\frac{s + (s^2 - m^2)^{\frac{1}{2}}}{2} \; d'\left(\frac{s + (s^2 - m^2)^{\frac{1}{2}}}{2}\right) \tag{11}$$

where h(s) is the π^0 energy spectrum and d(h) the photon energy spectrum.

From (8) and (11) we can work out the π^o longitudal momentum and energy spectra, from the respective gamma spectra.

For the P_T distribution, there is a slight problem: Equation (8) applies directly to any one component of transverse momentum but there are two independent directions transverse to the primary and the distributions are not statistically independent.

The Parent - Child relation for π^o decay is the factor:

$$\alpha = \left[\left(2E_\gamma \frac{d\sigma}{d^3P\sigma}\right) \Big/ \left(2E_\pi \frac{d\sigma}{d^3P_\pi}\right)\right]_{P_{\pi T} = P_{\gamma T}}$$

At large P_T, from equation (9), for an exponential dependence $f(P_T) = e^{-aP_T}$ we can see that

$$\alpha = \frac{f(P_T)}{g(P_T)} = \frac{1}{aP_T}$$

At low P_T though, terms of the order $m_\pi/4P_T^2$ become important:

$$\alpha = \frac{1}{n-1}\, e^{-ax_T/n} \frac{1}{\left[\,1 + m_\pi^2/4P_T^2\,\right]^{n-1}}$$

where n is of order 8.

For $P_T << m_\pi/2$ this value falls very steeply.

from: R.G. Glasser Phys Rev 6D 1993 (1972)

G.I. Kopylov Phys Lett 41B 371 (1972)

N.S. Craigie Physics Report 47 No. 1 (1978)

ACKNOWLEDGEMENTS

I should like to express my thanks and appreciation to the following people :

Professor Ian Butterworth, my supervisor, for providing me with a place in the Imperial College HENP group and for the use of the group facilities.

Dr. T.C. Bacon, the spokesman for this experiment, for his direction and encouragement over the last three years and for reading the drafts for this thesis.

Miss Pat Hurst and all the Imperial College scanners and measurers : my apologies for the eye strain.

Betty Moynihan and the PDP10 computing staff for the help and access given in using this computer

Linda Gold and Linda Jones for their excellent (and patient) typing of this thesis and Christine Page for the chapter 1 diagrams.

Finally I should like to thank the Science Research Council for providing the financial assistance for my studies.

The majority of the diagrams were produced using the PDP10 "grafix" package and written by Eddie Clayton, on the Tektronix 4015 and hard copier. Those of chapter 2 are mainly based on the BEBC users Handbook.